PENNING IONIZATION

Seventh International Conference on Dissociative Recombination (DR2007) IOP Publishing
Journal of Physics: Conference Series **192** (2009) 012023 doi:10.1088/1742-6596/192/1/012023

2009

Measurements of EEDF in recombination dominated afterglow plasma

R Plasil[1], I Korolov[1], T Kotrik[1], J Varju[1], P Dohnal[1], Z Donko[2], G Bano[2], J Glosik[1]

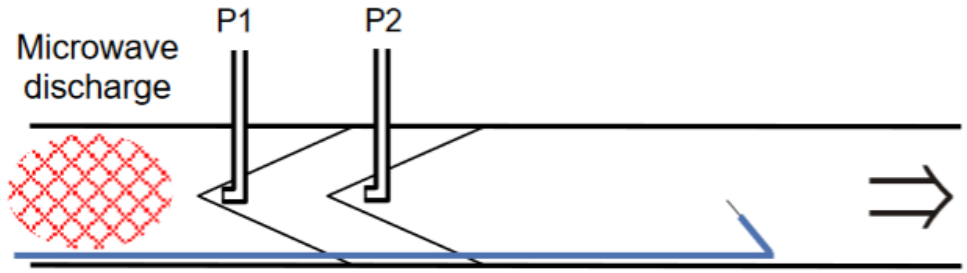

Figure 1. Principle of FALP method. He buffer gas carries the decaying plasma from discharge region along the flow tube. The reactant gases are added via ports P1 and P2. The plasma decay is monitored downstream from P2 ($t_{P2} = 0$).

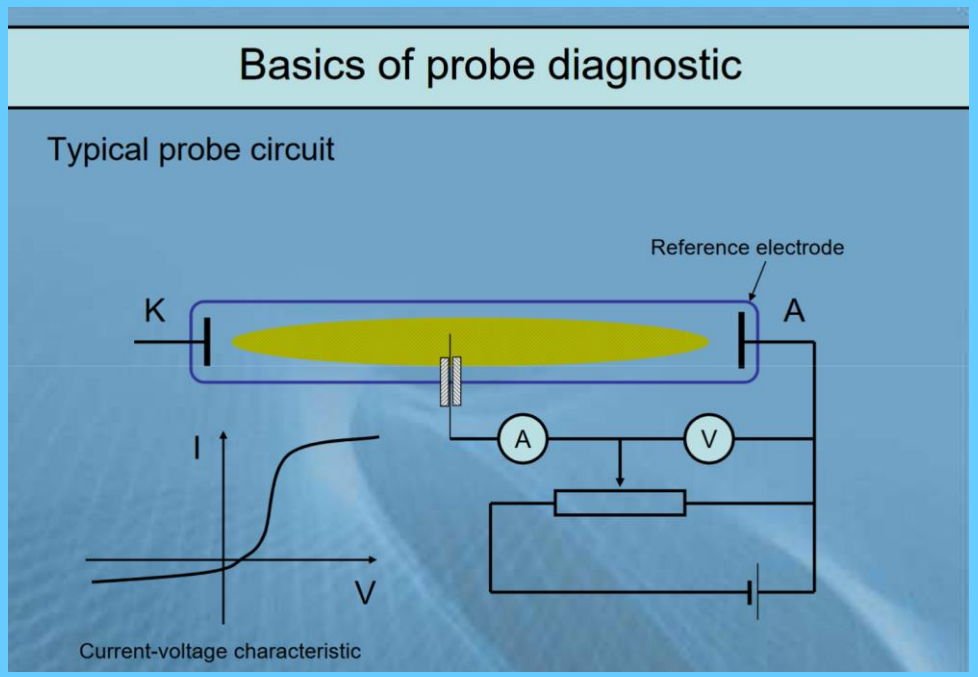

Contrib. Plasma Phys. **48**, No. 5-7, 461 – 466 (2008) / **DOI** 10.1002/ctpp.200810074

2008

Measurements of EEDF in Helium Flowwing Afterglow at Pressures 500 – 2000 PA

I. Korolov, R. Plašil, T. Kotrík, P. Dohnal, O. Novotný, and J. Glosík*

Electron Energy Distribution Functions (EEDF)

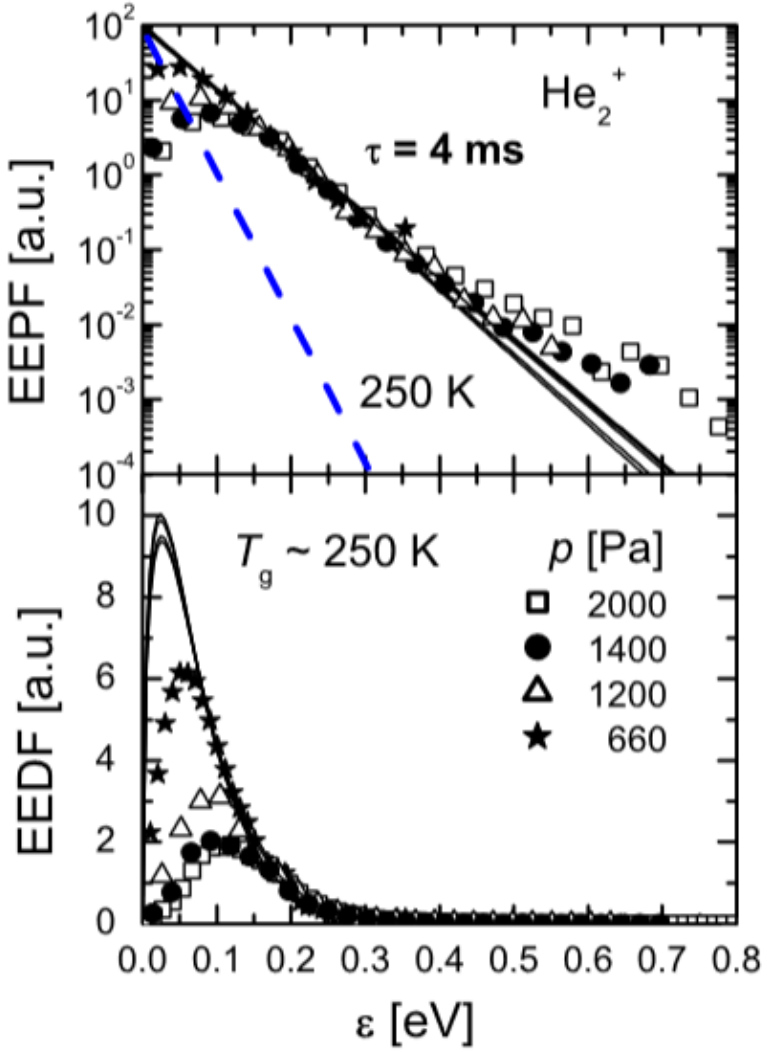

Fig. 4 Dependence of measured EEPF and EEDF on He pressure. **Upper panel:** The EEPF, $f_{\mathrm{PD}}(\varepsilon)$, obtained by using Druyvesteyn formula. The straight lines are fitted Maxwellian $f_{\mathrm{PM}}(\varepsilon)$. Dashed line indicates $f_{\mathrm{PM}}(\varepsilon)$ corresponding to $T_{\mathrm{e}} = 250$ K. **Lower panel:** The corresponding EEDF, $f_{\mathrm{D}}(\varepsilon)$. The full lines are fitted by Maxwellian $f_{\mathrm{M}}(\varepsilon)$, corresponding to straight lines $f_{\mathrm{PM}}(\varepsilon)$ in upper panel. **Comment to EEPF:** In order to simplify discussion, electron energy probability function EEPF is introduced by relation: $f_{\mathrm{P}}(\varepsilon) = f(\varepsilon)/\sqrt{(\varepsilon)}$. If EEDF is Maxwellian with temperature T_{e}, $f(\varepsilon) \equiv f_{\mathrm{M}}(\varepsilon) = A\sqrt{\varepsilon}\exp(-\varepsilon/k_{\mathrm{B}}T_{\mathrm{e}})$, then Electron Energy Probability Function (EEPF) is $f_P(\varepsilon) = A\exp(-\varepsilon/k_{\mathrm{B}}T_{\mathrm{e}})$, where A is a constant given by the normalization. If the formula (1) is applicable, then for plasma with Maxwellian EEDF the second derivative of the probe characteristic is also exponential, $I''_{\mathrm{Pr}}(U_{\mathrm{Pr}}) \approx I''_{\mathrm{e}}(U_{\mathrm{Pr}}) = Bn_{\mathrm{e}}\exp(-\varepsilon/k_{\mathrm{B}}T_{\mathrm{e}})$, where B is a constant given by probe geometry. The corresponding T_{e} can be determined simply from the linear part of the semi-logarithmic plot of I''_{Pr}.

Contrib. Plasma Phys. **48**, No. 5-7, 461 – 466 (2008) / **DOI** 10.1002/ctpp.200810074

2008

Measurements of EEDF in Helium Flowwing Afterglow at Pressures 500 – 2000 PA

I. Korolov, R. Plašil, T. Kotrík, P. Dohnal, O. Novotný, and J. Glosík*

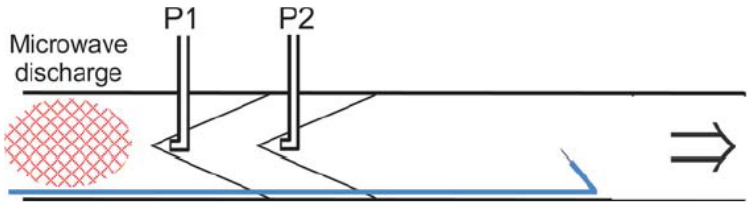

Fig. 1 Principle of FALP method. Buffer gas flows through the discharge region towards the Roots pump (right side). Plasma formed in the discharge is carried along the flow tube. The reactants are added via ports P_1 and P_2 to already cold plasma. The Langmuir probe is movable from the position of port P_2 up to the end of the flow tube. Relation between decay time and position is given by buffer gas velocity. (Online colour: www.cpp-journal.org).

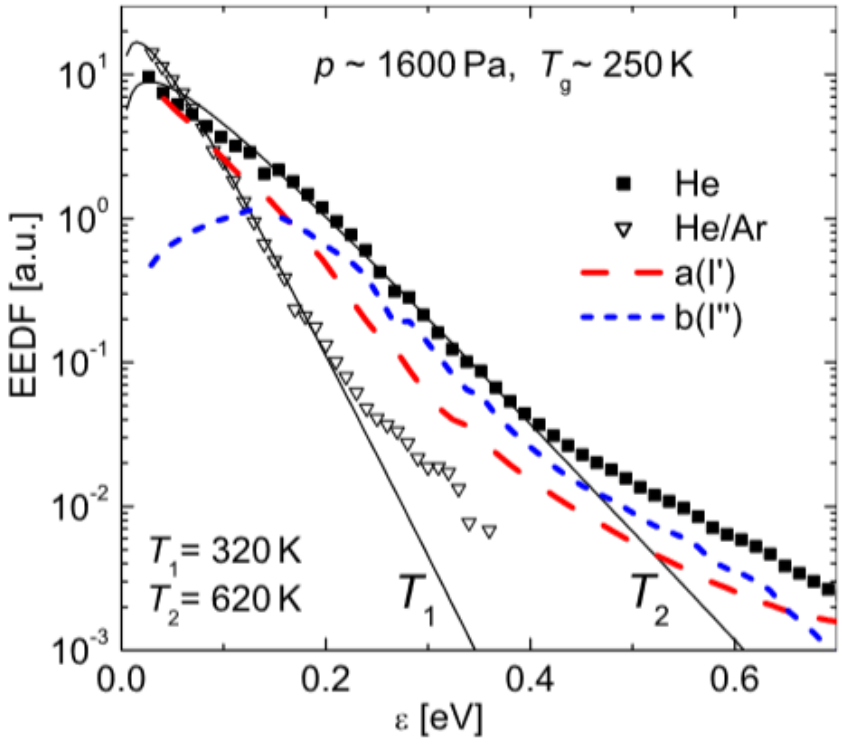

Fig. 6 The influence of He metastables on EEDF in afterglow plasma. The data were measured in afterglow plasma in He with and without addition of Ar in otherwise identical conditions. Ar was introduced via port P_1; measurements are made 35 ms downstream the position of P_2. Contributions $a(I'')$ and $b(I')$ from first and second term in formula (2) are indicated respectively. The full curves indicate Maxwellian fit to measured EEDF.

Contrib. Plasma Phys. **48**, No. 5-7, 461 – 466 (2008) / **DOI** 10.1002/ctpp.200810074

2008

Measurements of EEDF in Helium Flowwing Afterglow at Pressures 500 – 2000 PA

I. Korolov, R. Plašil, T. Kotrík, P. Dohnal, O. Novotný, and J. Glosík*

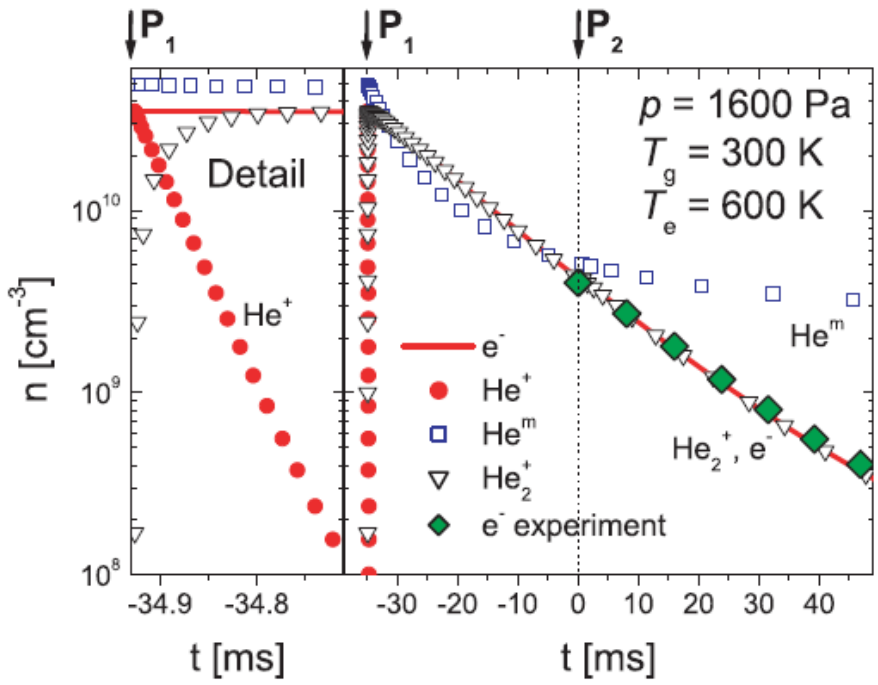

Fig. 2 Calculated evolutions of number densities of electrons, He^+ and He_2^+ ions and metastables He^m in He afterglow. Time $t = 0$ is assigned to position of entry port P_2. The detail on the left side showes fast formation of He_2^+. In the calculation, energies of electrons formed in chemi-ionization are not considered and, for simplicity, just one type of metastables is considered $He(2^3S)$. The used ambipolar diffusion coefficient was calculated for electron temperatures $T_e = 600$ K and He temperature $T_g = 250$ K. For comparison the measured decay of electron density is also included. (Online colour: www.cpp-journal.org).

EEDF

He/Ar/Xe/H_2

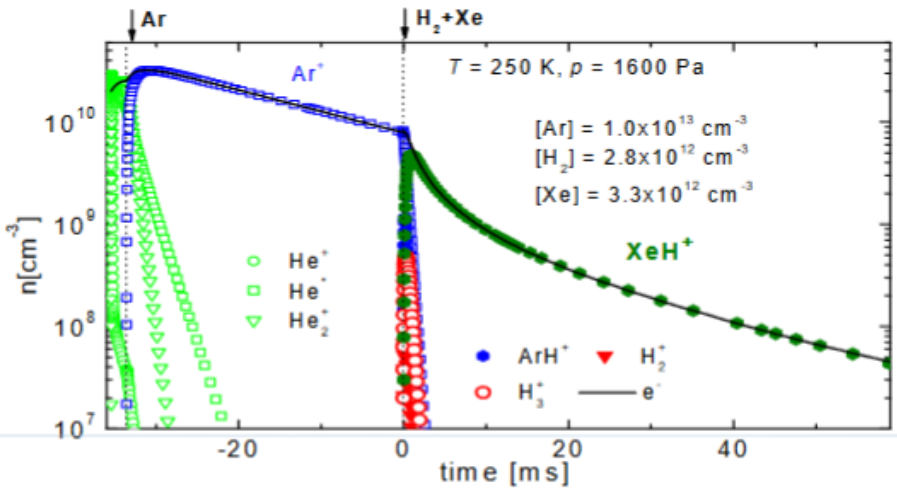

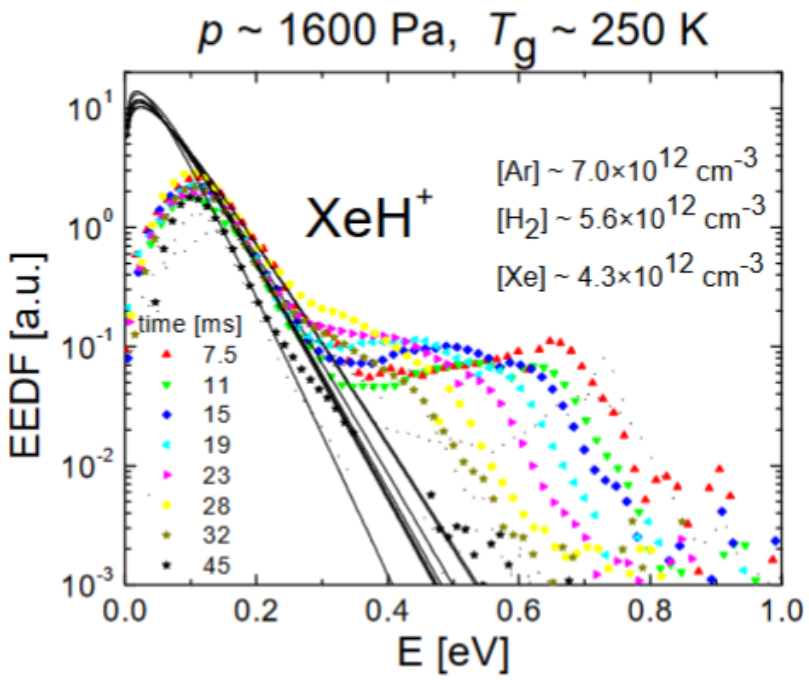

EEDF

He/Ar/Xe/H_2

Eur. Phys. J. D **54**, 391–398 (2009)
DOI: 10.1140/epjd/e2009-00144-3

THE EUROPEAN PHYSICAL JOURNAL D

Regular Article

2009

Non-Maxwellian electron energy distribution function in He, He/Ar, He/Xe/H_2 and He/Xe/D_2 low temperature afterglow plasma

R. Plasil[1,a], I. Korolov[1,2], T. Kotrik[1], P. Dohnal[1], G. Bano[2], Z. Donko[2], and J. Glosik[1]

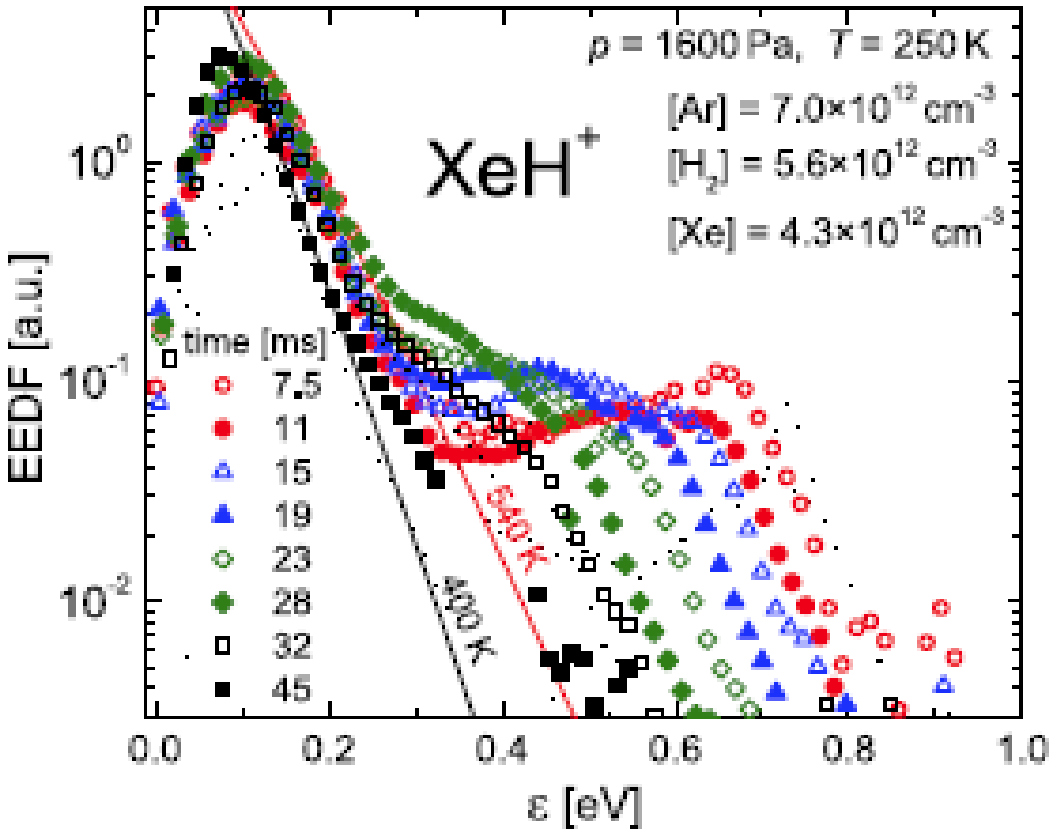

Fig. 8. (Color online) Evolution of EEDF in He/Ar/Xe/H_2 plasma obtained from measured characteristics of Langmuir probe. In low energy region (<0.15 eV), the EEDFs are expected to be Maxwellian [7]. The solid curves correspond to Maxwellian electron energy distributions fitted to the measured data for the decay time 7.5 ms and 45 ms. The plotted EEDFs are normalised to 1. Experimental conditions are indicated.

Seventh International Conference on Dissociative Recombination (DR2007) IOP Publishing
Journal of Physics: Conference Series **192** (2009) 012023 doi:10.1088/1742-6596/192/1/012023

Measurements of EEDF in recombination dominated afterglow plasma

R Plasil[1], I Korolov[1], T Kotrik[1], J Varju[1], P Dohnal[1], Z Donko[2], G Bano[2], J Glosik[1]

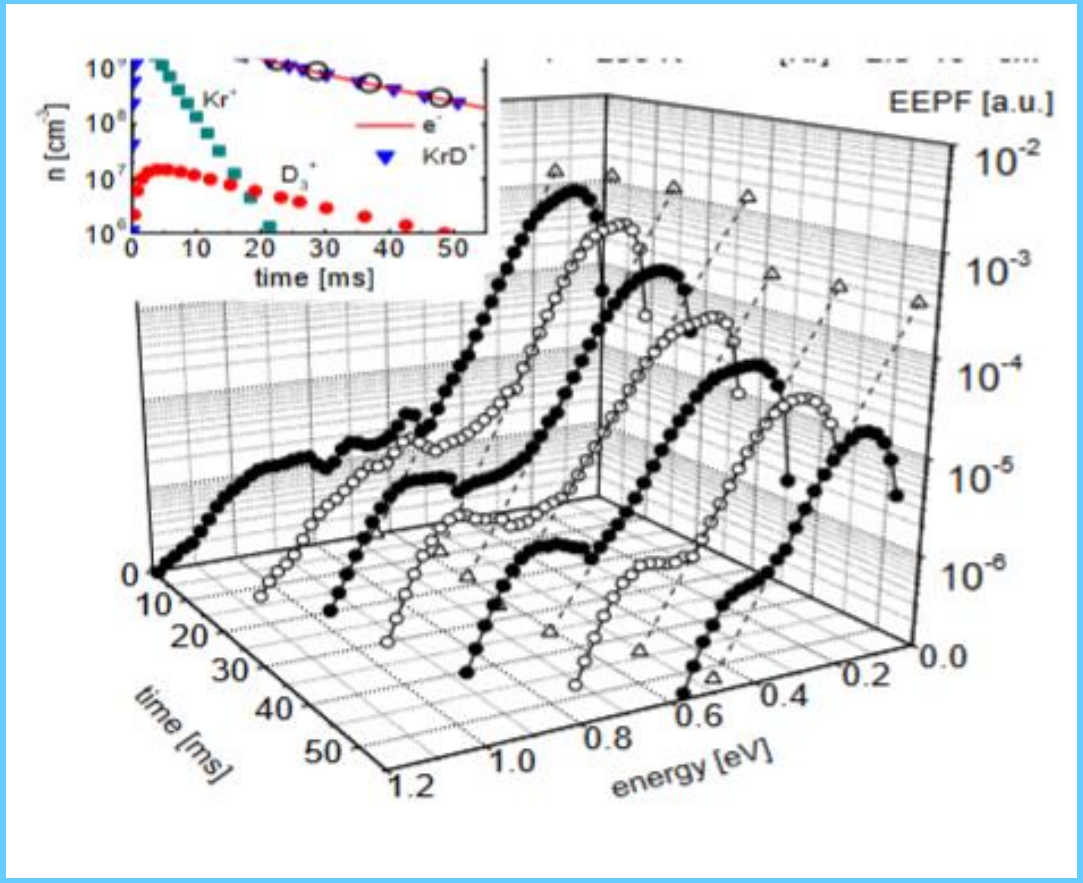

Figure 4. The evolution of EEPF in KrD^+ dominated recombining plasma. The measured electron density and the calculated ion composition are plotted in the inset.

Eur. Phys. J. D 54, 391–398 (2009)
DOI: 10.1140/epjd/e2009-00144-3

THE EUROPEAN PHYSICAL JOURNAL D

Regular Article

2009

Non-Maxwellian electron energy distribution function in He, He/Ar, He/Xe/H_2 and He/Xe/D_2 low temperature afterglow plasma

R. Plasil[1,a], I. Korolov[1,2], T. Kotrik[1], P. Dohnal[1], G. Bano[2], Z. Donko[2], and J. Glosik[1]

Reactant gases

He buffer gas

discharge

FALP

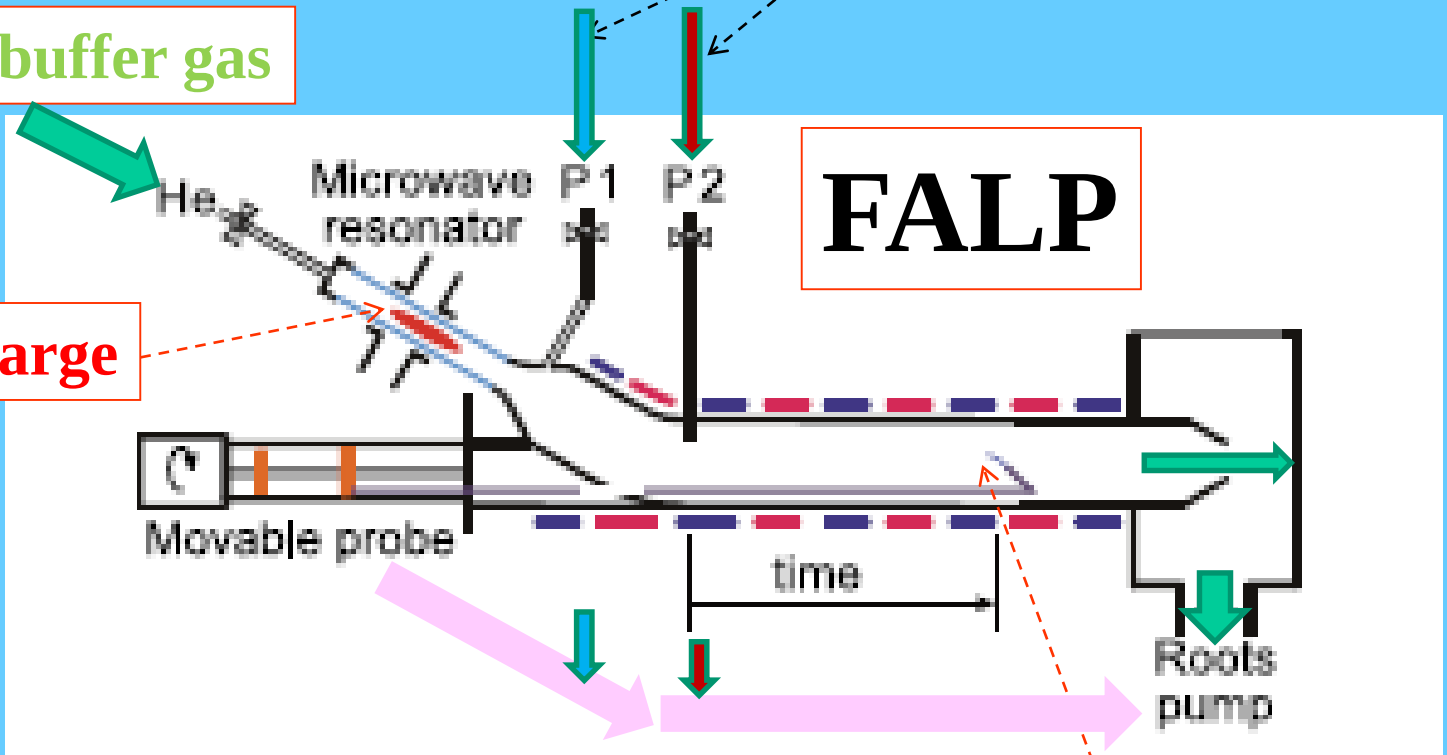

Fig. 1. (Color online) Schematic of FALP apparatus. Buffer gas flows from discharge region (upper left corner) towards the Roots pump (right). The plasma formed in the discharge is driven along the flow tube. The plasma parameters on the axis of the flow tube are measured by an axially movable Langmuir probe (from the port P2 up to the end of the flow tube).

Eur. Phys. J. D 54, 391–398 (2009)
DOI: 10.1140/epjd/e2009-00144-3

THE EUROPEAN PHYSICAL JOURNAL D

Regular Article

Non-Maxwellian electron energy distribution function in He, He/Ar, He/Xe/H_2 and He/Xe/D_2 low temperature afterglow plasma

R. Plasil[1,a], I. Korolov[1,2], T. Kotrik[1], P. Dohnal[1], G. Bano[2], Z. Donko[2], and J. Glosik[1]

2009

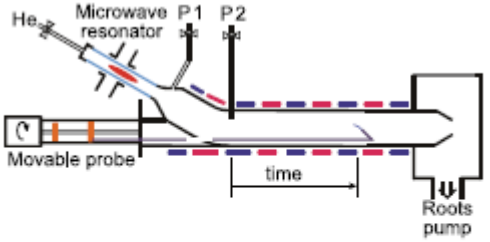

Fig. 1. (Color online) Schematic of FALP apparatus. Buffer gas flows from discharge region (upper left corner) towards the Roots pump (right). The plasma formed in the discharge is driven along the flow tube. The plasma parameters on the axis of the flow tube are measured by an axially movable Langmuir probe (from the port P2 up to the end of the flow tube).

T_e

n_e

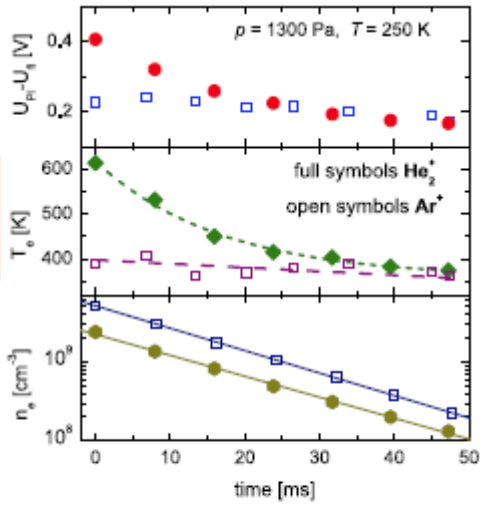

Fig. 2. (Color online) The evolution of afterglow plasma along the flow tube in He_2^+ (full symbols) and Ar^+ (open symbols) dominated plasmas. Upper panel: the difference between plasma and floating potential $\Delta = (U_{P1} - U_f)$. Middle panel: the measured electron temperature evolutions in He_2^+ and Ar^+ dominated plasmas. Lower panel: the decays of electron densities along the flow tube.

n_e

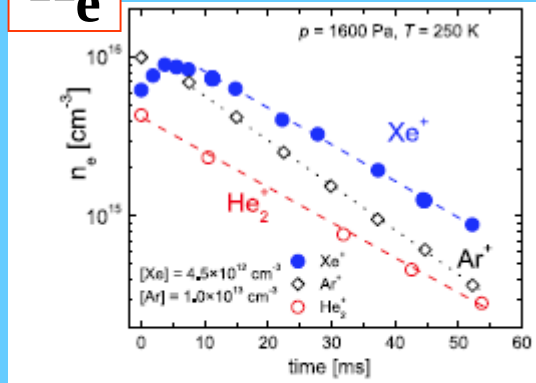

Fig. 3. (Color online) The measured decay of electron density in He_2^+ dominated plasma in pure He and the increase of the electron density in the afterglow plasma after injection of Xe via port P2. Indicated are the dominant ions. For comparison the electron density decay of argon plasma is plotted. In this case Ar is added to the afterglow via port P1.

1940

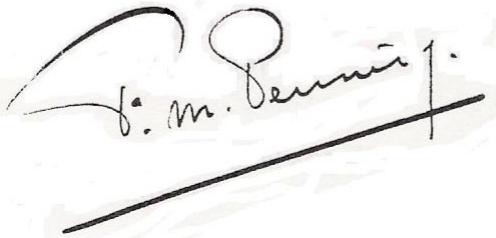

(1894-1953)

REVIEWS OF
MODERN PHYSICS

VOLUME 12 APRIL, 1940 NUMBER 2

The Mechanism of Electrical Discharges in Gases of Low Pressure*

M. J. DRUYVESTEYN AND F. M. PENNING

Natuurkundig Laboratorium der N. V. Philips' Gloeilampenfabrieken, Eindhoven, Holland

1927

F. M. Penning

(1894-1953)

Über Ionisation durch metastabile Atome.

Während einer Untersuchung über das Funkenpotential von Neon für größere Werte von pd (Druck × Elektrodenabstand) zeigte sich, daß dieses beträchtlich erniedrigt wurde durch sehr geringe Beimischung (0,0001 bis 0,1 %) von anderen Gasen mit niedrigerer Ionisierungsspannung. Nähere Experimente mit Argon zeigten, daß die Bedingung für diesen Effekt ist: $V_{met.} > V_i'$. ($V_{met.}$ = Anregungsspannung der metastabilen Zustände des Edelgases; V_i' = Ionisierungsspannung des beigemischten Gases.) Sehr wahrscheinlich ist die Erklärung folgende. Mit zunehmenden Werten von pd wird in einem reinen Edelgase das Funkenpotential größer, weil eine immer größer werdende Prozentzahl der Elektronen die Atome anregen statt zu ionisieren. Ein Teil dieser angeregten Atome befindet sich in metastabilem Zustand oder kommt durch Lichtausstrahlung in diesen Zustand. Jedes dieser metastabilen Atome wird nun, während seiner langen Lebensdauer (bei Neon von 1 cm Druck etwa 0,002 sec.) eine große Anzahl von Zusammenstößen mit anderen Atomen machen. Dabei wird es seine Energie $V_{met.}$ an ein fremdes Atom (mit Ionisierungsspannung V_i') übertragen können[1] und dieses letztere ionisieren, wenn $V_{met} > V_i'$. Dieser Prozeß ist also vorzustellen als: Metast. Atom + fremdes Atom = normales Atom + fremdes Ion.

In unterstehenden Tafeln sind einige Resultate zusammengefaßt. Alle Messungen wurden ausgeführt mit ebenen, parallelen Elektroden (meistens Fe). V_f bedeutet das Funkenpotential des reinen Gases, V_f' dasselbe nach Beimischung des Fremdgases (auf 10 V abgerundet), V_i' die Ionisierungsspannung des Fremdgases.

Neon $V_{met.}$ = 16,5 und 16.6 V.

pd (mm × cm)	V_f	V_f'	Beimischung %		V_i'
22	400 V	290 V	0,0001	Hg	10.4 V
22	400 V	200 V	0,001	Hg	10.4 V
22	400 V	150 V	0,05	Hg	10,4 V
20	350 V	170 V	0.02	Kr	13,3 V
81	750 V	180 V	0.006	Ar	15,4 V
15	320 V	160 V	0.03	Ar	15.4 V
18	340 V	210 V	0,05	H_2	16.1 V
18	340 V	160 V	0.05	N_2	16 à 17 V

Argon $V_{met.}$ = 11,5 und 11,7 V.

pd (mm × cm)	V_f	V_f'	Beimischung %		V_i'
15	510 V	340 V	0.02	J_2	10 V
15	510 V	300 V	0,07	J_2	10 V
14	540 V	460 V	0,0001	Hg	10,4 V
14	540 V	170 V	0.03	Hg	10.4 V
15	520 V	530 V	0,03	Xe	11.5 V
14	500 V	500 V	0.03	Kr	13.3 V

Eindhoven, Natuurkundig Laboratorium der N. V. Philips' Gloeilampenfabrieken, den 31. August 1927.

F. M. PENNING.

[1] Auf ähnliche Weise war schon vor den hier beschriebenen Messungen von HOLST und OOSTERHUIS das Quecksilberlicht in der positiven Säule von Röhren mit Argon und ein wenig Quecksilber erklärt, nl. durch die Anregung oder Ionisation der Quecksilberatome durch metastabile Argonatome.

F. M. Penning,
Naturwissenschaften 15, 818 (1927)

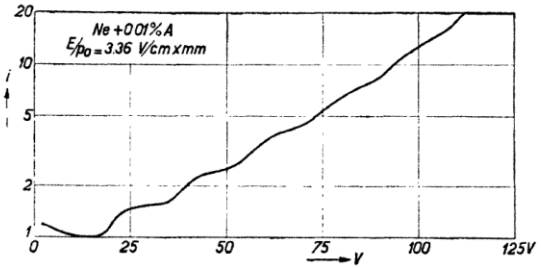

FIG. 8. Steplike increase of i as a function of V at constant E/p_0 due to ionization of A atoms by metastable Ne atoms.

The Penning ionization process …

… it's elementary, my dear Watson.

ELECTRON SPECTROSCOPY AND MASS SPECTROMETRIC STUDY OF PENNING IONIZATION OF MOLECULES

F. Vecchiocattivi
Dipartimento d'Ingegneria Civile ed Ambientale
Università degli Studi di Perugia
Perugia - Italy

Grotrian diagram He

Energy levels He

Ionization energy He

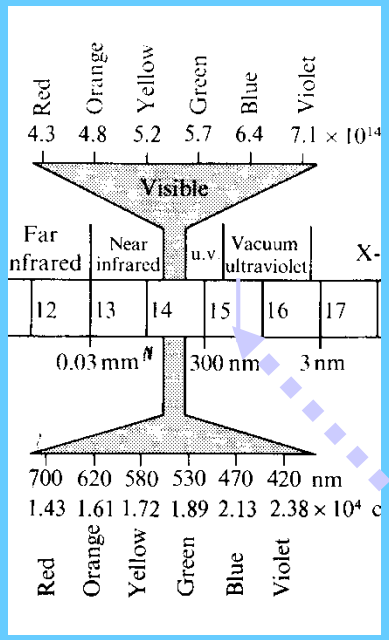

24.46eV

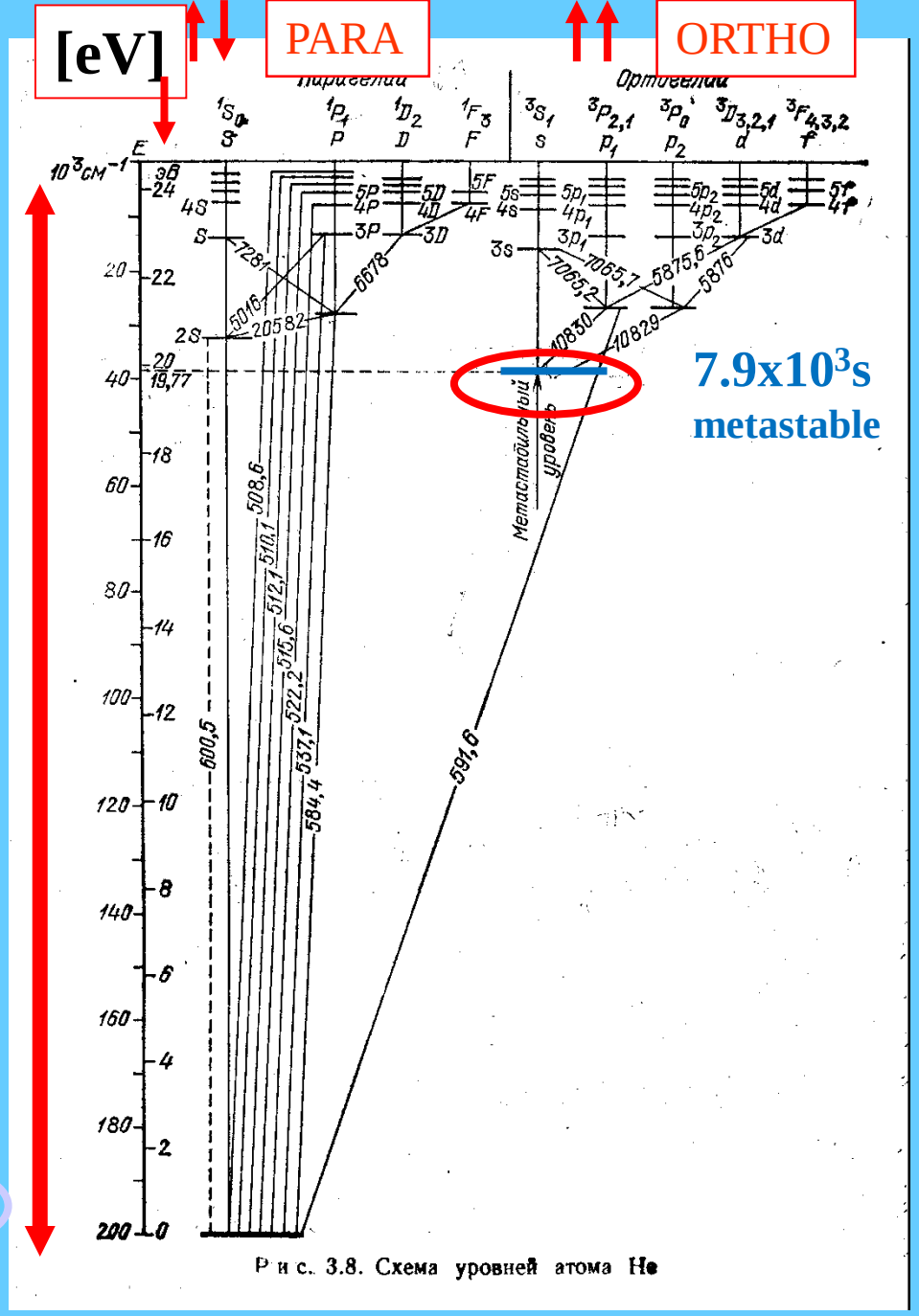

24.46eV → ~198400 cm^{-1} → ~50nm

vacuum ultraviolet

Energy levels He

Grotrian diagram He

Ionization energy He

24.46eV

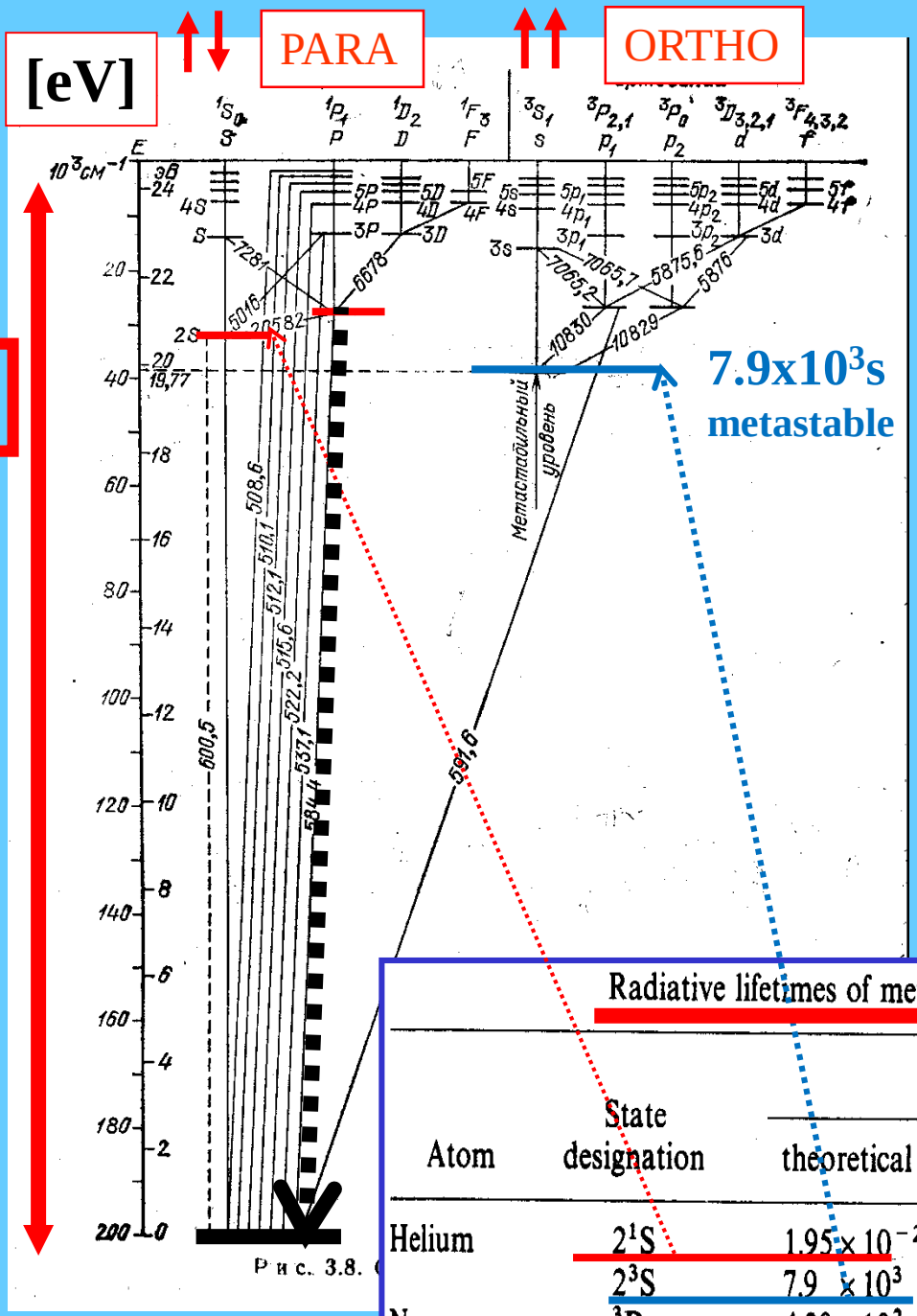

Radiative lifetimes of metastable rare-gas atoms

Atom	State designation	Radiative lifetime (s) theoretical	ref.	experimental
Helium	2^1S	1.95×10^{-2}	*a*	1.97×10^{-2}
	2^3S	7.9×10^{3}	*c*	9.0×10^{3}
Neon	$^3P_0$	4.30×10^{2}	*e*	
	$^3P_2$	2.44×10^{1}	*e*	>0.8

24.46eV → ~198400 cm^{-1} → ~50nm

Tables

Energy levels for rare-gas atoms and photons[a]

Atom	Electron configuration	Metastables		Resonance photons		
		designation	energy (eV)	transition	wavelength (nm)	energy (eV)
Helium	1s2p			$2^1P \rightarrow 1^1S$	58.44	21.217
				$2^1P \rightarrow 2^1S$	2058.7	0.602
				$2^3P \rightarrow 2^3S$	1083.0	1.145
	1s2s	2^1S	20.616			
		2^3S	19.818			
Neon	$2p^5 3s$	$^3P_0$	16.716			
		$^3P_2$	16.619			
Argon	$3p^5 4s$	$^3P_0$	11.723			
		$^3P_2$	11.548			
Krypton	$4p^5 5s$	$^3P_0$	10.562			
		$^3P_2$	9.915			
Xenon	$5p^5 6s$	$^3P_0$	9.447			
		$^3P_2$	8.315			

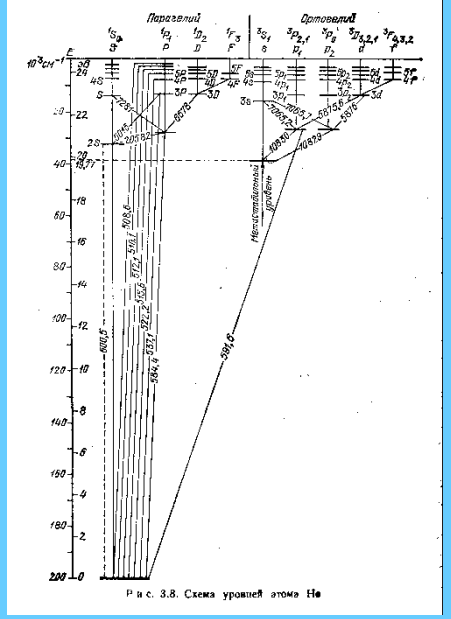

Рис. 3.8. Схема уровней атома He

1eV~23.6 kcal/mol

Radiative lifetimes of metastable rare-gas atoms

Atom	State designation	Radiative lifetime (s) theoretical	ref.	experimental
Helium	2^1S	1.95×10^{-2}	*a*	1.97×10^{-2}
	2^3S	7.9×10^{3}	*c*	9.0×10^{3}
Neon	$^3P_0$	4.30×10^{2}	*e*	
	$^3P_2$	2.44×10^{1}	*e*	>0.8
Argon	$^3P_0$	4.49×10^{1}	*e*	
	$^3P_2$	5.59×10^{1}	*e*	>1.3
Krypton	$^3P_0$	4.9×10^{-1}	*e*	
	$^3P_2$	8.51×10^{1}	*e*	>1.0
Xenon	$^3P_0$	7.8×10^{-2}	*e*	
	$^3P_2$	14.95×10^{1}	*e*	

Ústav vznikl v roce 1972 sloučením Ústavu fyzikální chemie a Polarografického ústavu, které oba byly součástí tehdejší Československé akademie věd (ČSAV).

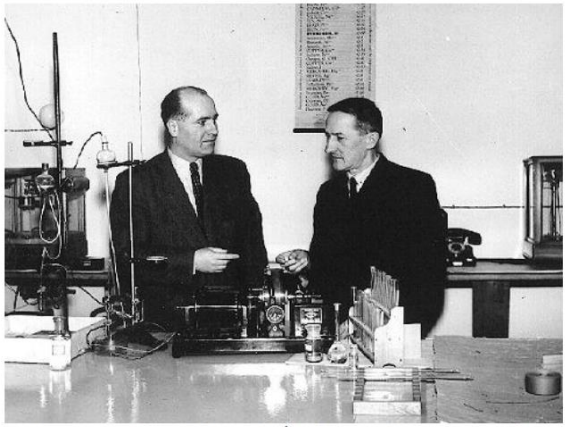

Profesor R. Brdička (vlevo) a profesor J. Heyrovský, ředitelé Ústavu fyzikální chemie resp. Polarografického ústavu (1952).

Obr. 2. **Budova v Máchově ulici 7, Praha 2-Vinohrady, sídlo ústavu v létech 1957–1988**

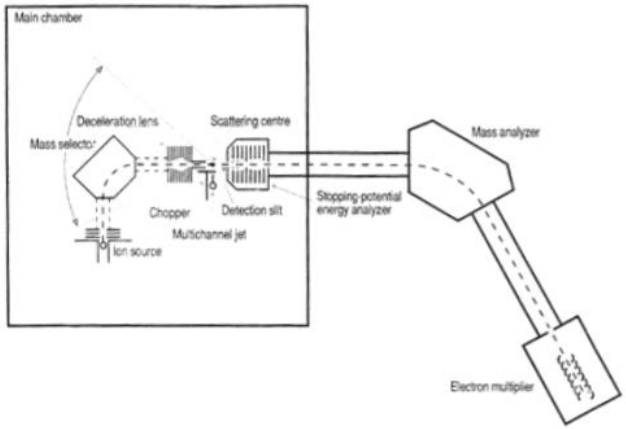

Obr. 8. **Schema přístroje pro výzkum dynamiky iontových procesů za podmínek jediné srážky mezi částicemi, využívající metodu rozptylu ve zkřížených paprscích částic (Z. Herman[15])**

THE FIRST TRY (July 30, 1958)

INSTITUTE OF PHYSICAL CHEMISTRY, ACADEMY OF SCIENCES, PRAGUE

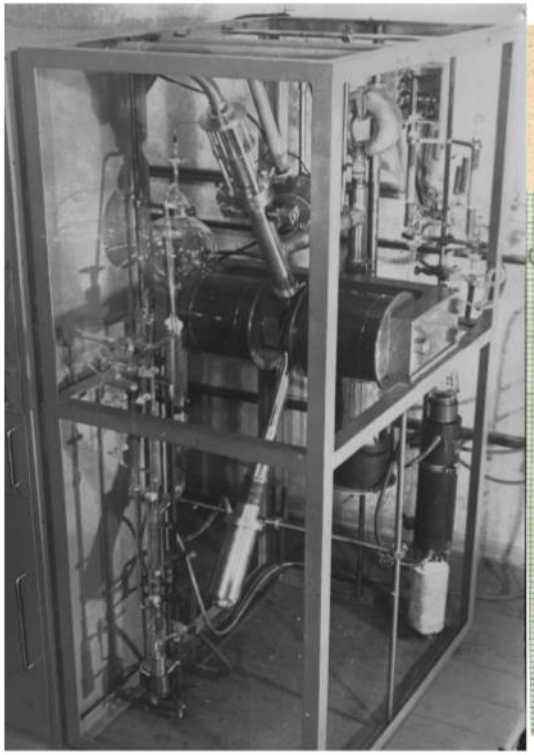

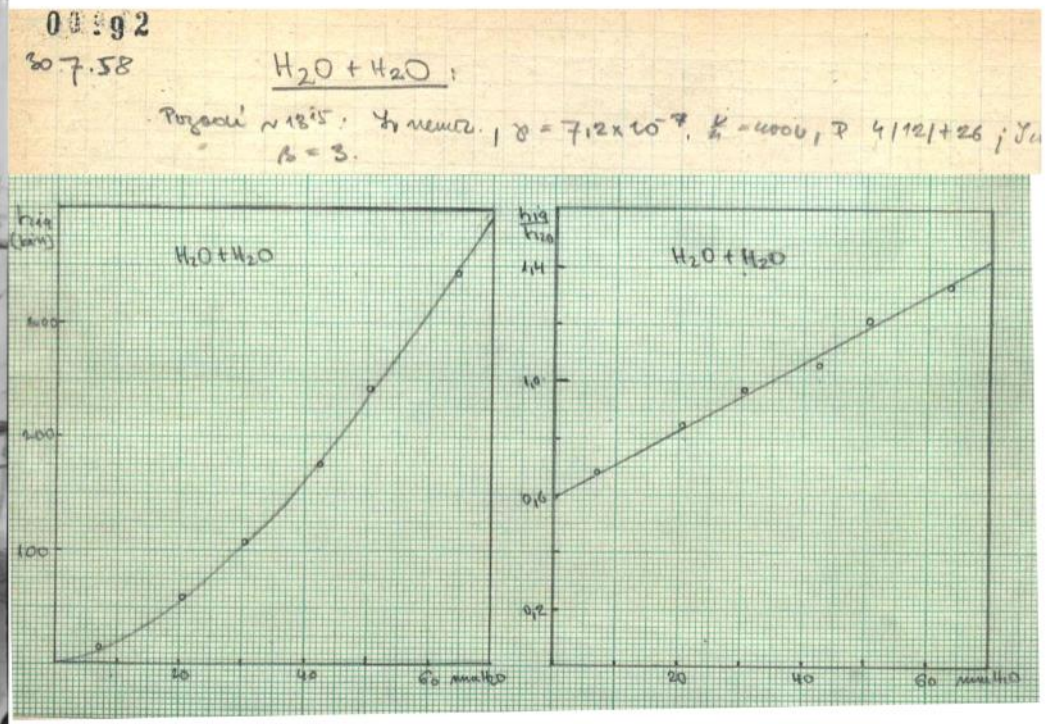

(Mann et al 1940) - Talroze 1952 - Stevenson, Schissler 1955-56 – Field, Franklin, Lampe 1957

1970 - 1982
DYNAMICS OF ION-MOLECULE PROCESSES

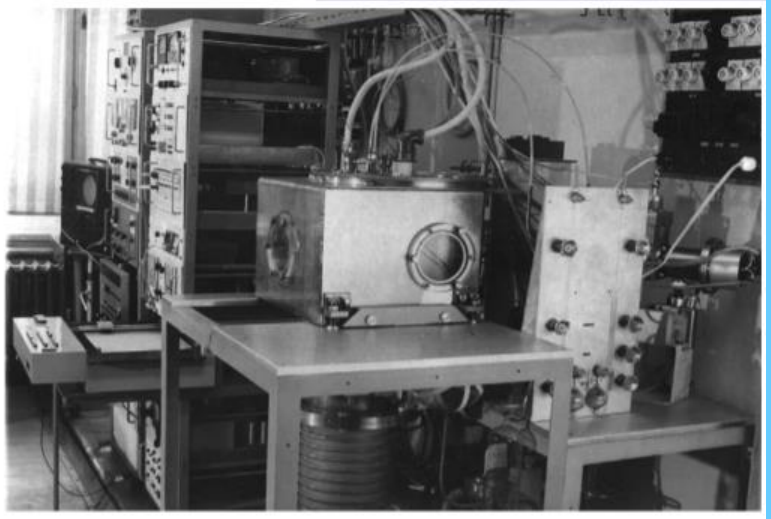

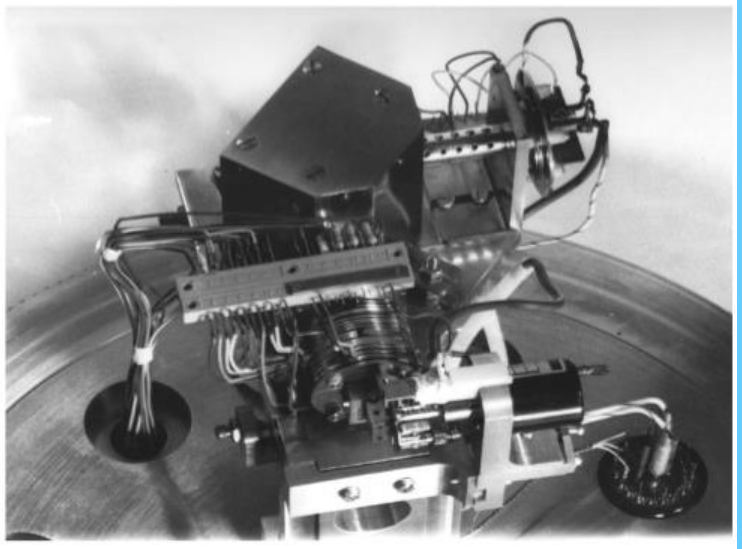

Prague, after 1969

EVA II

(with V. Pacák)

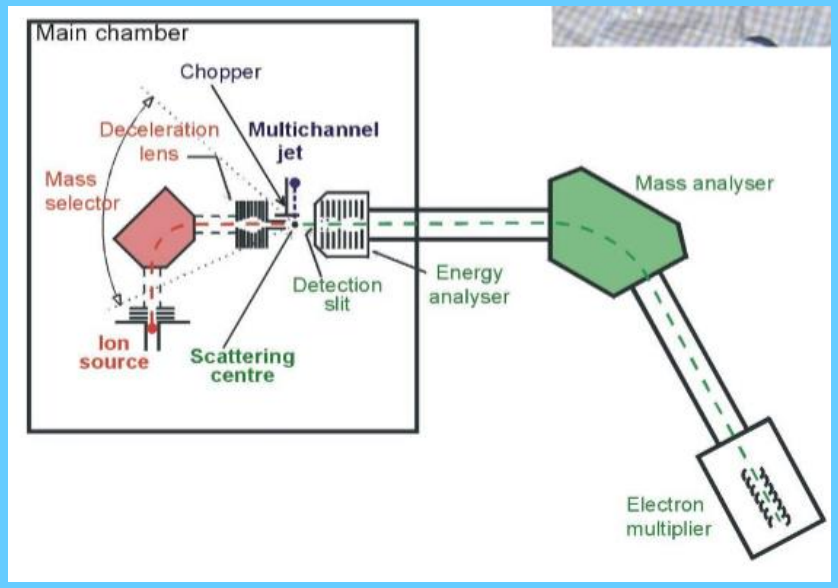

EPRP 2A 2023

PENNING IONIZATION

Penning Ionization and related Processes
Andrew J. Yencha
State University of New York at Alabany, USA
Electron spectroscopy Vo 5 Academic Press, London 1984

THE JOURNAL OF CHEMICAL PHYSICS **122**, 164307 (2005)

Penning ionization of N_2O molecules by $He^*(2^{3,1}S)$ and $Ne^*(^3P_{2,0})$ metastable atoms: A crossed beam study

Francesco Biondini
Dipartimento di Ingegneria Civile ed Ambientale, Università di Perugia, 06125 Perugia, Italy

J. Phys. B: At. Mol. Opt. Phys. **31** (1998) 4813–4820. Printed in the UK PII: S0953-4075(98)92666-9

Penning ionization of the CO_2 molecule by $He^*(2\,^1S)$ metastable atoms

M Ben Arfa, B Lescop, M Cherid and G Fanjoux
Laboratoire des Collisions Electroniques et Atomiques, Faculté des Sciences et Techniques de Brest, 6 Avenue Le Gorgeu, 29287 Brest Cedex, France

Atmosphere **2015**, *6*, 299-317; doi:10.3390/atmos6030299

OPEN ACCESS

atmosphere

ISSN 2073-4433

www.mdpi.com/journal/atmosphere

Article

The Possible Role of Penning Ionization Processes in Planetary Atmospheres

Stefano Falcinelli [1,2,*], Fernando Pirani [3] and Franco Vecchiocattivi [2]

JOURNAL OF CHEMICAL PHYSICS VOLUME 111, NUMBER 16 22 OCTOBER 1999

The chemi-ionization of $He^*(2\,^{1,3}S)$ + Ar,Kr,Xe for collision energies from 0.003 to 6 eV

R. Feltgen, H. Ferkel,[a] R. K. B. Helbing,[b] A. Lindinger, D. Pikorz, and H. Vehmeyer
Max-Planck-Institut für Strömungsforschung, Bunsenstr.10, D-37073 Göttingen, Germany

PENNING IONIZATION

$$A^* + M \rightarrow (A...M)^* \rightarrow (A...M)^+ + e^-$$

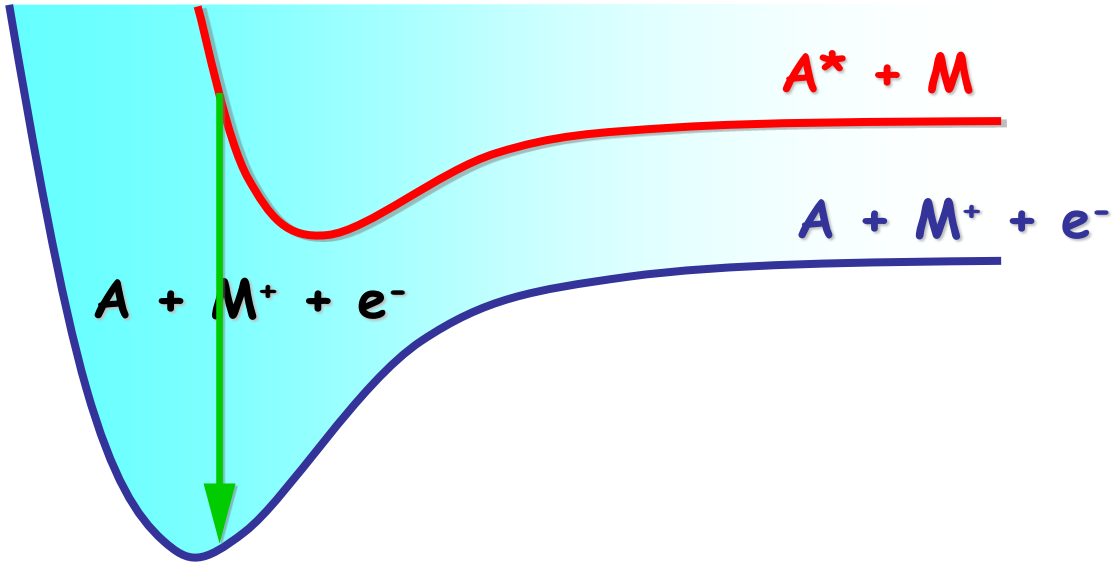

Penning ionization

$X^* + Y \rightarrow X + Y^+ + e^-$	**Penning Ionisation (PI)**
$X^* + AB \rightarrow X + AB^+ + e^-$	**Penning Ionisation (PI)**
$X^* + Y \rightarrow XY^+ + e^-$	**Associative Ionization (AI)**
$X^* + AB \rightarrow XAB^+ + e^-$	**Associative Ionization (AI)**
$He^* + He \rightarrow He_2^+ + e^-$	**Hornbeck-Molnar process.**

The process of PI was first postulated in 1927 by F.M. Penning
Examples of studied processes are:

$$He^* + Ar \rightarrow He + Ar^+ + e^-$$

$$Cs^* + Cs \rightarrow Cs_2^+ + e^-$$

$X^* + Y \rightarrow X + Y^*$	Excitation transfer	(3a)
$X^* + AB \rightarrow X + AB^*$	Excitation transfer	(3b)
$X^* + AB \rightarrow X + A^* + B$	Dissociative Exc. Trans.	(4)
$X^* + AB \rightarrow X + A + B$	Collisional Dissociation.	(5)
$X^* + AB \rightarrow X + A^+ + B$	Diss.Ionization	(6)

$X^* + Y \rightarrow X + Y$ Quenching $\leftarrow\rightarrow$ Excitation transfer

Resonant processes

Helium-neon laser:

$$He^*(1s2s, 2^1S) + Ne(^1S_0) \rightarrow He(^1S_0) + Ne^*(^1P_1)$$

Followed by

$$Ne^*(2p^55s, {}^1P_1) \rightarrow Ne^*(2p^53p) + h\nu(623{,}8\ nm)$$

24.46eV → ~198400 cm^{-1} → ~50nm
vacuum ultraviolet

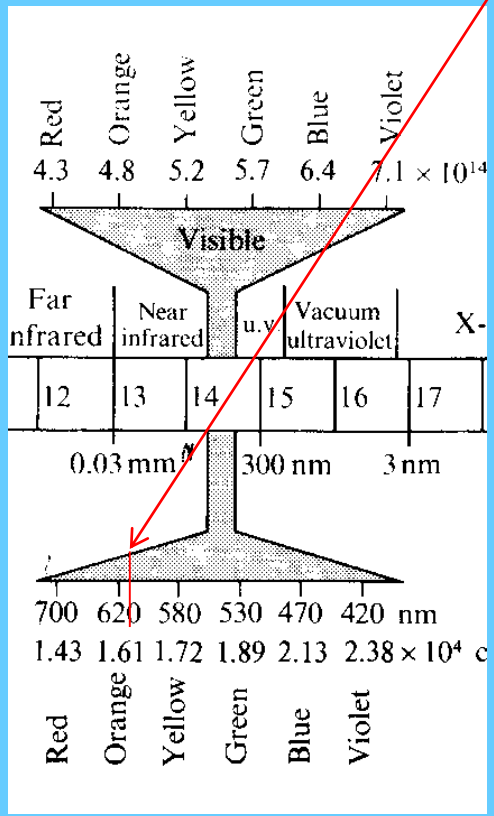

Resonant processes

Excimer formation:

$X^* + X + X \rightarrow X_2^* + X$ **Excimer formation**

$X^* + Y + X(\text{or } Y) \rightarrow XY^* + X(\text{or } Y)$ **Excimer formation**

Excimer lamps are quasimonochromatic light sources operating over a wide range of wavelengths in the ultraviolet (UV) and vacuum ultraviolet (VUV) spectral regions. Operation of an excimer lamp is based on the formation of **excited dimers (excimers),** which spontaneously transiting from the excited state to the ground state result in the emission of UV-photons. The spectral maximum of excimer lamp radiation is specified by a working excimer molecule (see table below).

Excimer lamps are quasimonochromatic light sources operating over a wide range of wavelengths in the ultraviolet (UV) and vacuum ultraviolet (VUV) spectral regions. Operation of an excimer lamp is based on the formation of excited dimers (excimers), which spontaneously transiting from the excited state to the ground state result in the emission of UV-photons. The spectral maximum of excimer lamp radiation is specified by a working excimer molecule (see table below).

Wavelength and photon energy of excimer lamp radiation.

Working excimer molecule	Wavelength (nm)	Photon energy (eV)
NeF*	108	11.48
Ar_2^*	126	9.84
Kr_2^*	146	8.49
F_2^*	158	7.85
ArBr*	165	7.52
Xe_2^*	172	7.21
ArCl*	175	7.08
KrI*	190	6.49
ArF*	193	6.42

Theoretical model of Penning ionization

Two states potential-curve model first proposed by
Z. Herman and V. Cermak
Coll. Czech. Chem. Commun. 31, (1966) 649

It is proposed that PI occurs by autoionizing transition between two adiabatic potential curves representing the **formation of quasi-molecule** by the following energy transfer scheme:

$$X^* + AB \rightarrow [X^*AB] \rightarrow [XAB^+ + e^-] \rightarrow X + AB^+ + e^-$$

$$V^*(R) \rightarrow V^+(R)$$

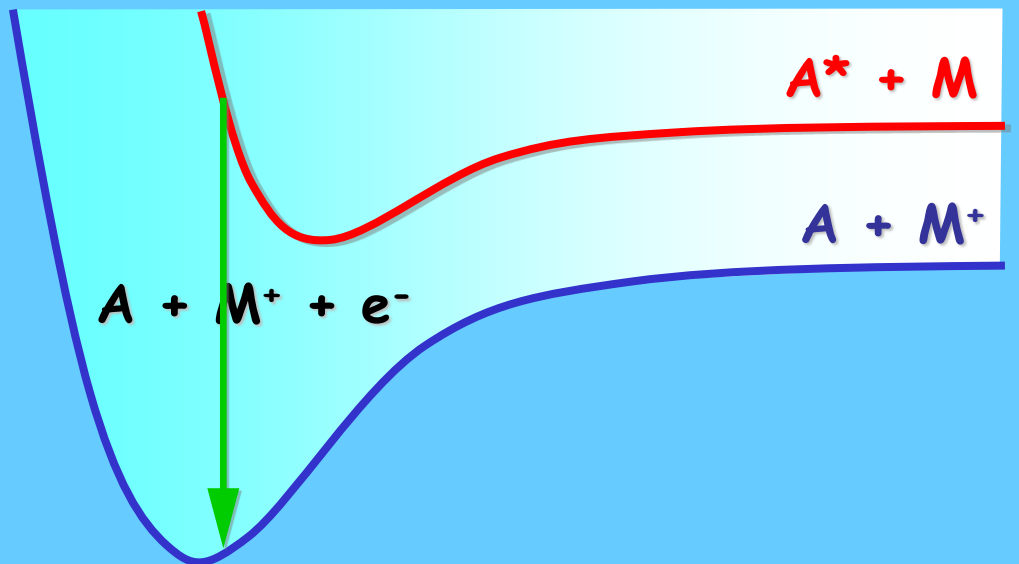

Formation of quasi-molecule by the following energy transfer

$$X^* + AB \rightarrow [X^*AB] \rightarrow [XAB^+ + e^-] \rightarrow X + AB^+ + e^-$$

$V^*(R)$ → $V^+(R)$

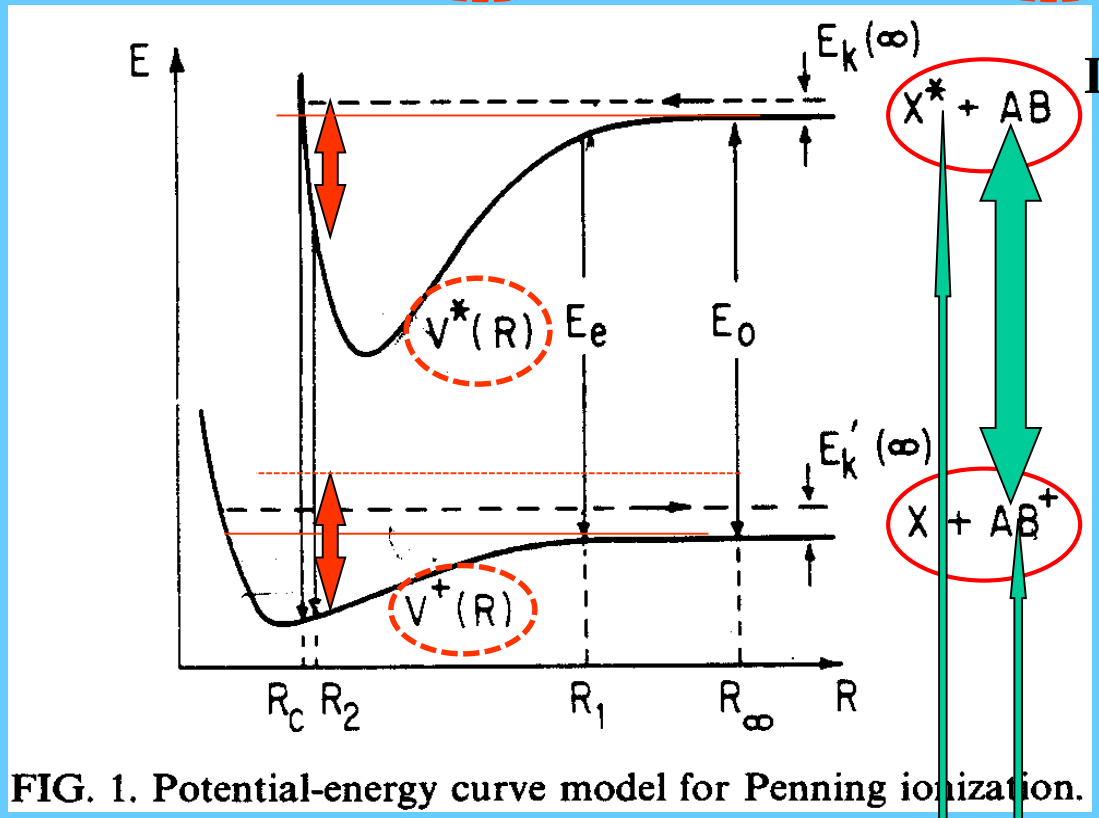

FIG. 1. Potential-energy curve model for Penning ionization.

INCOMING CHANNEL

OUTGOING CHANNEL

Ionization by a vertical downward transition (within **Born-Oppenheimer approximation**) from the upper, incoming channel, to the lower, outgoing channel.

That is, both the interpacticle separation and instantaneous relative kinetic energy are conserved during ionization, I.e. $R=R`$, $E_K(R)=E`_K(R`)$

$$E_K(R)=E`_K(R)$$

Two potential curve model for Penning ionization

$$X^* + AB \rightarrow [X^*AB] \rightarrow [XAB^+ + e^-] \rightarrow X + AB^+ + e^-$$

$$V^*(R) \rightarrow V^+(R)$$

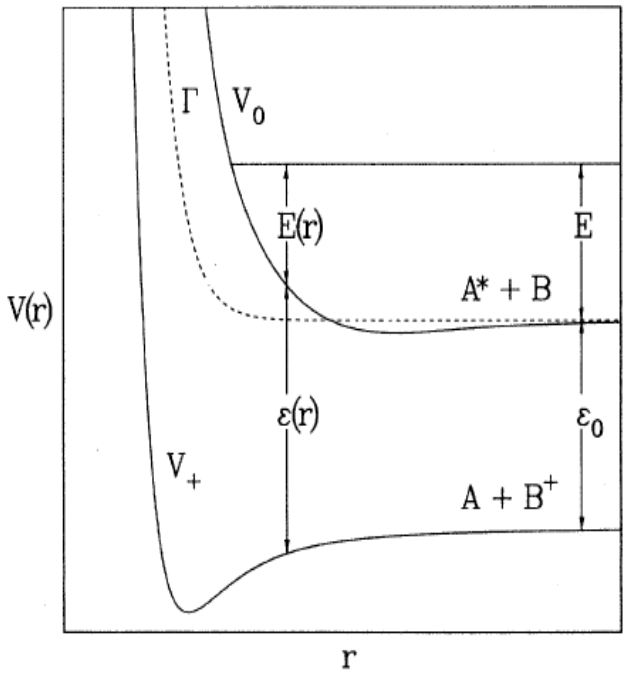

FIG. 2. Two-potential-curve model for Penning ionization. E is the center-of-mass kinetic energy of collision; ε_0 is the separation of the reagent and product potential asymptotes, $\varepsilon_0 = E_*(A^*) - IE(B)$; $E(r)$ is the (classical) local heavy-particle kinetic energy, including centrifugal energy; and $\varepsilon(r)$ is the kinetic energy of the Penning electron when Penning ionization takes place at separation r.

Formation of quasi-molecule by the following energy transfer

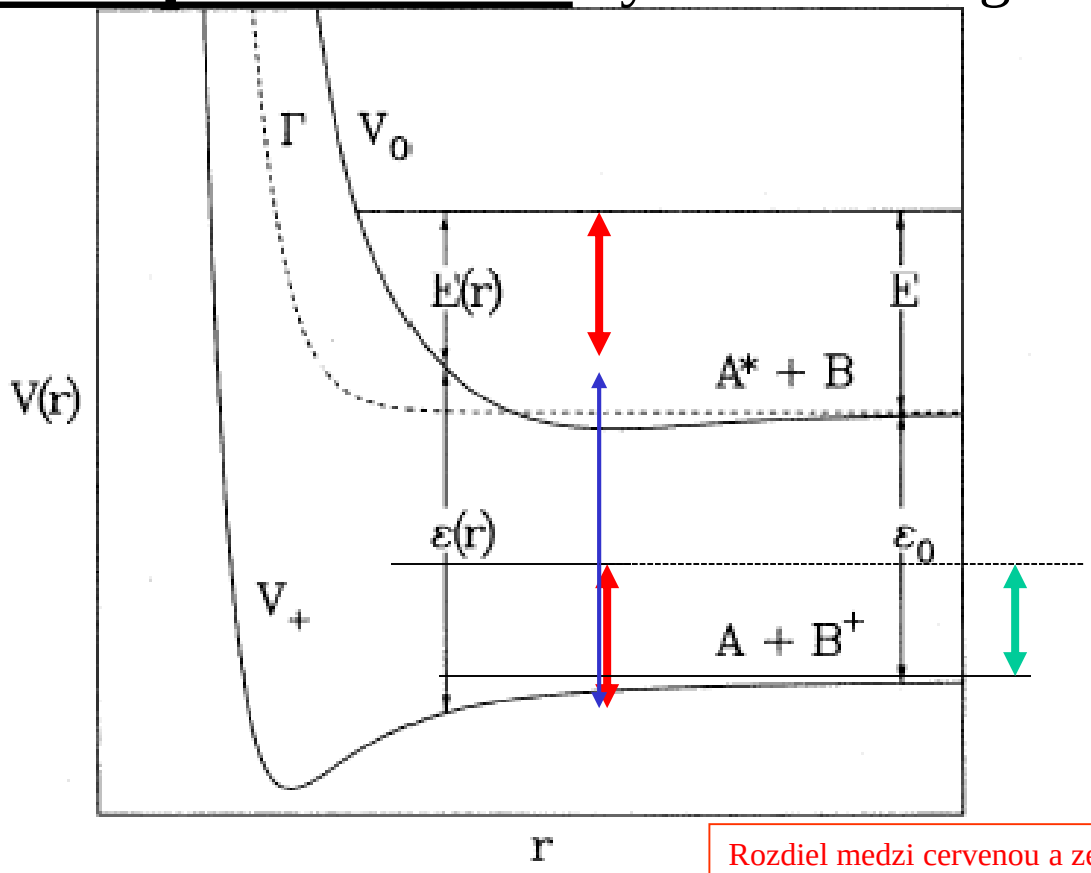

Rozdiel medzi cervenou a zelenou je vlastne energia ktorou bol molekularny iont viazany , ta sa musi prekonat

FIG. 2. Two-potential-curve model for Penning ionization. E is the center-of-mass kinetic energy of collision; ε_0 is the separation of the reagent and product potential asymptotes, $\varepsilon_0 = E_*(A^*) - IE(B)$; $E(r)$ is the (classical) local heavy-particle kinetic energy, including centrifugal energy; and $\varepsilon(r)$ is the kinetic energy of the Penning electron when Penning ionization takes place at separation r.

Reality

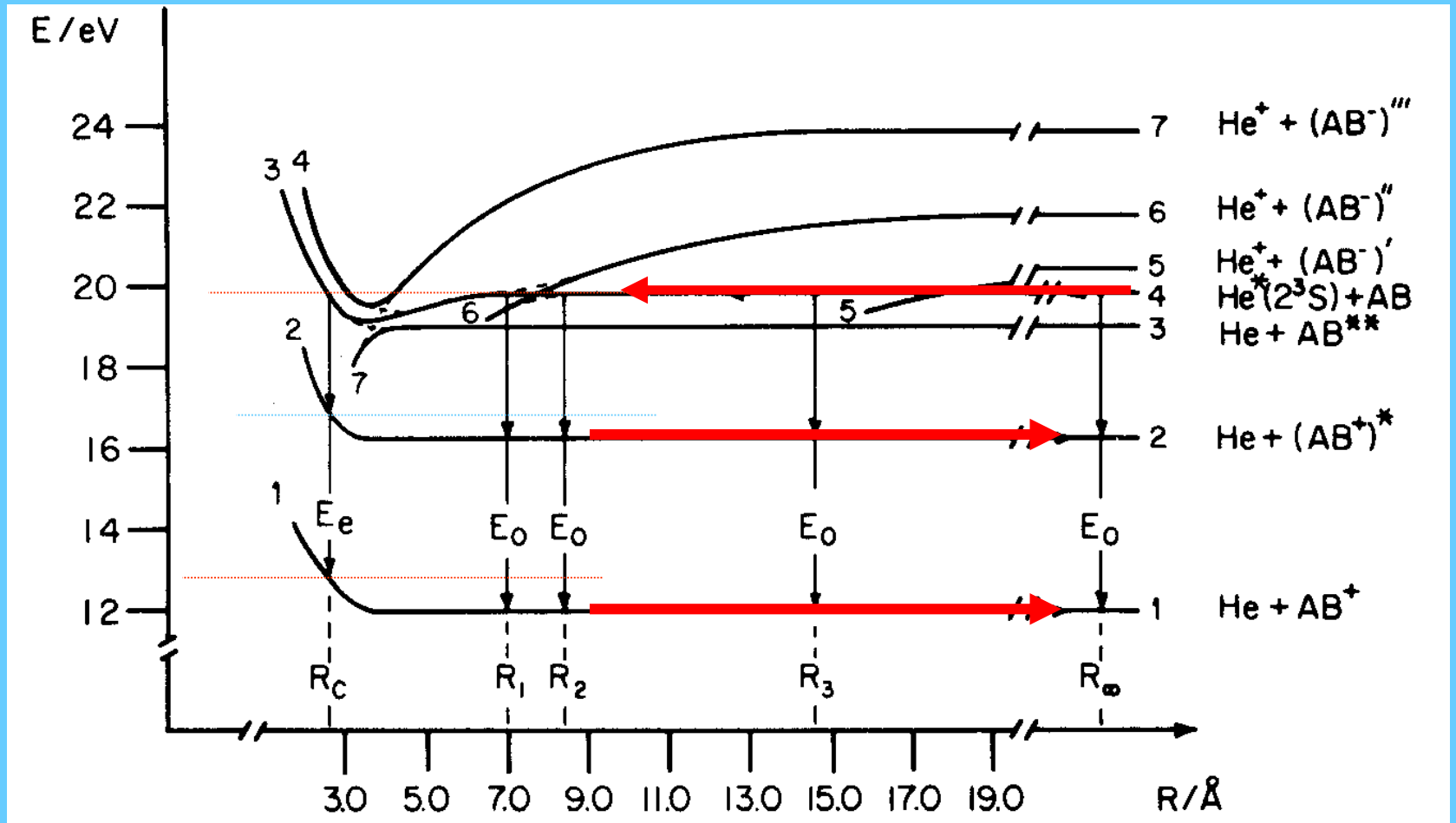

FIG. 2. Potential-energy curve model for Penning ionization showing the influence of other potential curves on the Penning ionization process (see text).

Energetics

$X^* + AB \rightarrow [X^*AB] \rightarrow [XAB^+ + e^-] \rightarrow X + AB^+ + e^-$

$V^*(R) \rightarrow V^+(R)$

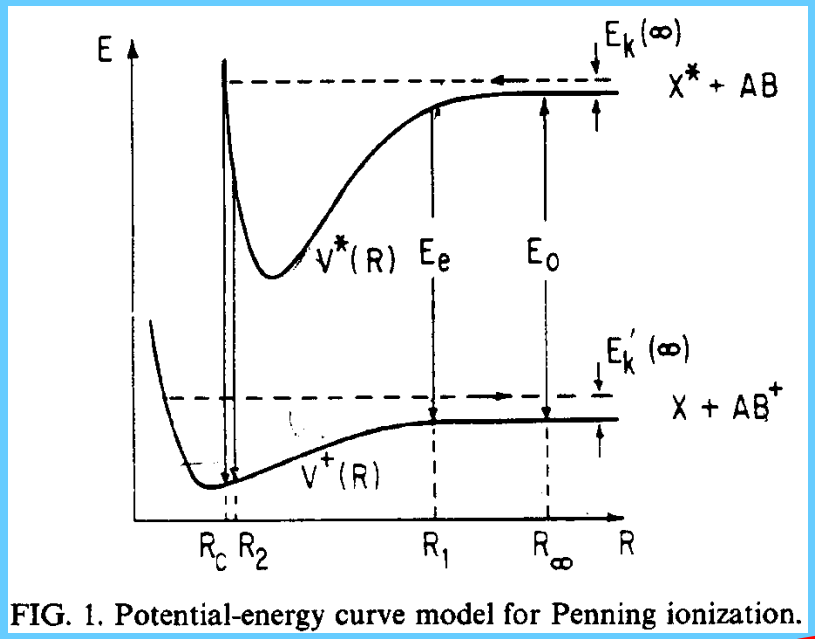

FIG. 1. Potential-energy curve model for Penning ionization.

INCOMING CHANNEL

OUTGOING CHANNEL

E before = E after

$$E = V^*(R) + E_k(\text{infinity}) = V^+(R) + E_k'(\text{infinity}) + E_e$$

$$E_e = V^*(R) + E_k(\text{infinity}) - V^+(R) - E_k'(\text{infinity})$$

Polarization of ejected electrons

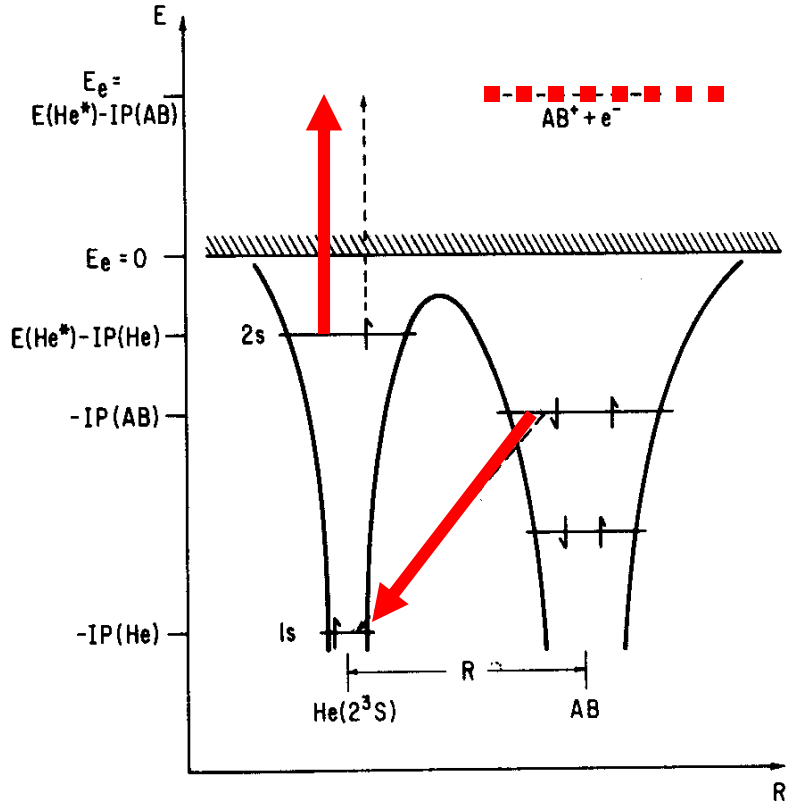

FIG. 3. Schematic representation of electron orbitals demonstrating the two-electron exchange mechanism for the Penning process $He(2^3S) + AB \rightarrow He(1^1S) + AB^+ + e^-$.

It was suggested , and it is now generally believed, that in PI the ionized electron originates with the metastable projectile irrespective of its spin.
Simultaneous, <u>two-electron</u>, exchange/ejection mechanism see Fig. 3.

EXPERIMENTS

Hemispherical electron energy analyzer

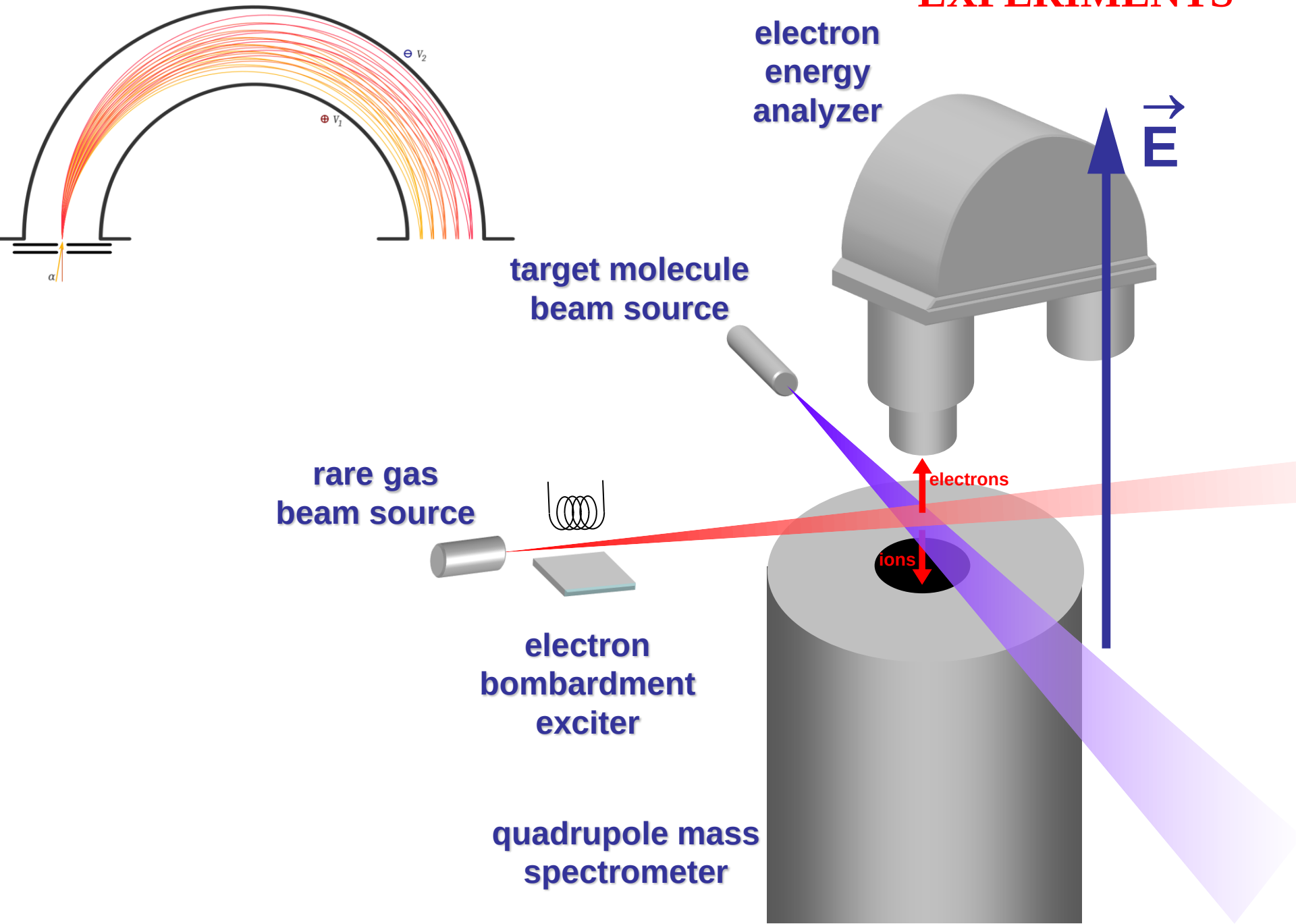

$He^*(2^1S, 2^3S) + Ar \rightarrow He + Ar^+(^2P_{3/2}, {}^2P_{1/2}) + e^-$

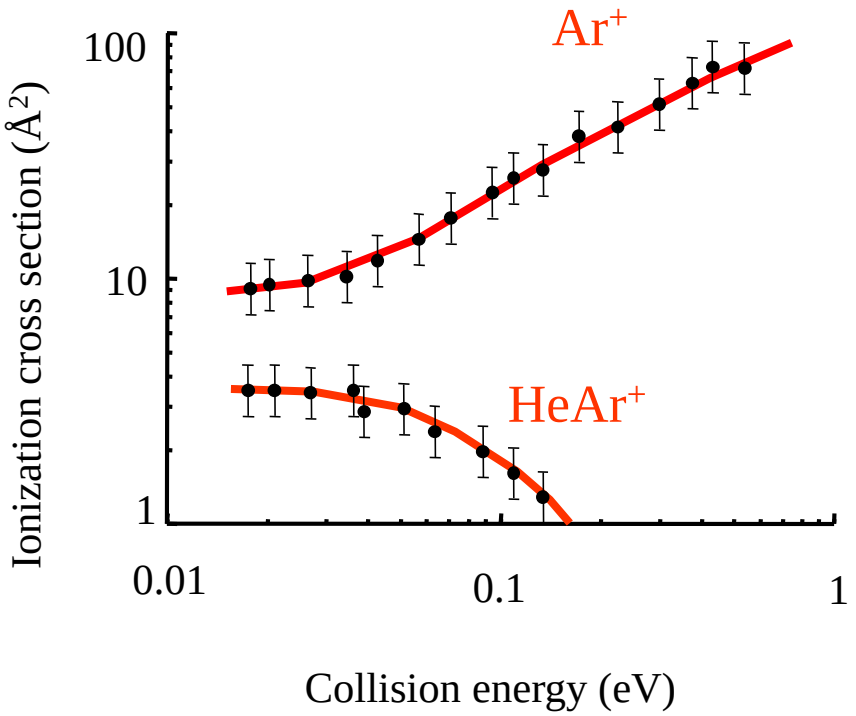

$He^*(2^3S) + Ar \rightarrow He + Ar^+(^2P_{3/2}) + e^-$ $\sigma_{3,3/2}$

$He^*(2^3S) + Ar \rightarrow He + Ar^+(^2P_{1/2}) + e^-$ $\sigma_{3,1/2}$

$He^*(2^1S) + Ar \rightarrow He + Ar^+(^2P_{3/2}) + e^-$ $\sigma_{1,3/2}$

$He^*(2^1S) + Ar \rightarrow He + Ar^+(^2P_{1/2}) + e^-$ $\sigma_{1,1/2}$

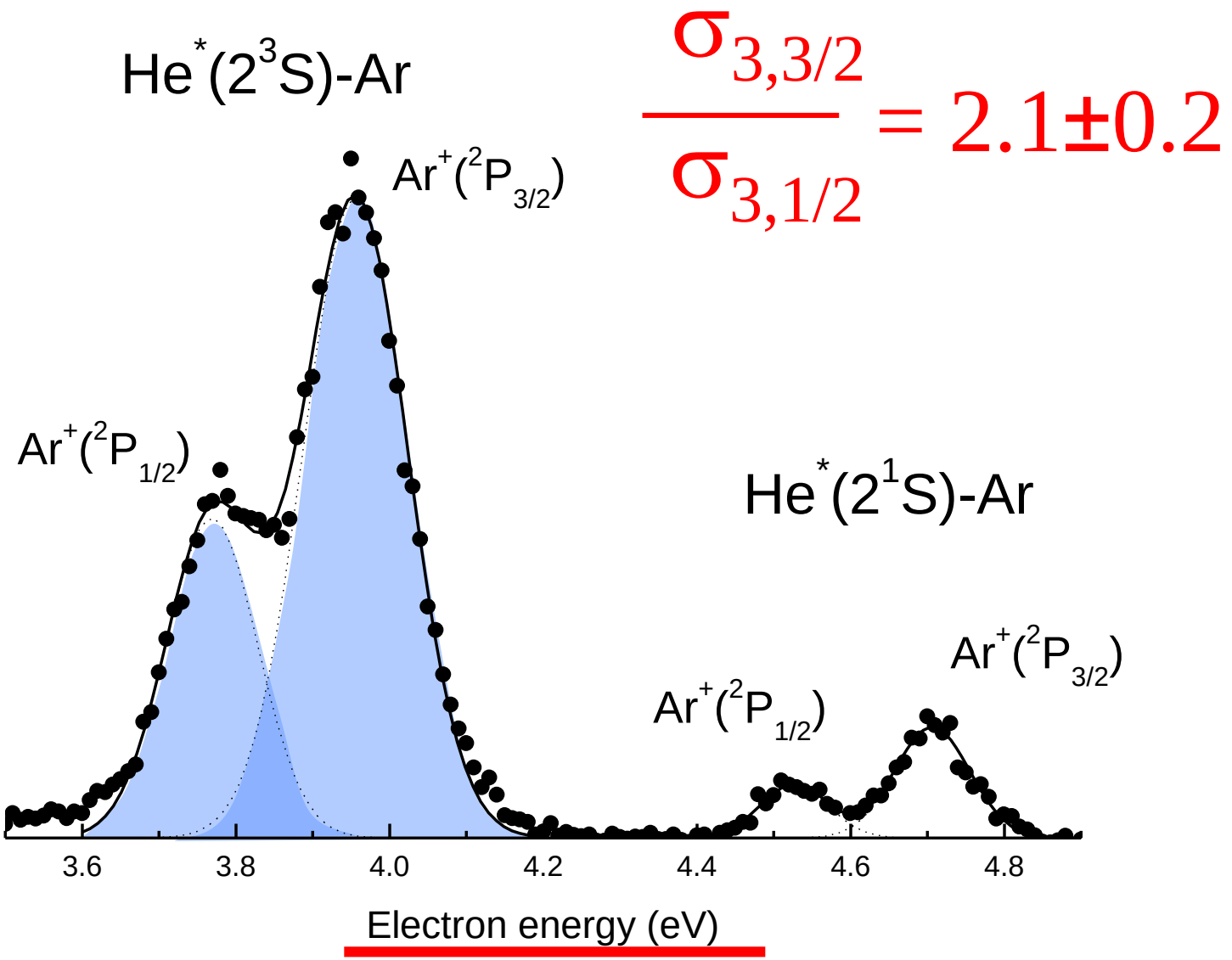

$$\frac{\sigma_{3,3/2}}{\sigma_{3,1/2}} = 2.1 \pm 0.2$$

B. Brunetti, P. Candori, S. Falcinelli, B. Lescop,
G. Liuti, F. Pirani, F. Vecchiocattivi (2005) to be published

$$He^*(^3S) + Ar \rightarrow [He\text{-}Ar]^* \rightarrow [He\text{-}M]^+ + e^-$$

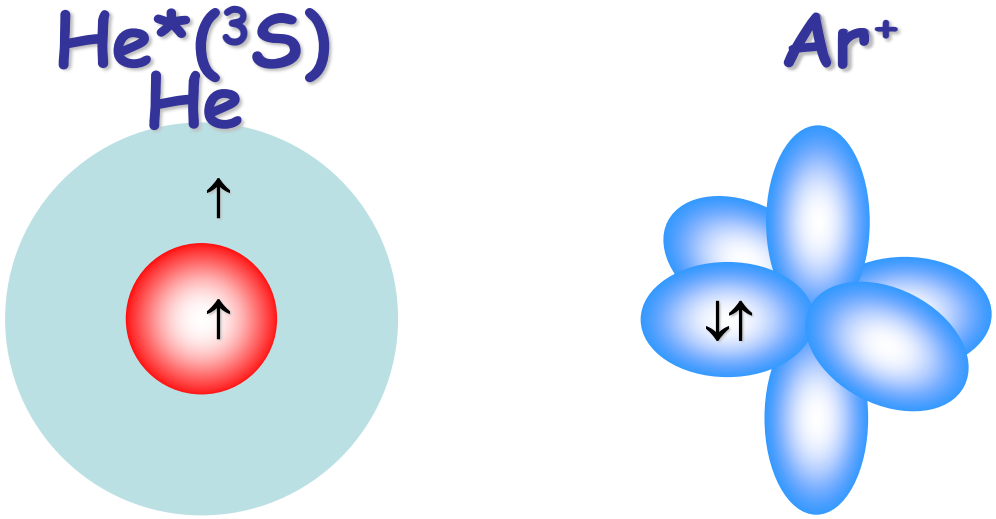

$$Ne^*(^3P_{2,0}) + Ar \rightarrow [Ne\text{-}Ar]^* \rightarrow [Ne\text{-}M]^+ + e^-$$

$Ne^*(^3P_{2,0})$

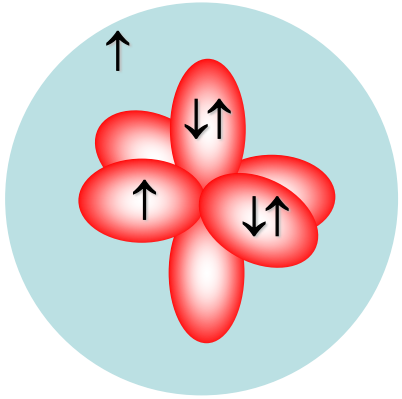

Ar^+

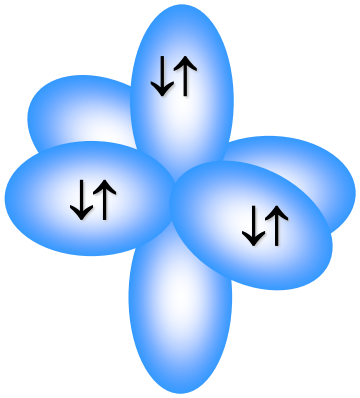

1993

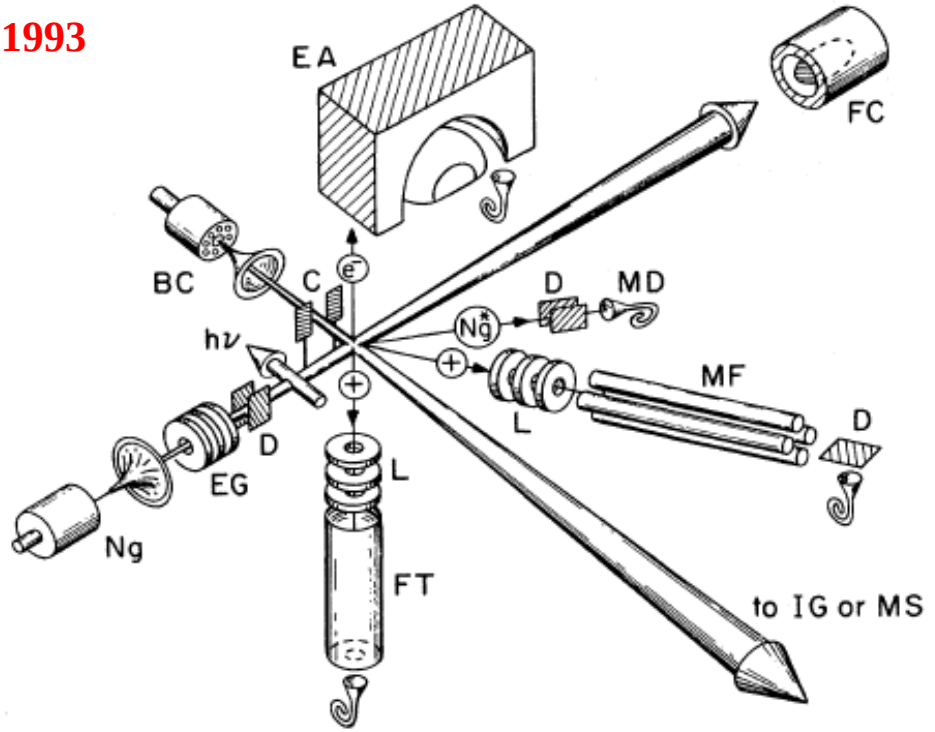

FIG. 1. Schematic illustration of a crossed-beam apparatus for the study of Penning ionization. Ng and BC—nozzle-skimmer assemblies for the excited atom and partner molecule beams, respectively; EG—electron gun used to excite Ng to Ng*; D—electrostatic deflector; $h\nu$—photons for state selection; C—chopper for modulation of BC beam; EA—electrostatic energy analyzer for Penning electrons; FC—Faraday cup metastable beam monitor; MD—metastable detector (electron multipler); L—electrostatic lens/retarding field assembly; MF—quadrupole mass filter; IG or MS—molecular-beam monitor, either ion gauge or mass spectrometer; FT—ion flight tube for coincidence measurements. The curly objects are channel electron multipliers. Not indicated are various collimators and plates surrounding the intersection region for total ion collection experiments.

Molecular-beam studies of Penning ionization

P. E. Siska

Department of Chemistry, University of Pittsburgh, Pittsburgh, Pennsylvania 15260

Reviews of Modern Physics, Vol. 65, No. 2, April 1993

TABLE I. Characteristics of the metastable noble-gas atoms.[a]

Atom	Electron configuration	State	Excitation energy E_* (eV)	Ionization energy (eV)	Lifetime (s)	Dipole polarizability (Å^3)
He	$1s2s$	$2\,^1S_0$	20.6158[b]	3.9716[b]	0.0197[c], 0.0195[d]	11.8.9[e]
		$2\,^3S_1$	19.8196[b]	4.7678[b]	9000[f], 7900[g]	46.9[e]
Ne	$2p^5 3s$	$^3P_0$	16.7154[h]	4.8491[b]	430[i]	
		$^3P_2$	16.6191[h]	4.9454[h]	> 0.8[c], 24.4[i]	27.8[i]
Ar	$3p^5 4s$	$^3P_0$	11.7232[k]	4.0364[k]	44.9[i]	
		$^3P_2$	11.5484[k]	4.2112[k]	> 1.3[c], 55.9[i]	47.9[j]
Kr	$4p^5 5s$	$^3P_0$	10.5624[l]	3.4372[l]	0.49[i]	
		$^3P_2$	9.9152[l]	4.0844[l]	> 1[c], 85.1[i]	50.7[j]
Xe	$5p^5 6s$	$^3P_0$	9.4472[m]	2.6826[m]	0.078[i]	
		$^3P_2$	8.3153[m]	3.8145[m]	150.0[i]	63.6[j]

Differential elastic scattering of He* (2¹S) by Ar, Kr, and Xe: Repulsive rainbows and optical potentials

1978

D. W. Martin,[a] R. W. Gregor, R. M. Jordan, and P. E. Siska[b]

Department of Chemistry, University of Pittsburgh, Pittsburgh, Pennsylvania 15260

(Received 1 June 1978)

J. Chem. Phys. 69(6), 15 Sept. 1978

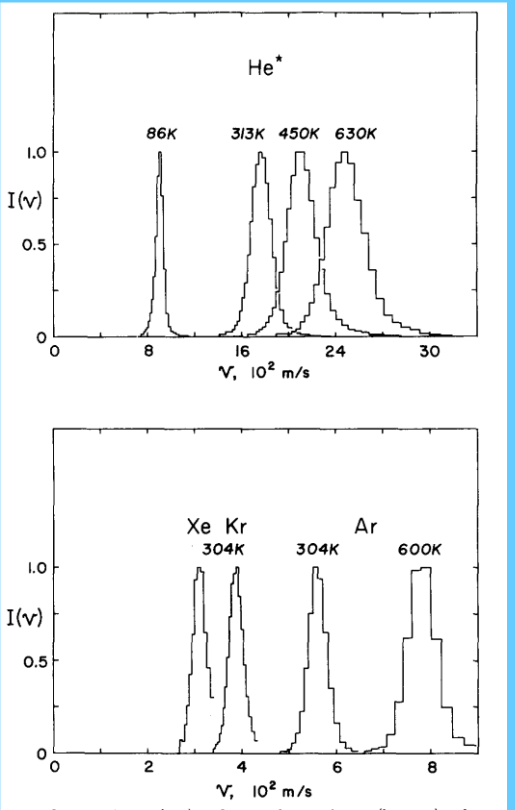

FIG. 2. He* beam (top) and ground state beam (bottom) velocity distributions derived from time-of-flight measurements. The Kr and Xe distributions do not go to zero at large v because of a background effect (see text).

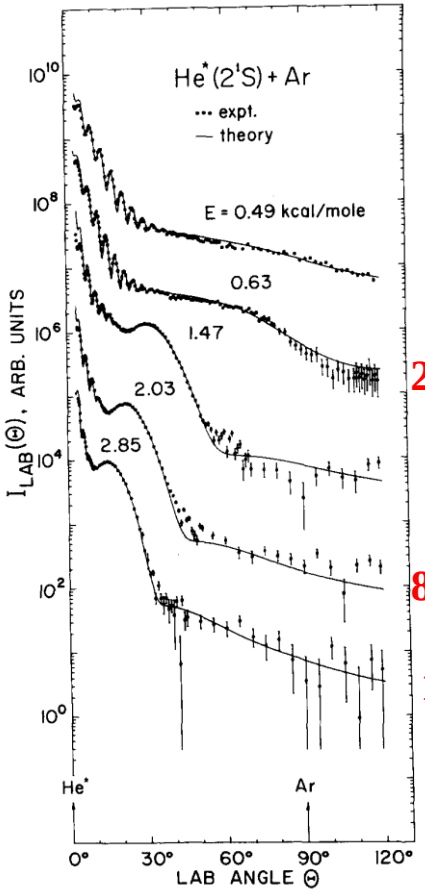

21meV

27meV

64meV

88meV

124meV

FIG. 3. Laboratory angular distributions of He*(2¹S) scattered by Ar. E is the most probable collision energy (1 kcal/mole = 43.36 meV). Error bars represent two standard deviations calculated from statistical errors only. Solid curves are calculated from an optical potential.

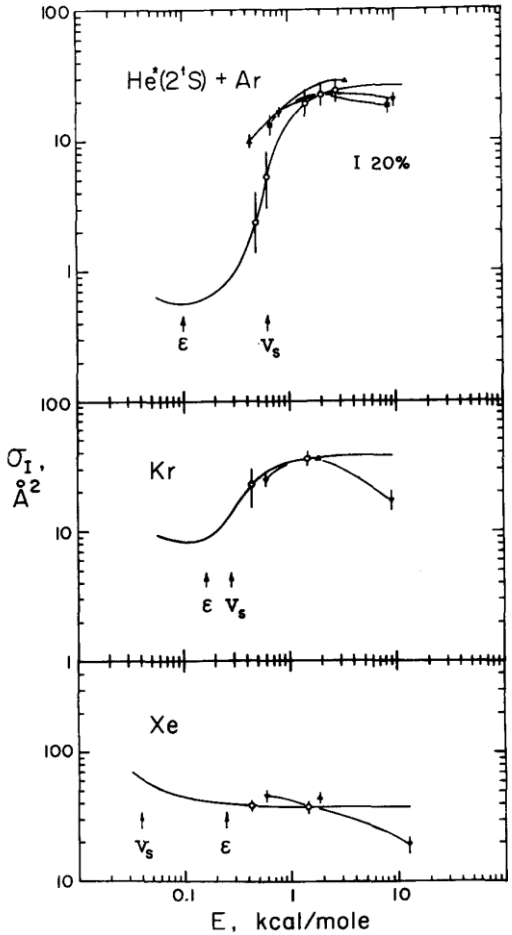

FIG. 13. Total ionization cross section energy dependence: —o— predicted in this work; ▲—▲, Ref. 49; ▼—▼, Ref. 48; ■—■, Ref. 47. For clarity, the many experimental points have been represented by smooth curves.

Experiment

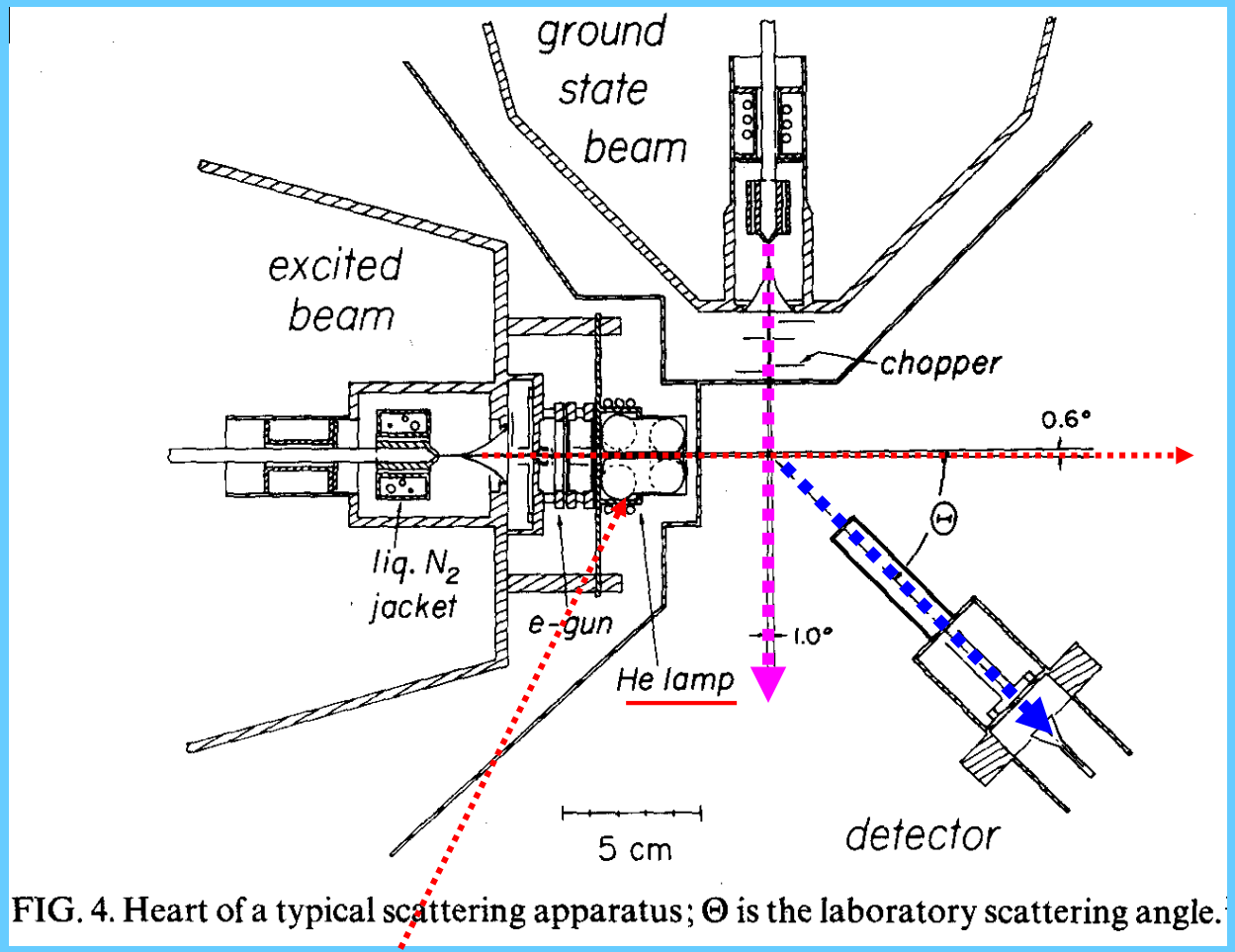

FIG. 4. Heart of a typical scattering apparatus; Θ is the laboratory scattering angle.

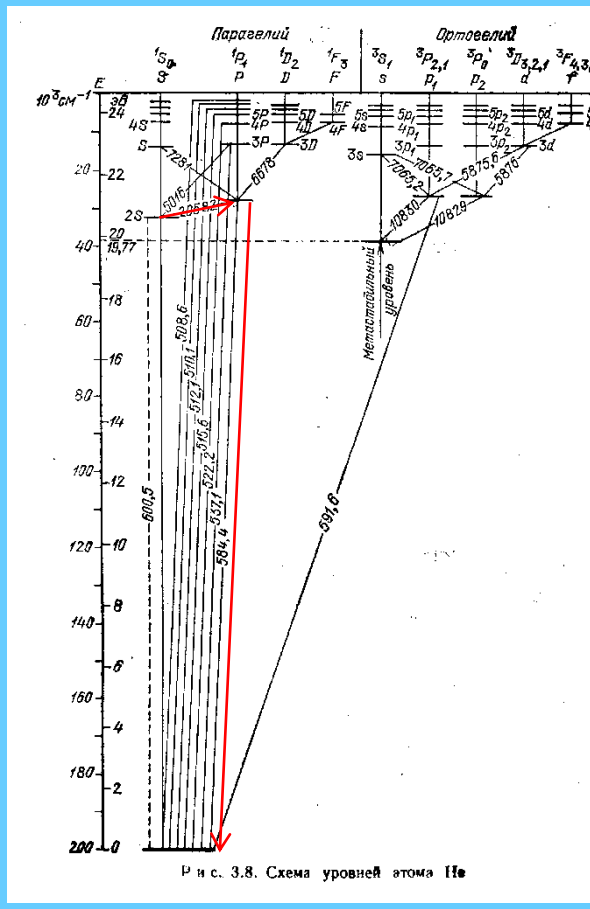

Рис. 3.8. Схема уровней атома He

$He^*(2^1S)$ metastables are removed from the He^* beam
using a quench lamp by the following optically allowed processes:

$He^*(2^1S) + h\nu(2.06\mu m) \rightarrow He^*(2^1P) \rightarrow He(1^1S) + h\nu(58.44nm)$

Elastic scattering experiments

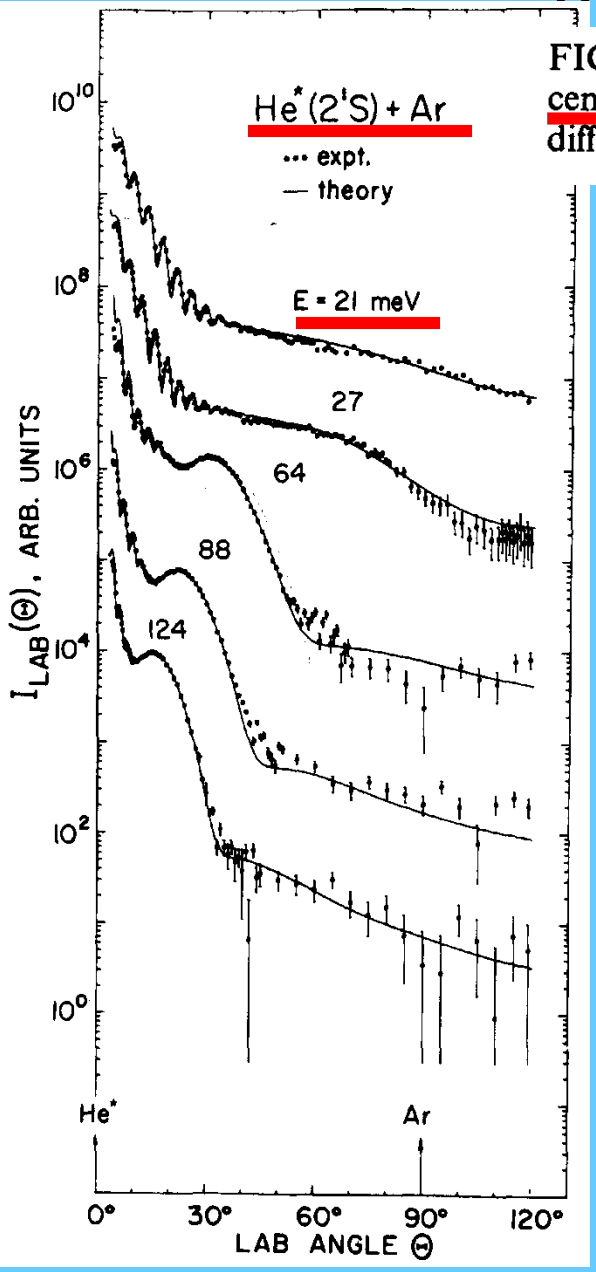

FIG. 6. Laboratory angular distributions of He*(2¹S) scattered by Ar at different center-of-mass collision energies (adapted from ref. 144). The solid curves are relative differential cross sections calculated from an optical potential.

Relative differential cross sections

The angular distribution data (**points**) at various center-of-mass collision energies obtained in $He^*(2^1S)$ + Ar system.

Solid curves - relative differential cross sections calculated from an optical potential.

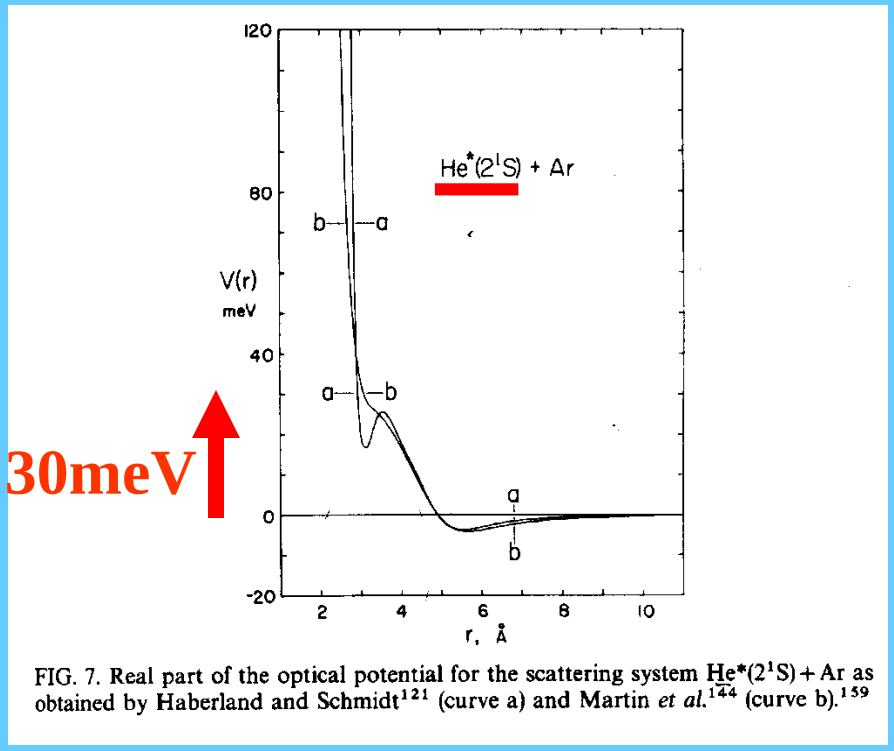

FIG. 7. Real part of the optical potential for the scattering system He*(2¹S) + Ar as obtained by Haberland and Schmidt[121] (curve a) and Martin *et al.*[144] (curve b).[159]

Elastic scattering – total cross section

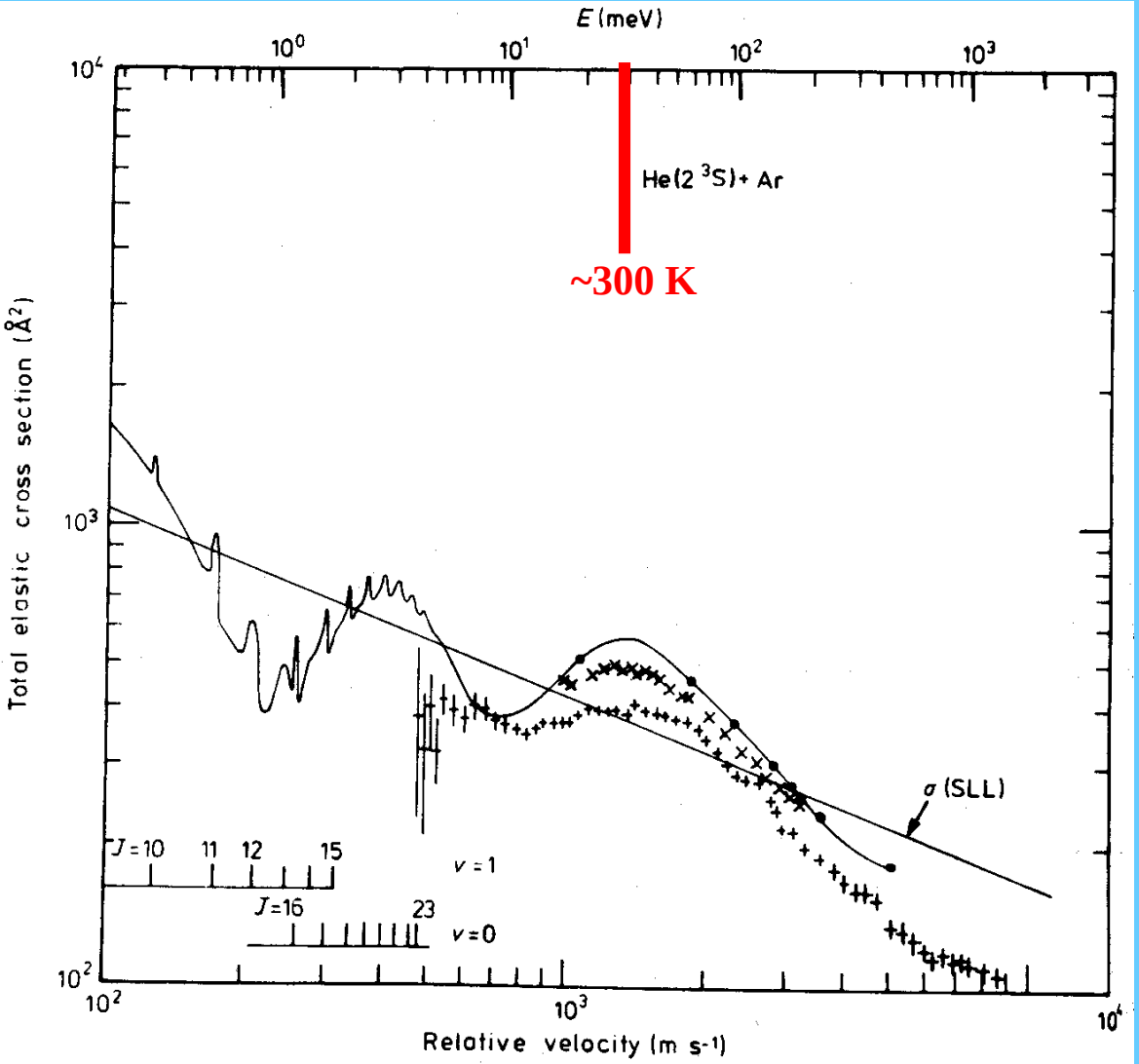

FIG. 18. Calculated velocity dependence of the total elastic cross section for He*(2^3S)+Ar compared with experimental data (×, Rothe *et al.*;[176] +, Trujillo[177]).[118] The straight line is calculated on the basis of the Schiff–Landau–Lifshitz (SLL) approximation. The positions of the orbiting resonances for (v,J) quantum numbers are also shown.

Inelastic scattering - Contour diagram

Forward scatering with an energy 6kcal/mol=0.26eV release into translation

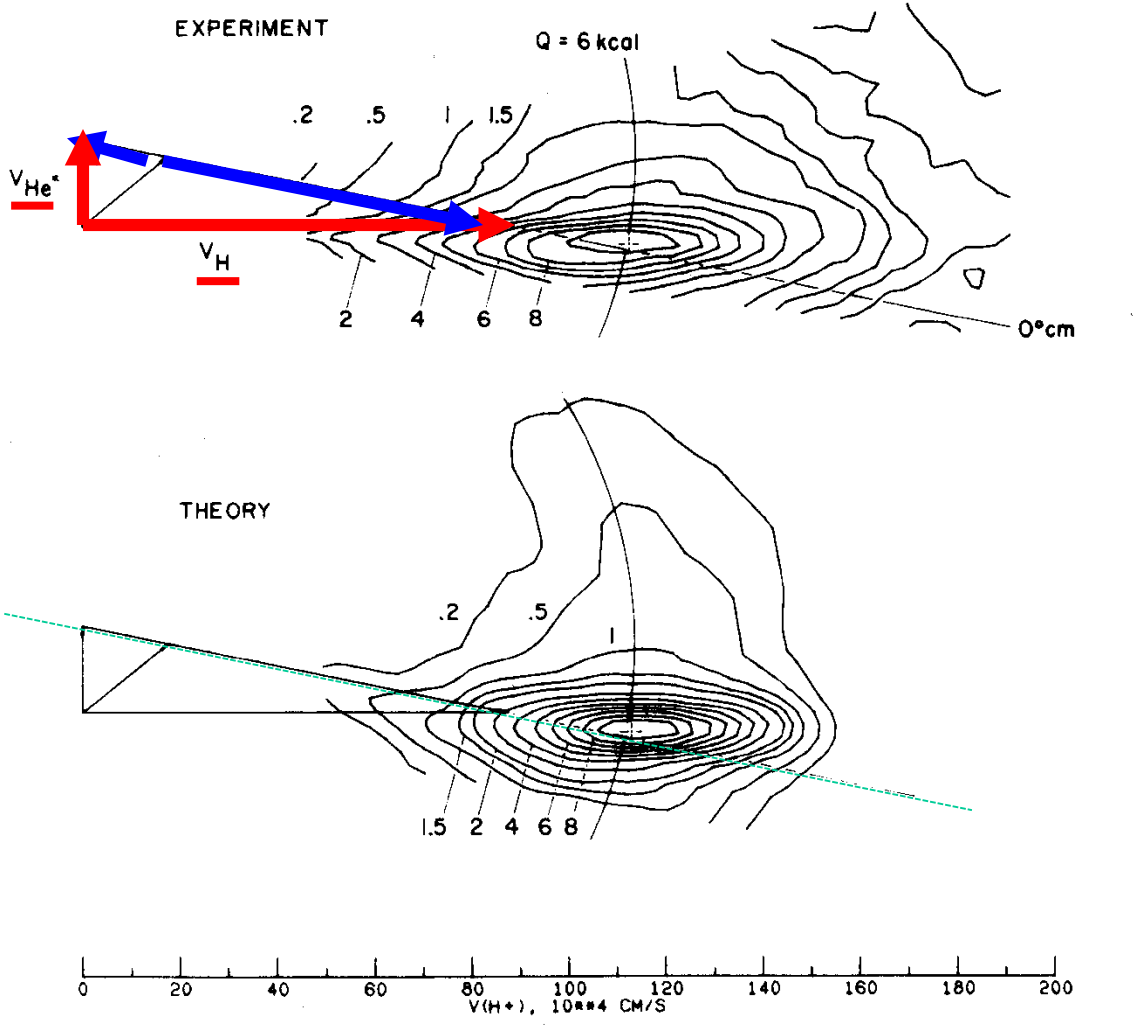

FIG. 14. Experimental and theoretical center-of-mass polar velocity angle intensity maps for H^+ from $He^*(2^1S) + H$ scattering.[152]

ELECTRON SPECTRUM

Rev. Mod. Phys., Vol. 65, No. 2, April 1993

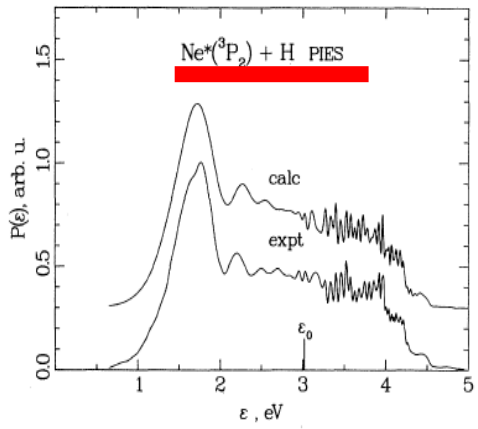

FIG. 4. Electron spectrum from the Penning ionization of H atoms by Ne*, experimental data of Lorenzen *et al.* (1983) compared to calculations of Khan *et al.* (1991b). The smooth structure to the left of ε_0 is assigned to the rainbow effect, while the fine structure to the right reflects the rovibrational states of the NeH^+ associative ion. The calculated curve has been shifted upward by 0.3 units for presentation.

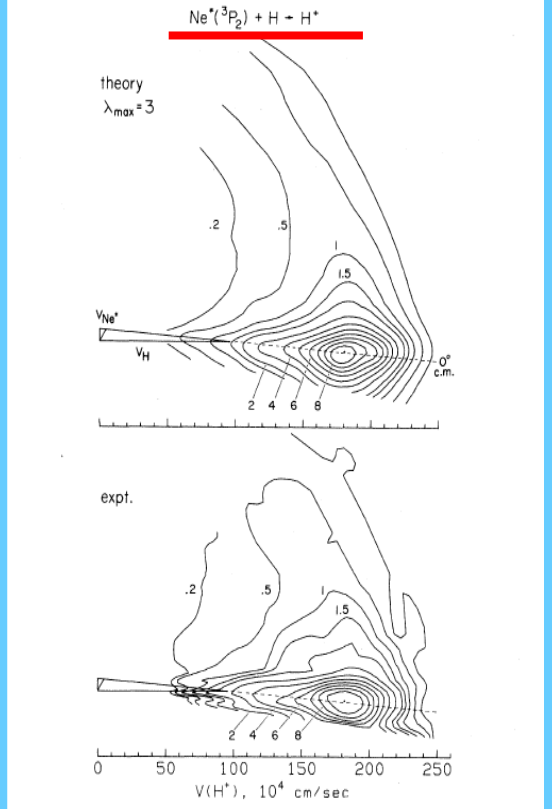

FIG. 5. Velocity-space center-of-mass intensity contour maps of scattered H^+ from Ne^*+H Penning ionization, at $E=10.4$ kcal/mol, from Khan *et al.* (1991b). Both the experimental and the calculated maps are normalized to 10 at the peak. The maps reflect strong forward scattering with substantial translational energy release. The calculations include angular momentum sharing between the Penning electron and the atoms to a maximum of $3\hbar$ ($\lambda_{max}=3$).

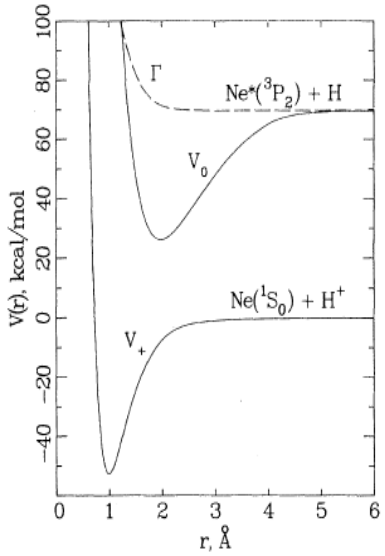

FIG. 6. Potential curves for Ne^*+H used in the calculations of Figs. 4 and 5. V_0 and Γ are determined by fitting the PIES and PI angle-energy distribution data, while V_+ was taken from the *ab initio* study of Rosmus and Reinsch (1980).

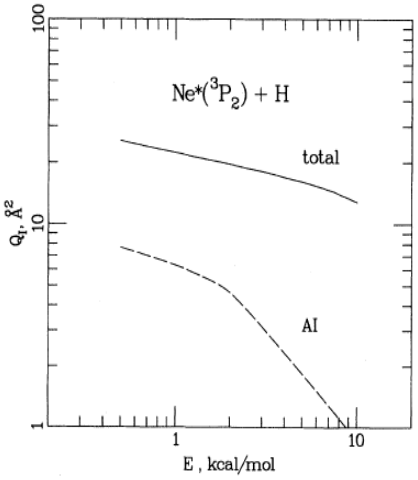

FIG. 8. Predicted total and associative ionization cross sections for Ne^*+H using the potentials of Fig. 6. The AI cross sections include qAI products with predissociation lifetimes greater than 10 μs.

Molecular-beam studies of Penning ionization

P. E. Siska

Department of Chemistry, University of Pittsburgh, Pittsburgh, Pennsylvania 15260

Molecular-beam experiments have exposed a new wealth of detail on the general reaction $A^*+B \rightarrow A+B^++e^-$ first suggested by Penning in 1927. The new capabilities not available to traditional swarm techniques include mass and electron spectroscopy on the reaction products and angle-resolved measurements of the scattering of both reagents and products. These new results have stimulated the recent development of both the electronic structure and the dynamical theories necessary for a first-principles description of at least the simplest of these reactions, those involving small atomic and diatomic species B. Recent progress in both experiment and interpretation is critically reviewed, and the prospects for attaining a global understanding of Penning ionization in larger systems are assessed.

Inelastic scattering experiments

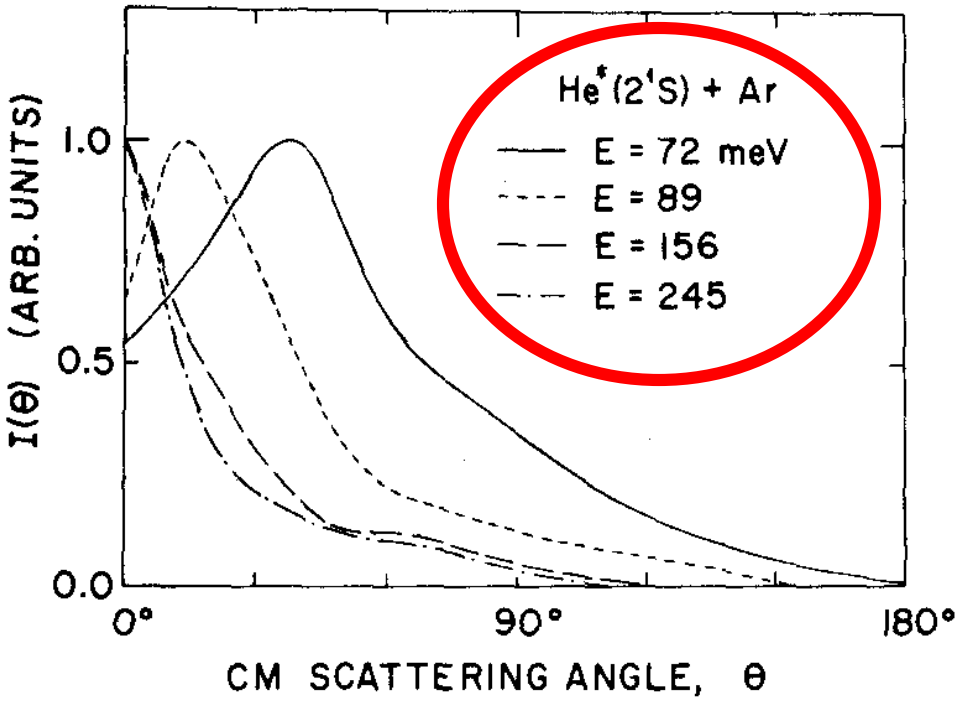

FIG. 12. Derived center-of-mass angular distributions for the Ar^+ Penning ion from $He^*(2^1S) + Ar$ scattering (adapted from ref. 138).

Inelastic scattering experiments

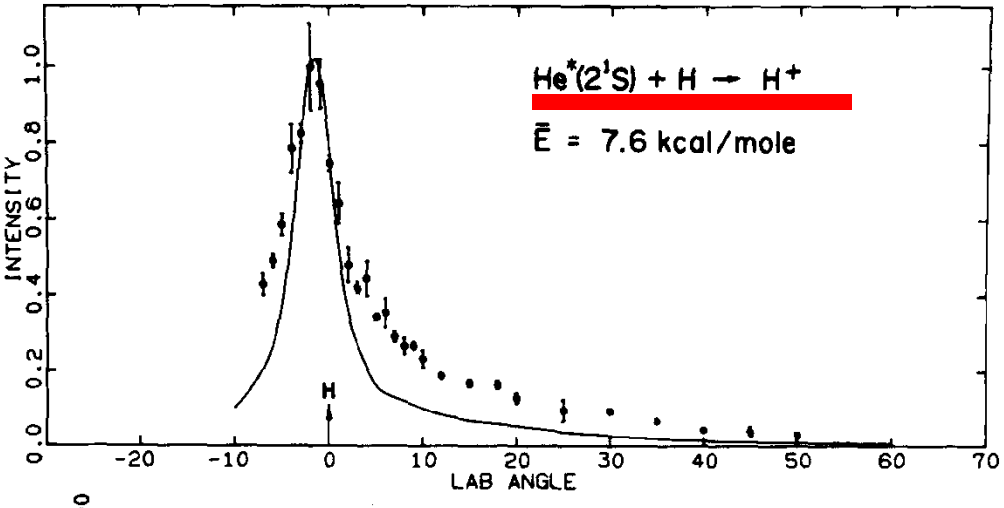

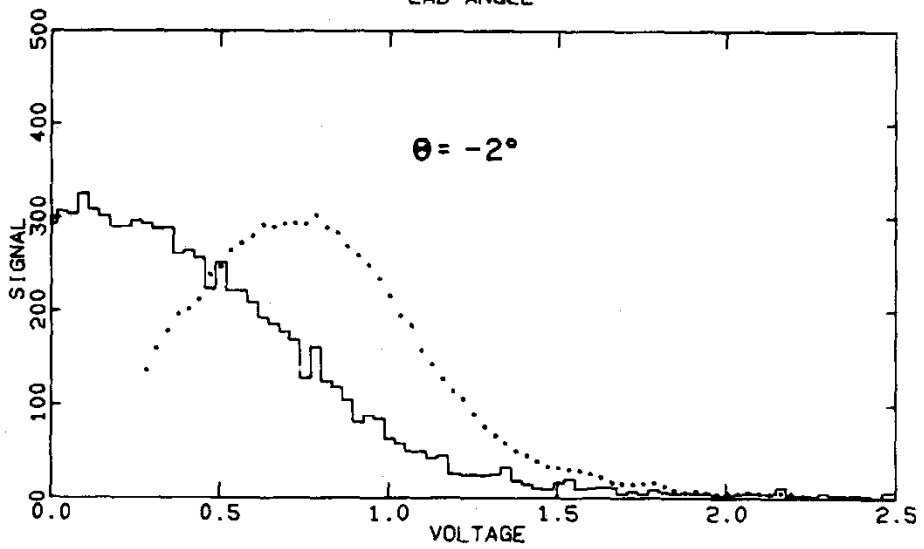

FIG. 13. Top: laboratory angular distributions of H^+ produced in $He^*(2^1S)+H$ collisions. Bottom: retarding potential curve (histogram) and laboratory energy distribution (points) of H^+ at the peak of the angular distribution.[152]

Experiments

Stationary afterglow methods

Flowing afterglow methods

Beam methods - beam-gas technique

Under single collision conditions: $I = I_0 \exp(-Nl\sigma_{abs})$

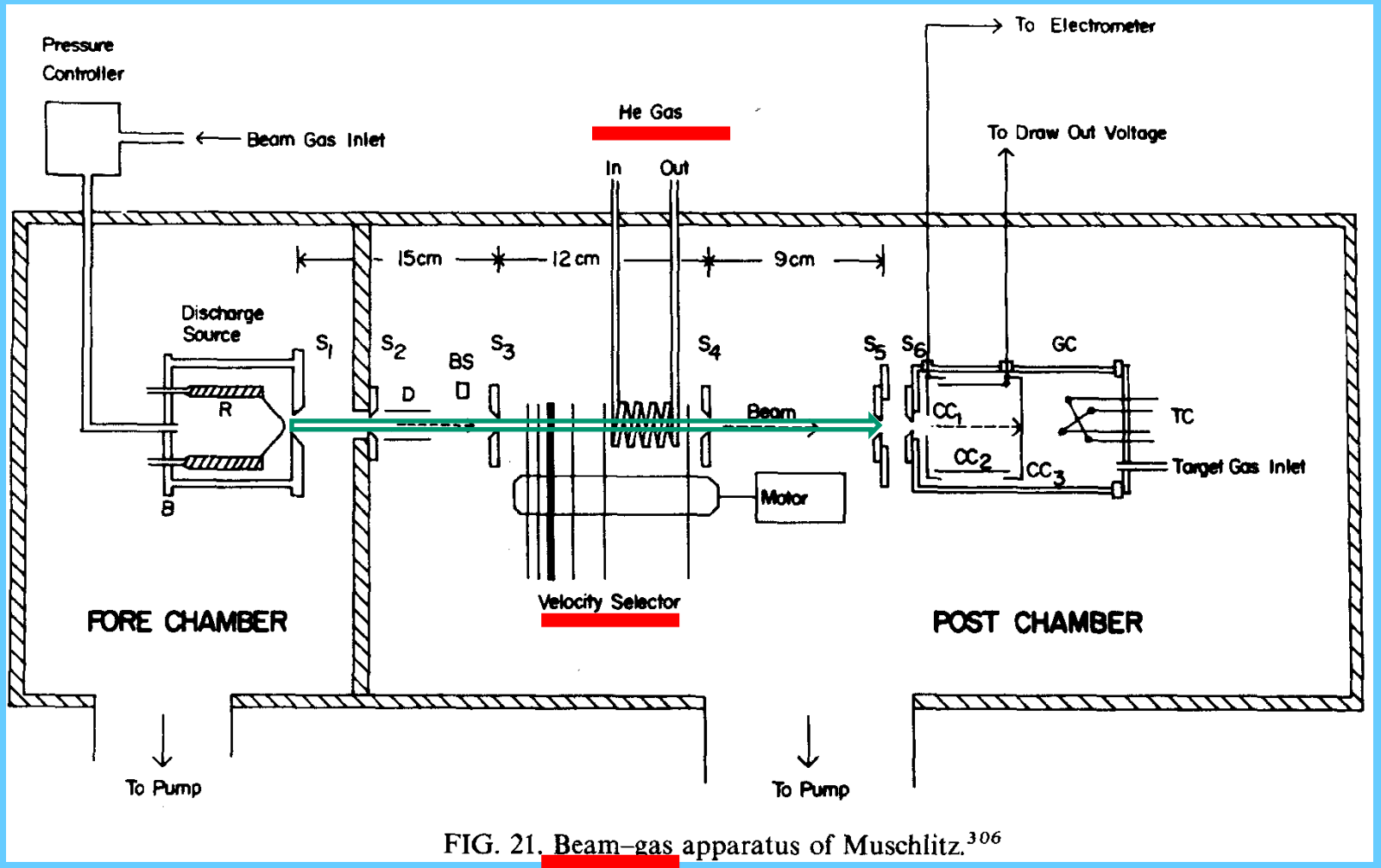

FIG. 21. Beam–gas apparatus of Muschlitz.[306]

Crossed beam

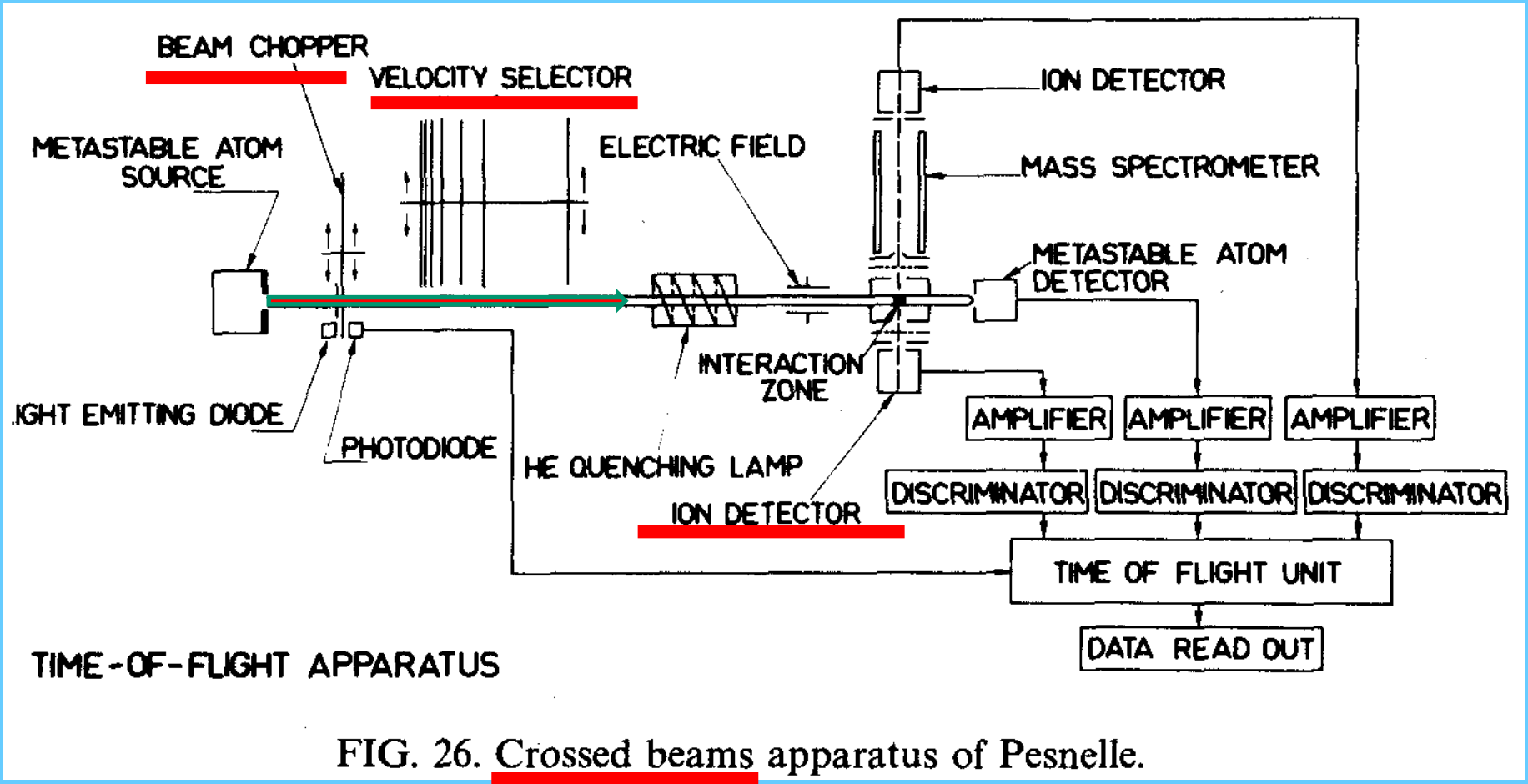

FIG. 26. Crossed beams apparatus of Pesnelle.

Merging beam techniques

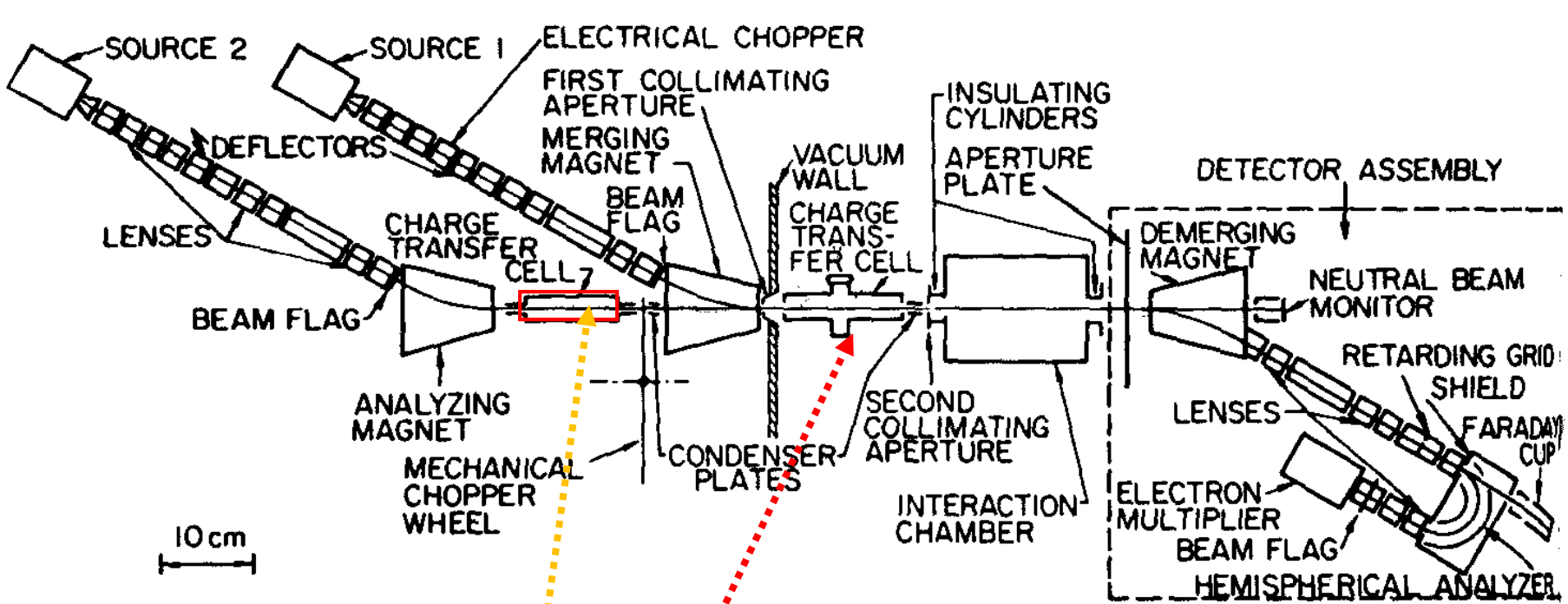

FIG. 24. Merging beams apparatus of Neynaber.

Fast rare-gas atoms are produced in resonant charge transfer reactions with identical rare-gas
Fast rare-gas metastables are produced in charge transfer reactions with appropriate alkali metal

Charged particles are produced …. manipulated and by magnets directed towards axis of the …
by charge transfer to identical rare gas atoms or other atoms beams of neutral particles are formed …
… particles forming two merged beams with nearly identical velocities are interacting … and detected...

Data **cross section is function of interaction energy**

Total ionization cross sections for reactions of various reagents with mixed composition of He^* ???? mixed???? E.g.

$He^* + Ar \rightarrow$products , $\sigma_{TI} = 8\text{-}11\ 10^{-16}cm^2$,

$He^* + Kr \rightarrow$products , $\sigma_{TI} = 2.4\ 10^{-16}cm^2$,

$He^* + O_2 \rightarrow$products , $\sigma_{TI} = 14\ 10^{-16}cm^2$,

Total ionization cross section - without specification of collision energy, …etc

Total ionization cross section for reaction between two excited rare – gas atoms.

$He^* + He^* \rightarrow$products

$\sigma_{TI} = 80\text{-}150x10^{-16}cm^2$,

$k_{TI} = 150\text{-}220x10^{-11}cm^3s^{-1}$

Data

pozor tu chyba energia

Total ionization cross sections for reactions of various reagents with $He^*(2^1S)$

$He^*(2^1S) + Ar \rightarrow$ products , $\sigma_{TI} = 20\text{-}26\ 10^{-16} cm^2$,

$He^*(2^1S) + Kr \rightarrow$ products , $\sigma_{TI} = 30\text{-}40\ 10^{-16} cm^2$,

$He^*(2^1S) + O_2 \rightarrow$ products , $\sigma_{TI} = 30\text{-}80\ 10^{-16} cm^2$,

Total ionization cross sections for reactions of various reagents with $He^*(2^3S)$

$He^*(2^3S) + Ar \rightarrow$ products , $\sigma_{TI} = 7\text{-}10\ 10^{-16} cm^2$,

$He^*(2^3S) + Kr \rightarrow$ products , $\sigma_{TI} = 8\text{-}20\ 10^{-16} cm^2$,

$He^*(2^3S) + O_2 \rightarrow$ products , $\sigma_{TI} = 10\text{-}20\ 10^{-16} cm^2$,

Total quenching cross sections for reactions of various reagents with $He^*(2^1S)$

$He^*(2^3S) + Ar \rightarrow$ products , $\sigma_Q = 5\text{-}10\ 10^{-16} cm^2$,

Velocity dependence of total ionization cross section $He^*(2^3S)$- Ar

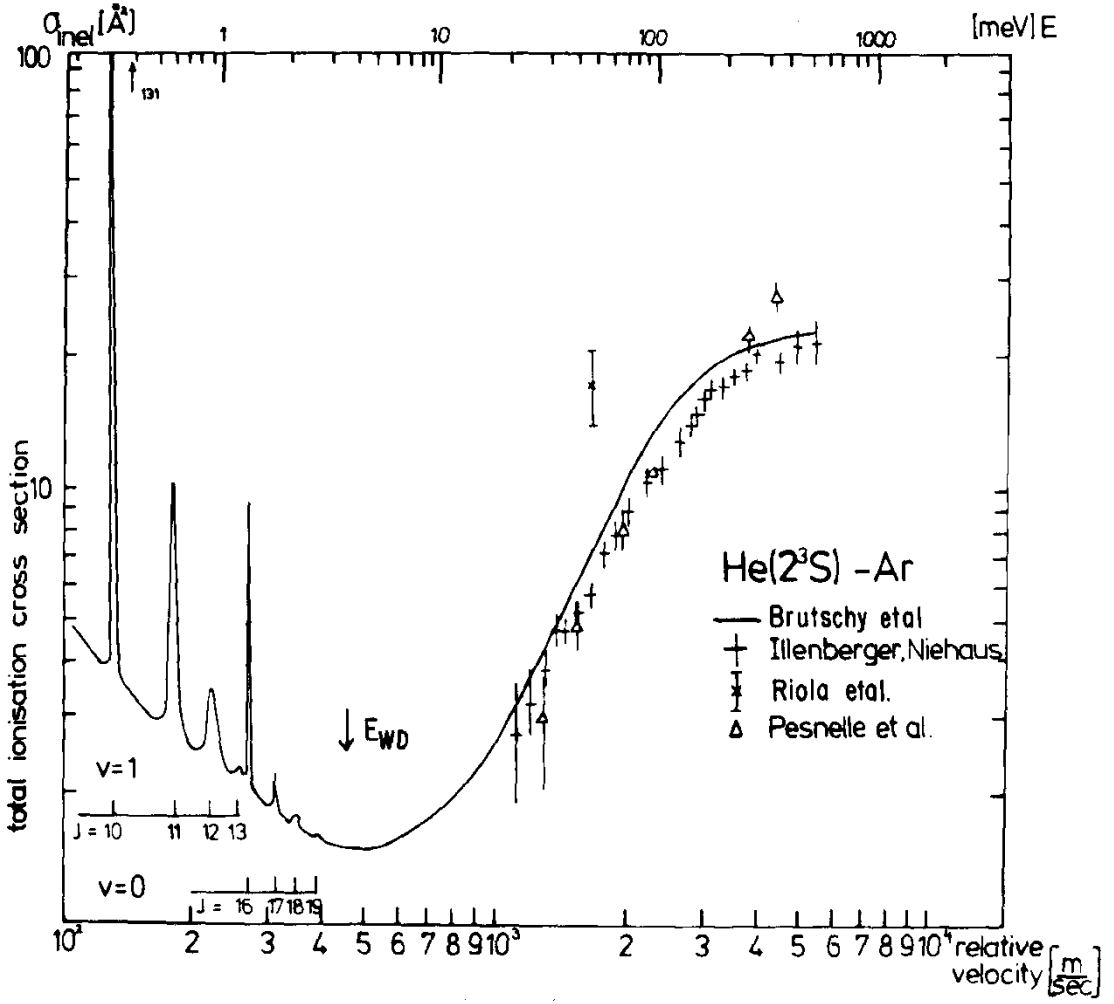

FIG. 30. Calculated total ionization cross section by Brutschy *et al.*[118] (solid curve) as a function of relative velocity for the system $He^*(2^3S)$–Ar compared with the experimental results of Illenberger and Niehaus,[160] Riola *et al.*,[374] and Pesnelle *et al.*[355] (adapted from ref. 118). The positions of the orbiting or shape resonances for (v,J) quantum numbers are also shown.

Comparison: **$He^*(2^3S)$- Ar,** **$He^*(2^1S)$- Ar**

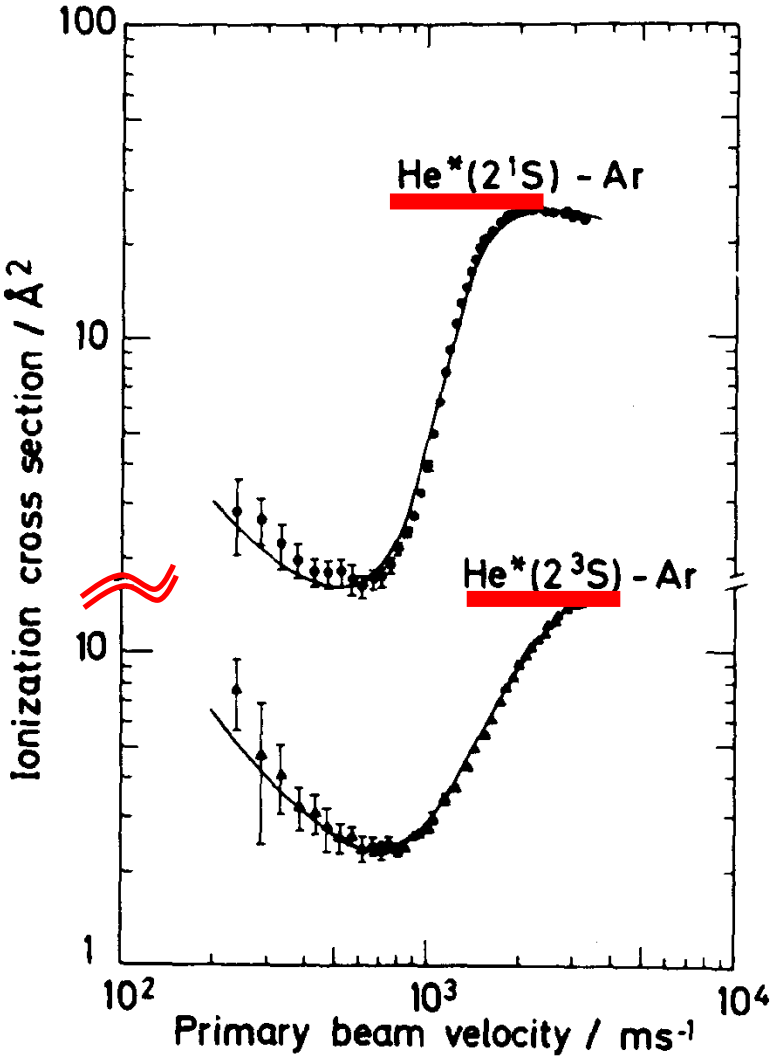

FIG. 31. Calculated velocity dependence of the total ionization cross section (solid curve) for the $He^*(2^1S)$–Ar and $He^*(2^3S)$–Ar systems compared with experimental data (points).[178]

Photoelectron Spectroscopy (PES)

E. Illenberger, J. Momigny

Gaseous Molecular Ions

An Introduction to Elementary Processes Induced by Ionization

Springer-Verlag Berlin Heidelberg GmbH

Figure 2.1 illustrates the schematic experimental arrangement for photoelectron spectroscopy. It consists of a light source, an interaction region where the photon beam collides with the gas under consideration, an electron spectrometer, and an electron detector. In conventional PES, one uses sources emitting light of a fixed wavelength (mostly 584 Å ≙ 21.22 eV produced in a He discharge lamp). The target gas is introduced in the reaction volume simply by effusing from a capillary. By scanning the electron energy analyzer, electrons of only one energy at a certain time are transmitted to the detector. By synchronizing the electron energy analyzer with a multichannel analyzer (MCA) a given channel (position on the X axis) is made to correspond to a particular electron energy, yielding a differential photoelectron spectrum, as indicated in Fig. 2.1.

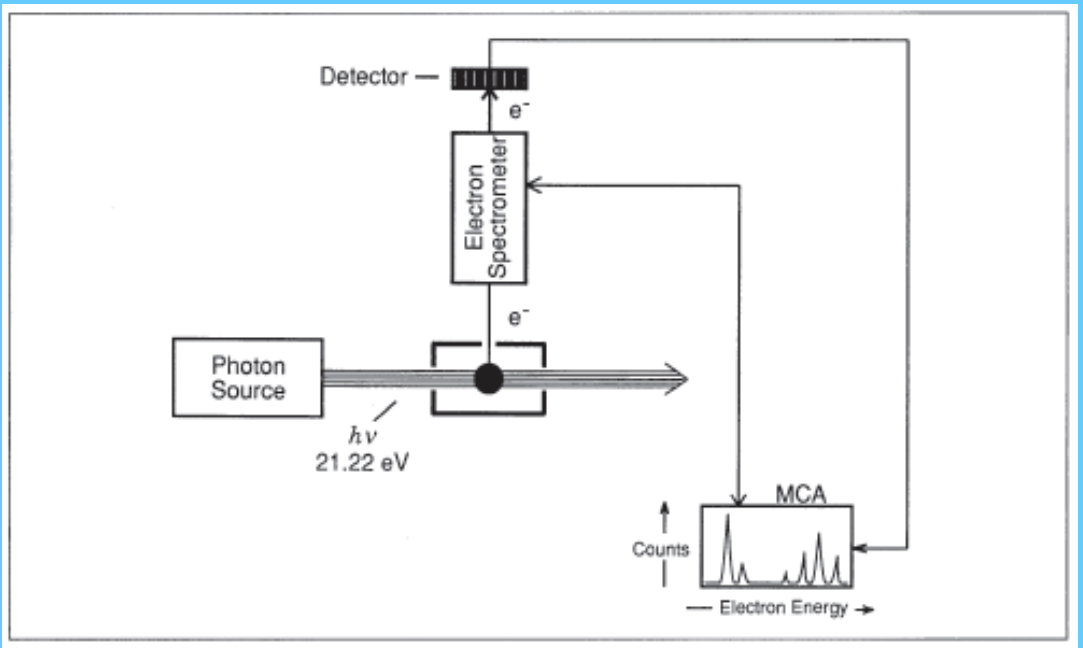

Fig. 2.1. Schematic of the experimental arrangement for photoelectron spectroscopy (PES). MCA: multichannel analyzer.

We will now briefly illustrate PES for the simple case of a diatomic molecule (Fig. 2.2). CO has 10 valence electrons with the configuration $CO\,(\sigma 2s)^2\,(\sigma^* 2s)^2\,(\pi 2p)^4(\sigma 2p)^2\,{}^1\Sigma_g^+$. As usual, $2p$, $2s$ denote the atomic orbitals of which the molecular orbitals (π, σ) are composed. Antibonding MOs are assigned by an asterix. 21.22 eV photons are able to ionize electrons from any of the three highest occupied MOs (Fig. 2.2). With the eigenvalues −14.0, −16.9, and −19.7 eV we expect photoelectrons of 7.2, 4.3, and 1.5 eV kinetic energy, respectively. Removal of an electron from the HOMO ($\sigma 2p$) generates CO^+ in its electronic ground state, and removal from $\pi 2p$ in its first electronically excited state, etc.

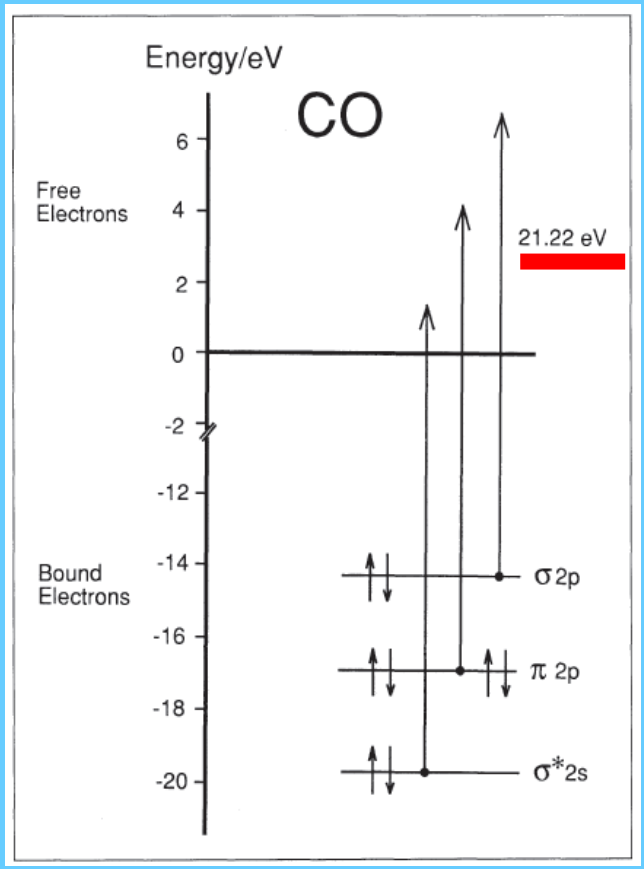

Fig. 2.2. MO diagram for the three highest occupied MOs in CO accessible by HeI radiation.

[1] The time of a vibrational period in CO is $\approx 1.54 \cdot 10^{-14}$ s; during that period the slowest photoelectron escaping from the $\sigma^* 2s$ MO travels over a distance of more than 100 Å. This exceeds the dimension of the molecule by nearly two orders of magnitude.

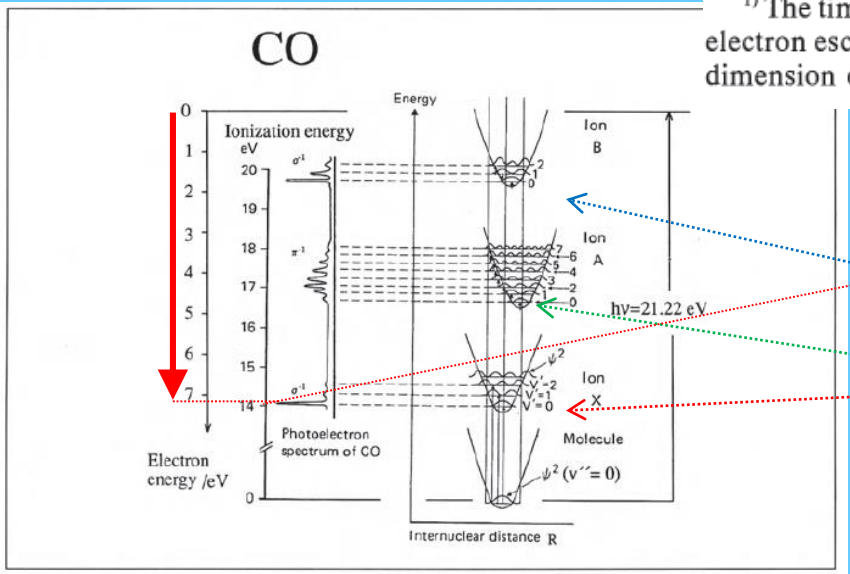

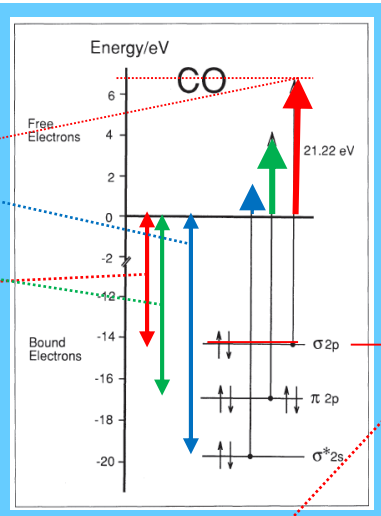

Fig. 2.3. PE spectrum of CO obtained by HeI radiation and potential energy curves for the neutral molecule and the three ionized states (adapted from [48]).

expect photoelectrons of 7.2, 4.3, and 1.5 eV kinetic energy, respectively. Removal of an electron from the HOMO ($\sigma 2p$) generates CO^+ in its electronic ground state, and removal from $\pi 2p$ in its first electronically excited state, etc.

Figure 2.3 shows the experimentally observed photoelectron spectrum and the associated potential energy curves. Since the ionization process is rapid with respect to the time of a molecular vibration, electron ejection can be represented by vertical lines in Fig. 2.3[1]). This approximation is known as the *Franck-Condon Principle*. As is obvious from Fig. 2.3, the electronic transition may lead to vibrational excitation in CO^+ in its different electronic states associated with the structures in the photoelectron spectrum. Rotational structures generally cannot be resolved in PES.

The cross section for ionization from the vibrational level v'' of the neutral molecule to a vibrational level v' in the ion is given to a good approximation [3] by the Franck-Condon Factor (FCF) which is equal to the square of the overlap integral between the respective vibrational wave functions

$$\mathrm{FCF} = |\langle \Psi_{v''} \mid \Psi_{v'} \rangle|^2 . \qquad 2.1$$

Note that this overlap integral does not vanish by orthogonality because $\Psi_{v''}$ and $\Psi_{v'}$ are vibrational wavefunctions belonging to different electronic states.

Penning ionization electron spectroscopy PIES

PIES began in 1966 with the publishing of a series of papers by VLADIMIR CERMAK on PI and AI.

Electron spectroscopy: **photoionization versus Penning ionization**

Photoionization

$h\nu + AB \rightarrow AB^+ + e^-$

Energy of ejected electron is: $E_e = E(h\nu) - [IP(AB) + E_{J,K}(AB^+)]$

$E_{J,K}(AB^+)$ - rotational and vibrational excitation energies of the product AB^+ ions

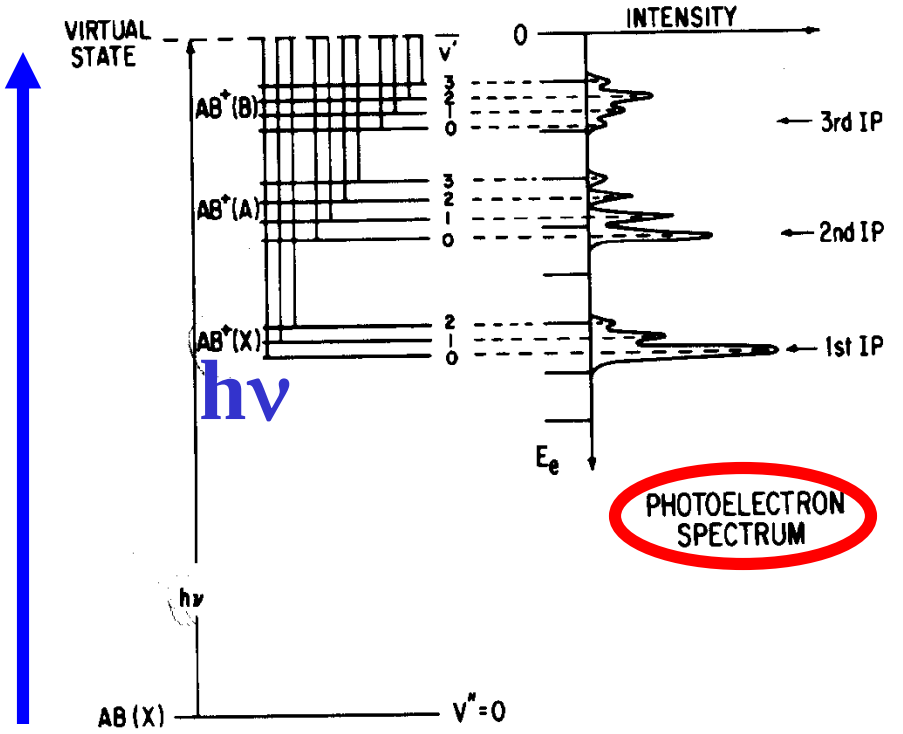

FIG. 36. Energy level diagram schematically showing the ionization of a molecule AB by a photon of energy *hν* and the populating of different vibrational states of the molecular ion AB^+. Also shown is the hypothetical photoelectron spectrum.

Photoionization can be viewed as the excitation of a ground state molecule, AB(X), by a photon, hν, into a virtual state that lies within the ionization continuum of the molecule. Relaxation (autoionization) from this virtual state then results in the formation, in this hypothetical case (Fig. 36), of three different bound ionic states of the molecule with the simultaneous ejection of electrons of energies dictated by equation (37). Rotational structure is not observed here owing to the limited resolution of the electron spectrometer.

Penning ionization electron spectroscopy PIES

Photoionization

$h\nu + H_2O \rightarrow$ ionic products + e^-

He I line 58.4 nm

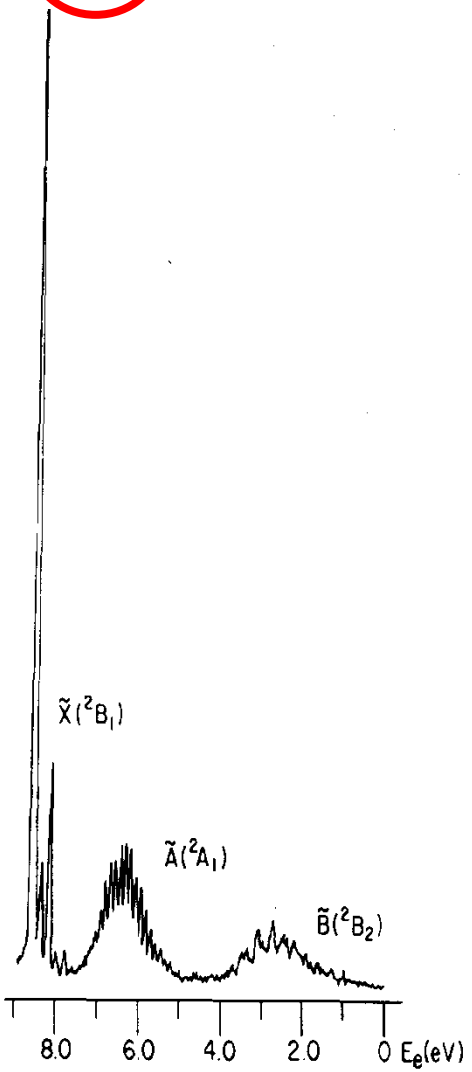

FIG. 37. Photoelectron spectrum of H_2O using the helium I, 58.4 nm, resonance line (adapted from ref. 516).

Photoionization Mass Spectrometry (PIMS)

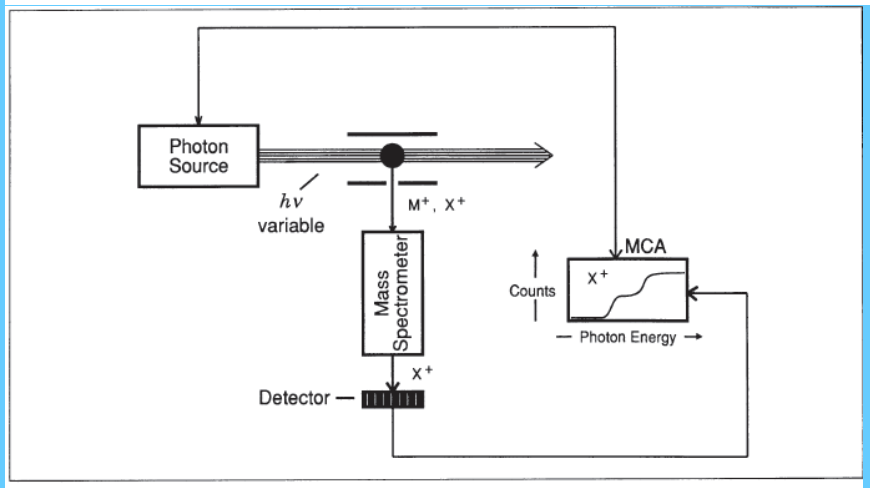

Fig. 2.4. Schematic of the experimental arrangement for photoionization mass spectrometry (PIMS). MCA: multichannel analyzer.

This method requires a tunable light source and a mass filter (Fig. 2.4). Ion yield curves are obtained by measuring the appearance of a specific ion (parent or fragment ion) as a function of the increasing photon energy. The ions created in the interaction volume are focused onto the entrance hole of the mass filter by appropriate electric fields and analyzed according to M/z.

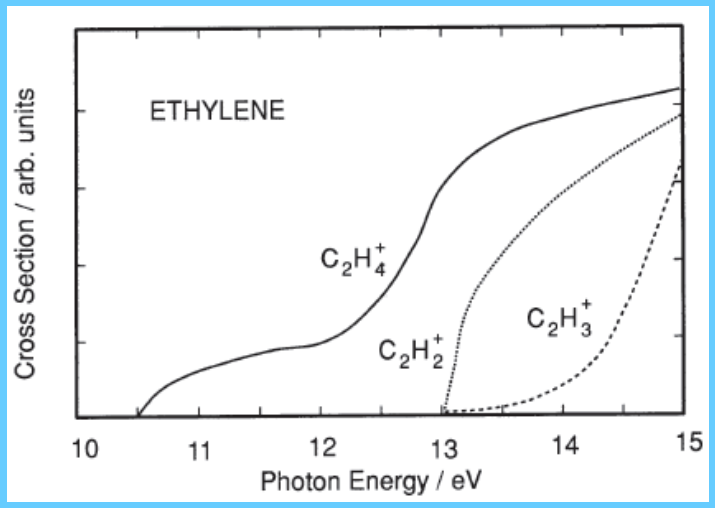

Fig. 2.5. Ion yield curves for C_2H_4 in the energy range 10-15 eV (adapted from [8]).

Figure 2.5 illustrates an experimental result for ethylene in the energy range between 10 eV to 15 eV [8]. For this system the energetic thresholds (ΔH_o) for the involved dissociative photoionization processes are well known from different experimental methods [9-12]:

$$h\nu + C_2H_4 \rightarrow C_2H_3^+ + H \qquad \Delta H_o = 13.22 \text{ eV} \qquad 2.2$$

$$\rightarrow C_2H_2^+ + H_2 \qquad \Delta H_o = 13.12 \text{ eV}. \qquad 2.3$$

From Fig. 2.5 it is apparent that the appearance energy of the two fragment ions is very close to the energetic threshold, i.e., the excess energy in reaction 2.2 and 2.3 is close to zero at the experimental appearance energy of $C_2H_3^+$ and $C_2H_2^+$.

2.3 Photoelectron-Photoion Coincidence Spectroscopy (PEPICO)

This technique combines PES and PIMS in the way that the dissociation pathways of M^+ for a defined internal energy are determined. Consider photoionization at a fixed photon wavelength

$$h\nu\ (21.22\ \text{eV}) + \text{M} \rightarrow \begin{cases} \text{M}^+ + \text{e}^- \\ \rightarrow \text{R}_1 + \text{X}^+ \\ \rightarrow \text{R}_2 + \text{Y}^+ \\ \rightarrow \ldots\ldots \end{cases} \qquad 2.5$$

If the electron spectrometer is arranged to transmit electrons of a fixed single energy, the corresponding molecular ion is created with a defined amount of internal energy given by

$$E_{\text{int}}(\text{M}^+) = h\nu - \varepsilon - IE(\text{M}), \qquad 2.6$$

with $IE(\text{M})$ the first ionization energy. If a fragment ion X^+ is then detected in coincidence with the electron, we know the internal energy of the precursor ion (M^+) from which X^+ is generated. The coincidence technique has to ensure that e^- and X^- arise from the same ionization event. By measuring coincidences at different electron energies, one can measure the appearance of X^+ as a function of the internal energy of M^+.

Figure 2.6 shows a schematic of the experimental arrangment for PEPICO. In contrast to PES a small electric field is applied in the reaction volume in order to draw out electrons and ions in opposite directions. This field will influence the electron energy resolution to some extent since photoelectrons are created across the finite thickness of the photon beam and hence at slightly different potential energies.

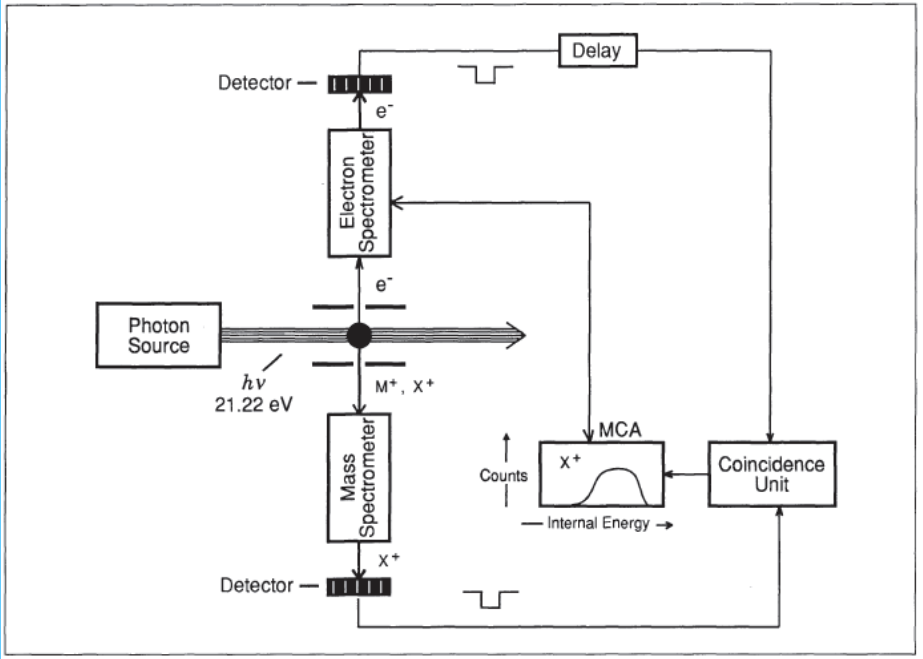

Fig. 2.6. Schematic of the experimental arrangement for photoelectron-photoion coincidence spectroscopy (PEPICO). MCA: multichannel analyzer.

The uncertainty in the exact arrival time of fragment ions due to excess translational energy from the unimolecular decomposition is the inherent limitation in distinguishing between true and random coincidences.

The poor data collection rates in coincidence experiments can be improved by the so-called PIPECO method [17, 18], which uses photons of variable energy and detects electrons of zero kinetic energy (threshold photoelectrons) by scanning the wavelength of the light. As mentioned above, detection of zero eV electrons has the advantage of greater sensitivity (nearly 100 % of the electrons are accepted by the spectrometer), but the disadvantage that autoionization resonances may coincide in energy with Franck-Condon allowed transitions to an ionic state.

Figure 2.7 shows the result of a coincidence experiment in the case of ethylene. The breakdown diagram has been obtained in a PIPECO experiment [19]. It has been established that the threshold PES in the region between 11 and 20 eV was indeed almost entirely due to direct ionization (no autoionization).

Figure 2.7 shows that between the first ionization energy (10.5 eV) and 12.5 eV the parent cation is generated exclusively. Increasing the internal energy of $C_2H_4^+$ above 2 eV leads to a decrease of $C_2H_4^+$ in favor of $C_2H_2^+$. The incorporated unimolecular reactions with their thermodynamic limits are as follows

$$h\nu + C_2H_4 \rightarrow C_2H_2^+ + H_2 + e^- \qquad \Delta H_0 = 13.12 \text{ eV} \qquad 2.8$$

$$\rightarrow C_2H_3^+ + H + e^- \qquad \Delta H_0 = 13.22 \text{ eV} \qquad 2.9$$

$$\rightarrow C_2H_2^+ + H + H + e^- \qquad \Delta H_0 = 17.60 \text{ eV} \qquad 2.10$$

$$\rightarrow CH_2^+ + CH_2 + e^- \qquad \Delta H_0 = 17.90 \text{ eV} \qquad 2.11$$

The PES spectrum (not presented here) shows different ionic states of $C_2H_4^+$ accessible by Franck-Condon transitions with vertical ionization energies of 10.51, 12.85,

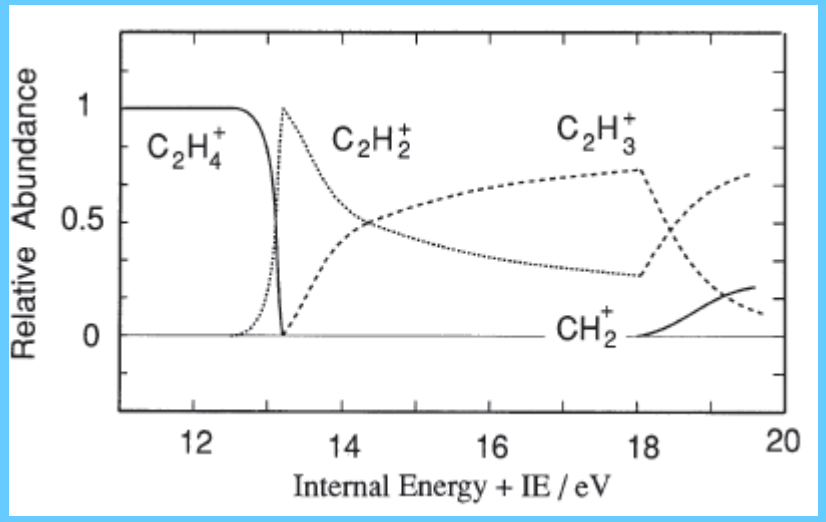

Fig. 2.7. Breakdown diagram for ethylene (adapted from [19]).

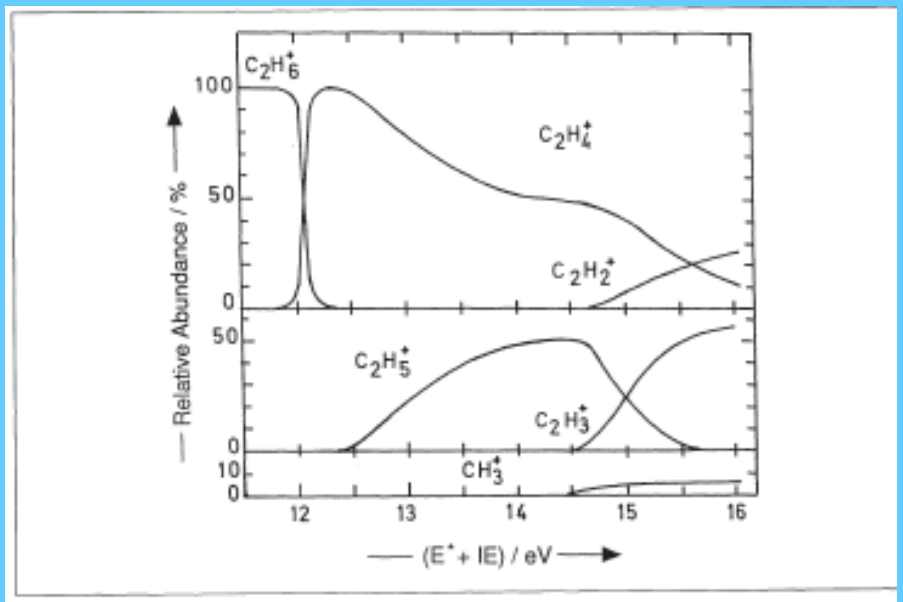

Fig. 1.20. Breakdown diagram for $C_2H_6^+$ from the ZKE coincidences with photoions, adapted from [43].

1.5 Charge Exchange Ionization

1.5.1 Introduction to Charge Exchange Physics and to Charge Exchange Mass Spectra

As was discussed above, the behavior of photons or of fast electron beams with respect to the target molecule results in ionization phenomena entirely dominated by Franck-Condon transitions. This has to be ascribed to the extremely small interaction time between the ionizing particle and the target molecule. As expected, many other ways to prepare electronically excited molecular ions are possible, such as the charge exchange (CE) processes used since 1954 [54, 55] for the study of mass spectra.

The CE ionization takes place when an ion A^+ of known translational energy is allowed to make short-range interactions with another atom or molecule. One distinguishes three main CE processes:

a) the symmetric CE, such as:
$A^+ + A \rightarrow A^+ + A$;
b) the asymmetric CE, such as:
$A^+ + B \rightarrow B^+ + A$;
c) the dissociative CE, such as:
$A^+ + BC \rightarrow B^+ + C + A$.

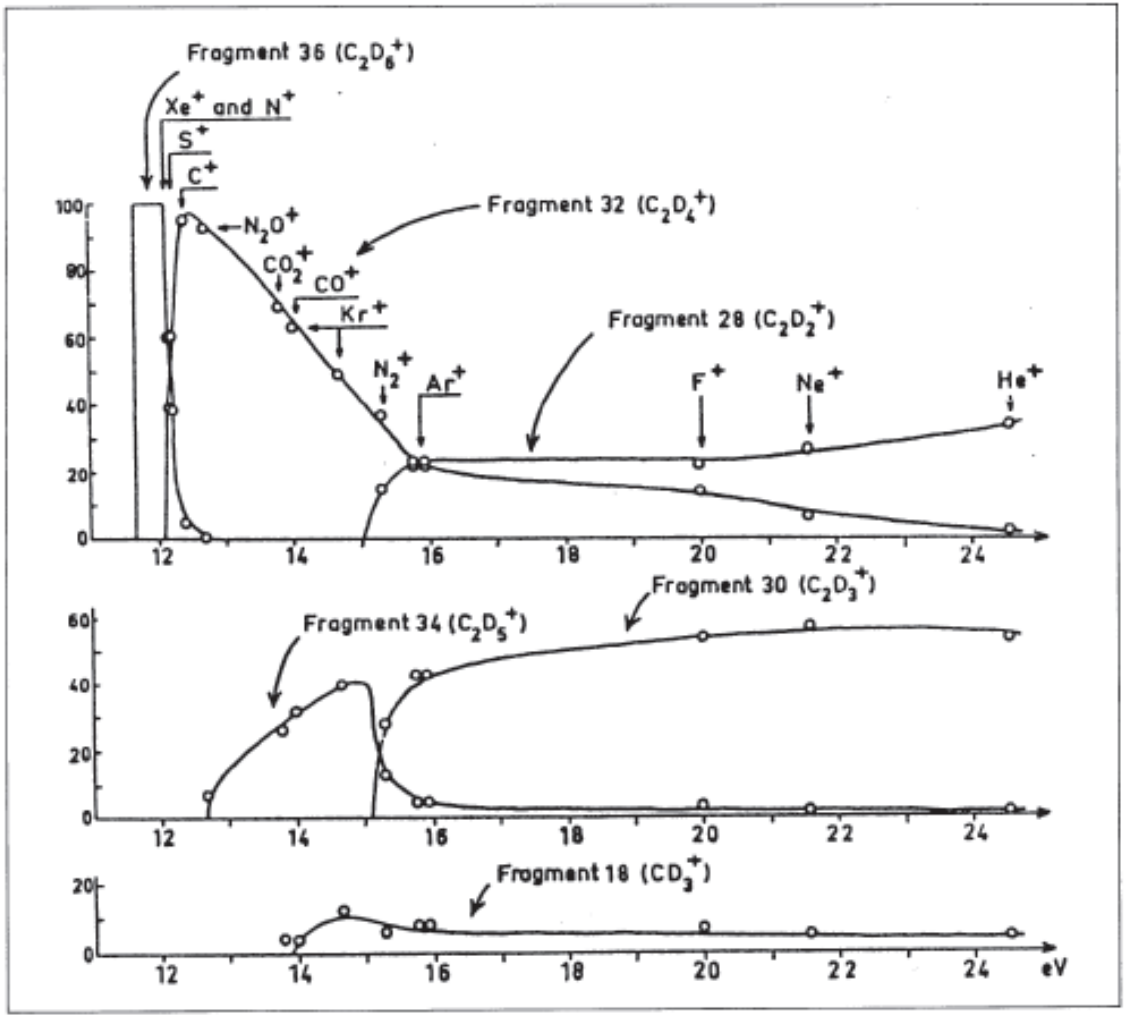

Fig. 1.25. Breakdown diagram of $C_2H_6^+$ from charge-exchange experiments [58].

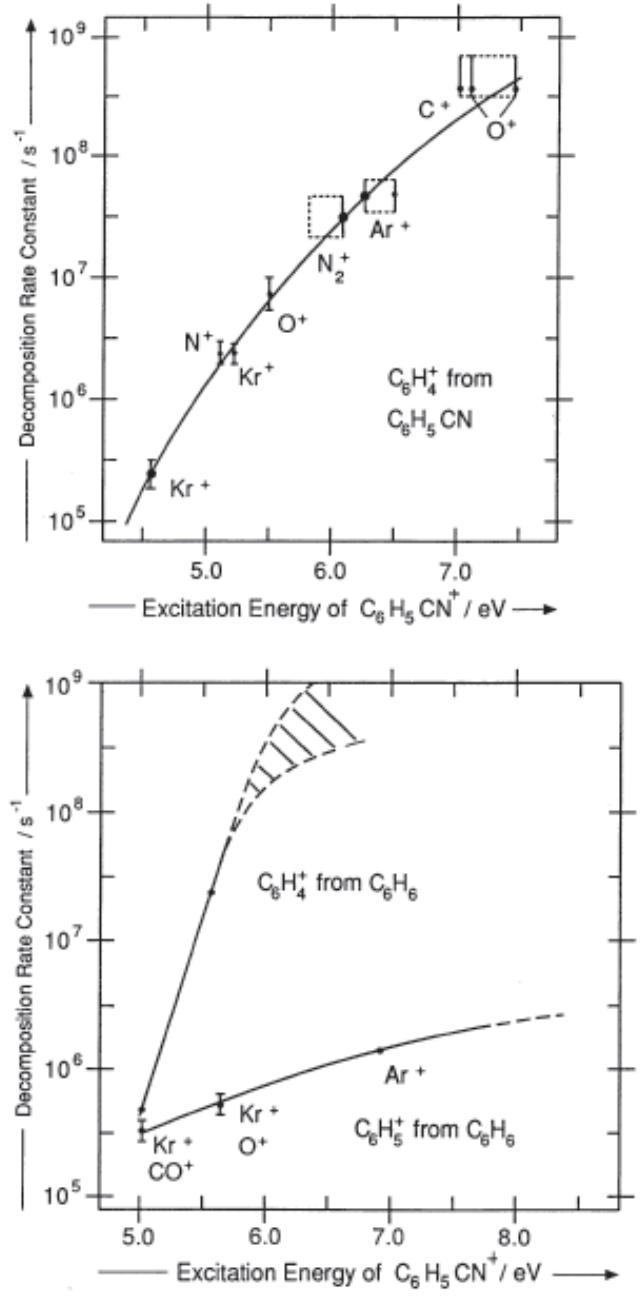

Fig. 1.26. $k(E)$ for $C_6H_5CN^+ \rightarrow C_6H_4^+ + HCN$, for $C_6H_6^+ \rightarrow C_6H_5^+ + H$ and $C_6H_6^+ \rightarrow C_4H_4^+ + C_2H_2$, as obtained from CE experiments with the special technique of Ottinger (see text) [60].

Penning ionization

$X^* + AB \rightarrow X^+ + AB^+ + e^-$

Should yield very similar electron energy distribution

$E_e = E(X^*) - [IP(AB) + E_{J,K}(AB^+)] + \Delta E$

ΔE - resultant energy shifts due to the interaction between the reactants and the interaction between the products during the collisional energy transfer process

Energy levels for rare-gas atoms and photons[a]

Atom	Electron configuration	Metastables		Resonance photons		
		designation	energy (eV)	transition	wavelength (nm)	energy (eV)
Helium	1s2p			$2^1P \rightarrow 1^1S$	58.44	21.217
				$2^1P \rightarrow 2^1S$	2058.7	0.602
				$2^3P \rightarrow 2^3S$	1083.0	1.145
	1s2s	2^1S	20.616			
		2^3S	19.818			
Neon	$2p^5 3s$	$^3P_0$	16.716	$^1P_1 \rightarrow {}^1S_0$	73.59	16.848
		$^3P_2$	16.619	$^3P_1 \rightarrow {}^1S_0$	74.37	16.671
Argon	$3p^5 4s$	$^3P_0$	11.723	$^1P_1 \rightarrow {}^1S_0$	104.82	11.823
		$^3P_2$	11.548	$^3P_1 \rightarrow {}^1S_0$	106.67	11.623
Krypton	$4p^5 5s$	$^3P_0$	10.562	$^1P_1 \rightarrow {}^1S_0$	116.49	10.643
		$^3P_2$	9.915	$^3P_1 \rightarrow {}^1S_0$	123.58	10.032
Xenon	$5p^5 6s$	$^3P_0$	9.447	$^1P_1 \rightarrow {}^1S_0$	131.24	9.447
		$^3P_2$	8.315	$^3P_1 \rightarrow {}^1S_0$	146.96	8.436

Tables

Energy levels for rare-gas atoms and photons[a]

Atom	Electron configuration	Metastables: designation	Metastables: energy (eV)	Resonance photons: transition	Resonance photons: wavelength (nm)	Resonance photons: energy (eV)
Helium	1s2p			$2^1P \rightarrow 1^1S$	58.44	21.217
				$2^1P \rightarrow 2^1S$	2058.7	0.602
				$2^3P \rightarrow 2^3S$	1083.0	1.145
	1s2s	2^1S	20.616			
		2^3S	19.818			
Neon	$2p^5 3s$	$^3P_0$	16.716			
		$^3P_2$	16.619			
Argon	$3p^5 4s$	$^3P_0$	11.723			
		$^3P_2$	11.548			
Krypton	$4p^5 5s$	$^3P_0$	10.562			
		$^3P_2$	9.915			
Xenon	$5p^5 6s$	$^3P_0$	9.447			
		$^3P_2$	8.315			

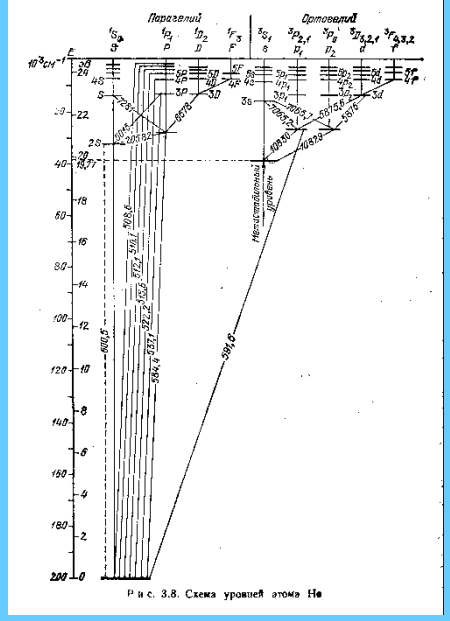

Radiative lifetimes of metastable rare-gas atoms

Atom	State designation	Radiative lifetime (s): theoretical	ref.	experimental
Helium	2^1S	1.95×10^{-2}	*a*	1.97×10^{-2}
	2^3S	7.9×10^{3}	*c*	9.0×10^{3}
Neon	$^3P_0$	4.30×10^{2}	*e*	
	$^3P_2$	2.44×10^{1}	*e*	>0.8
Argon	$^3P_0$	4.49×10^{1}	*e*	
	$^3P_2$	5.59×10^{1}	*e*	>1.3
Krypton	$^3P_0$	4.9×10^{-1}	*e*	
	$^3P_2$	8.51×10^{1}	*e*	>1.0
Xenon	$^3P_0$	7.8×10^{-2}	*e*	
	$^3P_2$	14.95×10^{1}	*e*	

PIES – DATA atomic reactant

EEDC produced by HeI radiation and by $He^*(2^1S)$ and $He^*(2^3S)$ metastables with Ar.
Nominal position of the peaks is indicated by arrows.
Obtained ΔE= +35meV for both metastables.

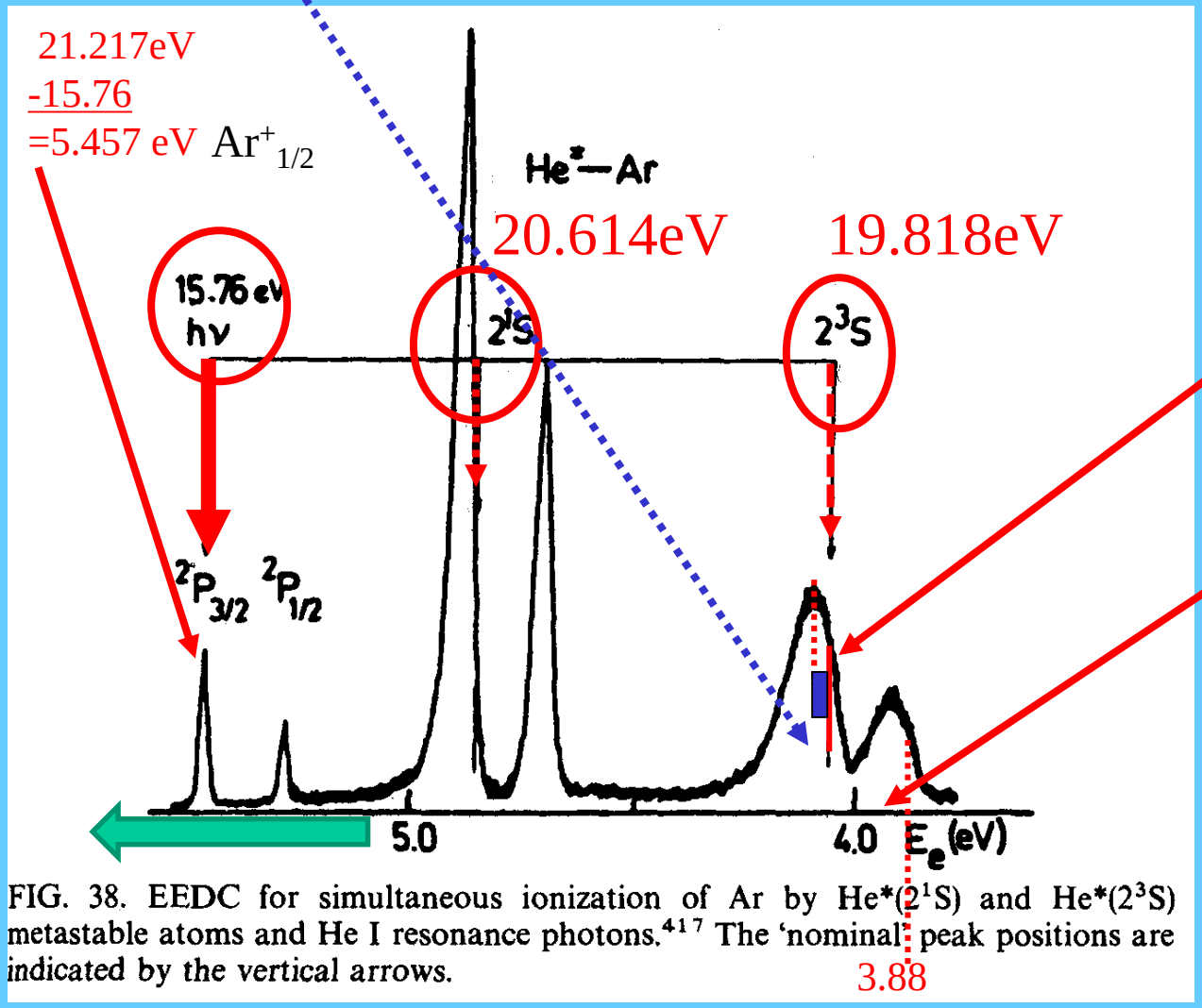

FIG. 38. EEDC for simultaneous ionization of Ar by $He^*(2^1S)$ and $He^*(2^3S)$ metastable atoms and He I resonance photons.[417] The 'nominal' peak positions are indicated by the vertical arrows.

19.818eV $Ar^+_{3/2}$
-15.76
=4.058 eV

19.818eV $Ar^+_{1/2}$
-15.93
=3.88 eV

PIES – DATA atomic reactant

EEDC produced by HeI radiation and by He*(2¹S) and H
Nominal position of the peaks is indicated by arrows.
Obtained ΔE= +35meV for both metastables.

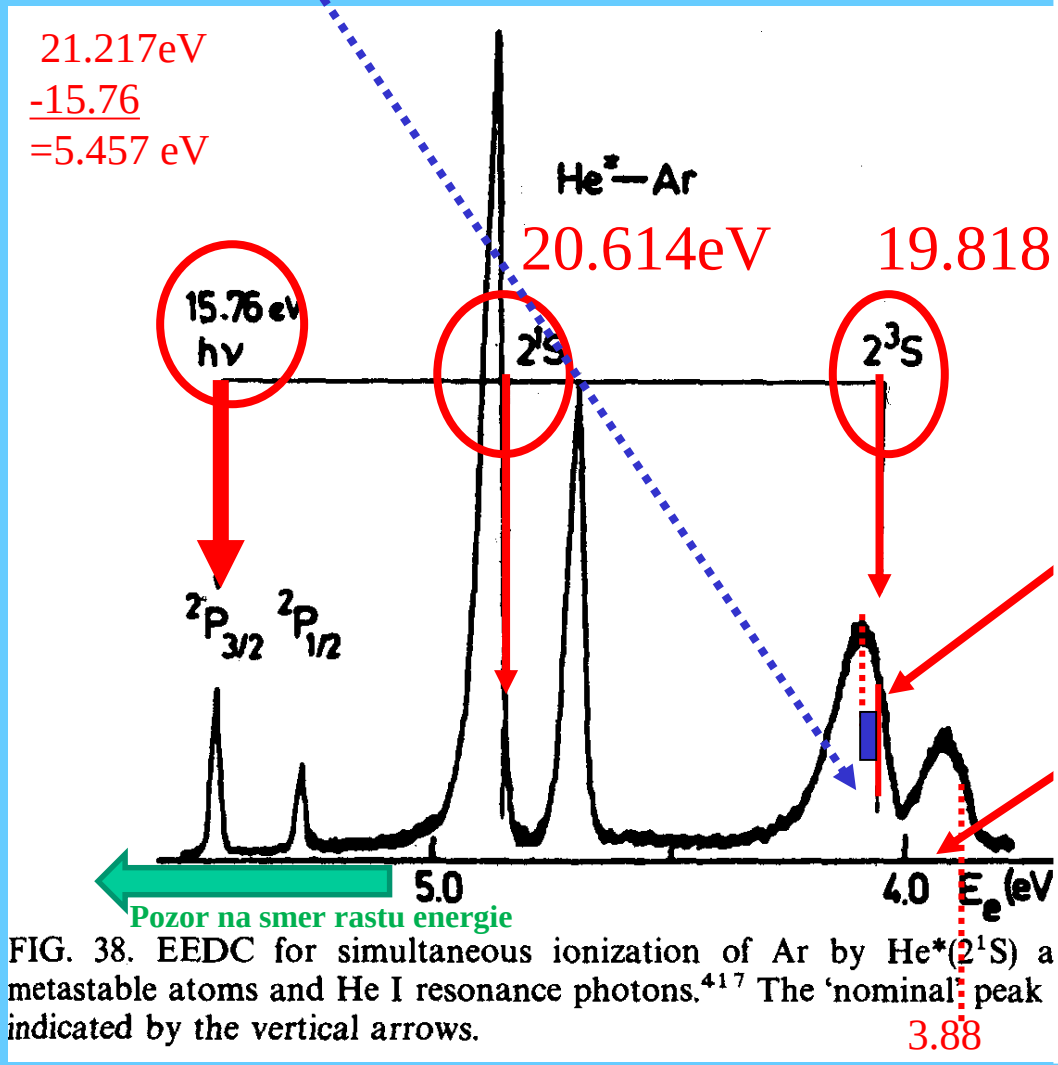

FIG. 38. EEDC for simultaneous ionization of Ar by He*(2¹S) a metastable atoms and He I resonance photons.[417] The 'nominal' peak indicated by the vertical arrows.

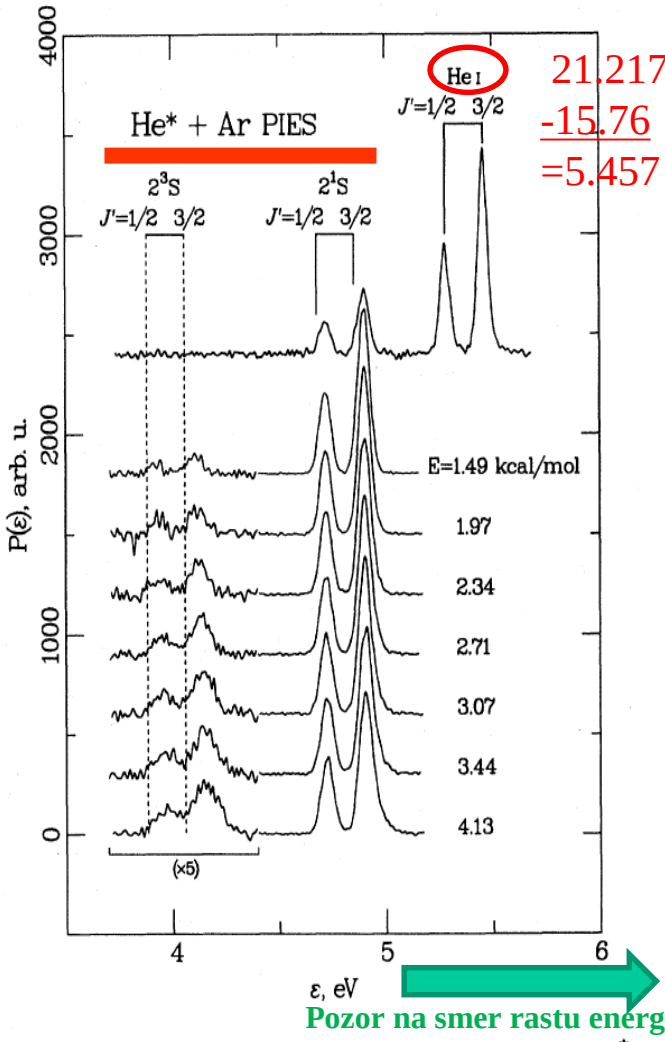

FIG. 19. Energy dependence of electron spectra from He* + Ar PI (Bevsek *et al.*, 1992). The uppermost spectrum is a simultaneous PI electron/photoelectron measurement used for calibration of the energy scale; the J' values refer to the final Ar^+ fine-structure state. The remaining PI electron spectra are normalized to the same area under the $J'=\frac{3}{2}$ peak; base lines are shifted for clarity of viewing. The variations in intensity and line position with energy for ^3S are noteworthy; the fine structure in these data is noise, due to a low counting rate.

PIES Molecules

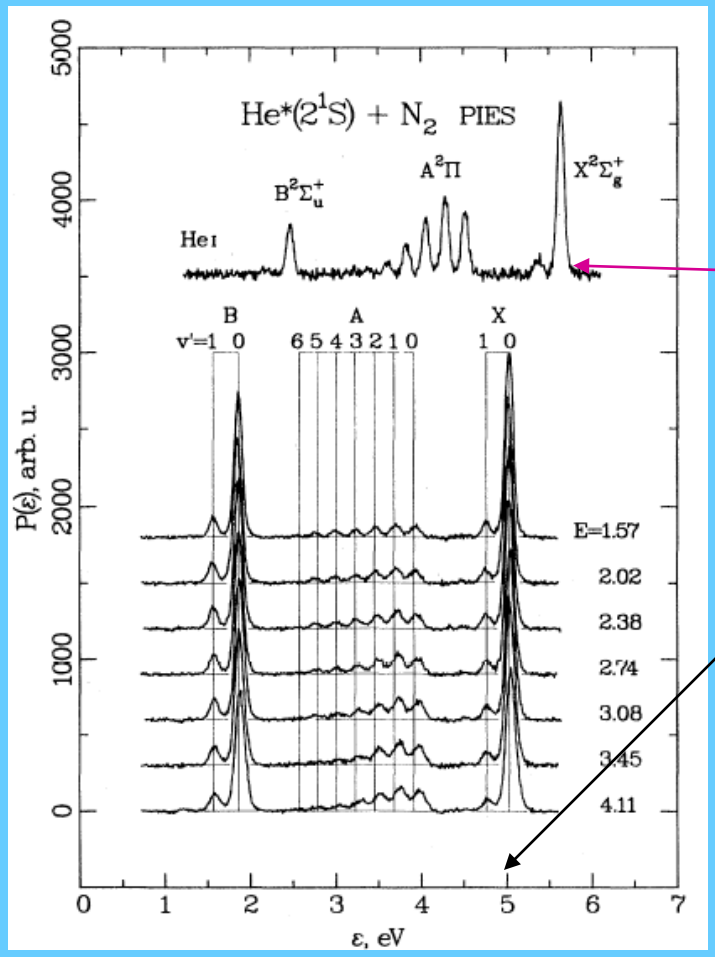

FIG. 21. Energy dependence of electron spectra from state-selected $He^*(2\,^1S)+N_2$, from Dunlavy *et al.* (1990, 1992). The uppermost spectrum is a photoelectron spectrum for reference, with N_2^+ electronic state assignments indicated. Noteworthy PIES features include the population change in *A* and *B* states relative to *X* compared to photoelectron spectroscopy and vibronic peak intensity and position changes with *E* (kcal/mol) of the *A* state.

21.217 eV

20.616 eV

~5eV

15.6eV

N_2

D

19.818 eV

14.5eV

N

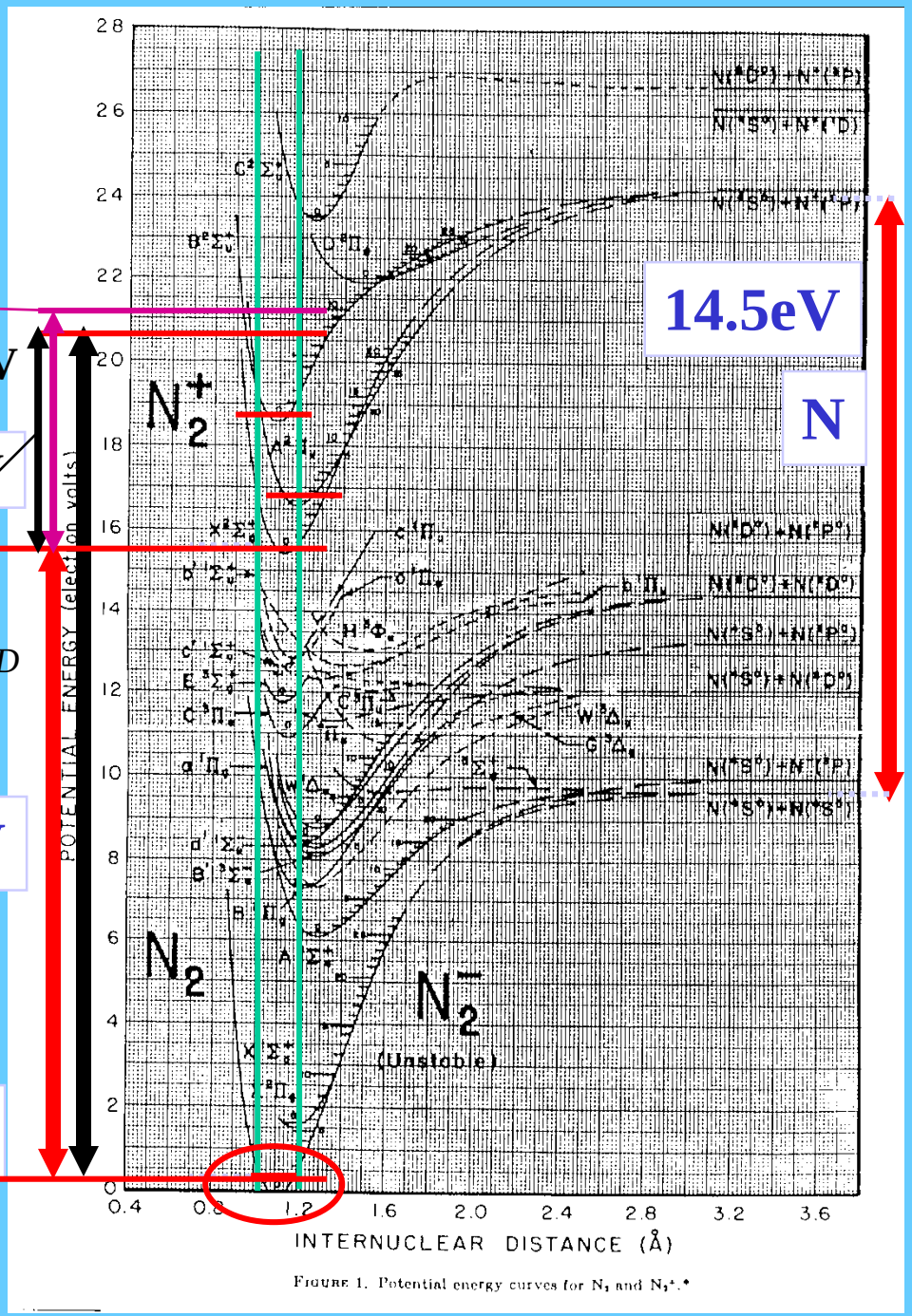

FIGURE 1. Potential energy curves for N_2 and N_2^+.*

PIES – DATA atomic reactant

EEDC produced by HeI radiation and by $He^*(2^1S)$ and $He^*(2^3S)$ metastables with Ar.
Nominal position of the peaks is indicated by arrows.
Obtained ΔE= +35meV for both metastables.

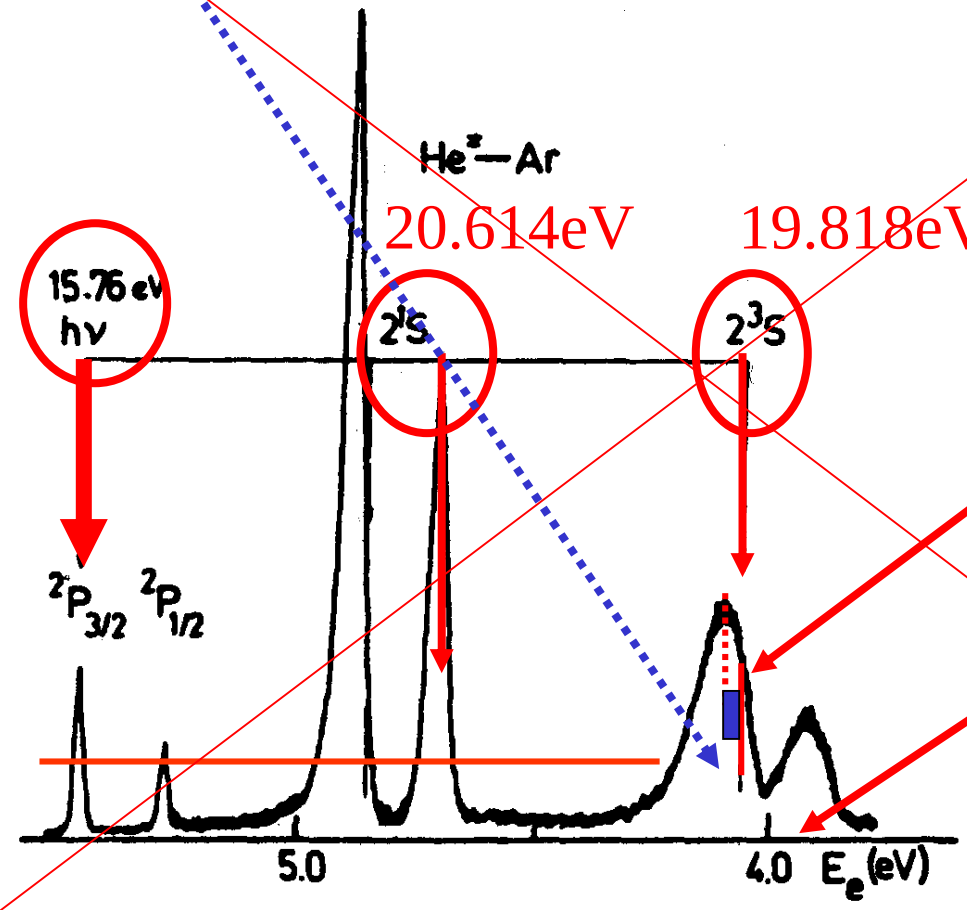

FIG. 38. EEDC for simultaneous ionization of Ar by He*(2^1S) and He*(2^3S) metastable atoms and He I resonance photons.[417] The 'nominal' peak positions are indicated by the vertical arrows.

3.88

19.818eV $Ar^+_{1/2}$
-15.76
=4.058 eV

19.818eV $Ar^+_{3/2}$
-15.93
=3.88 eV

PIE nt

EEL e*(2¹S) and H

Non by arrows.

Obt s.

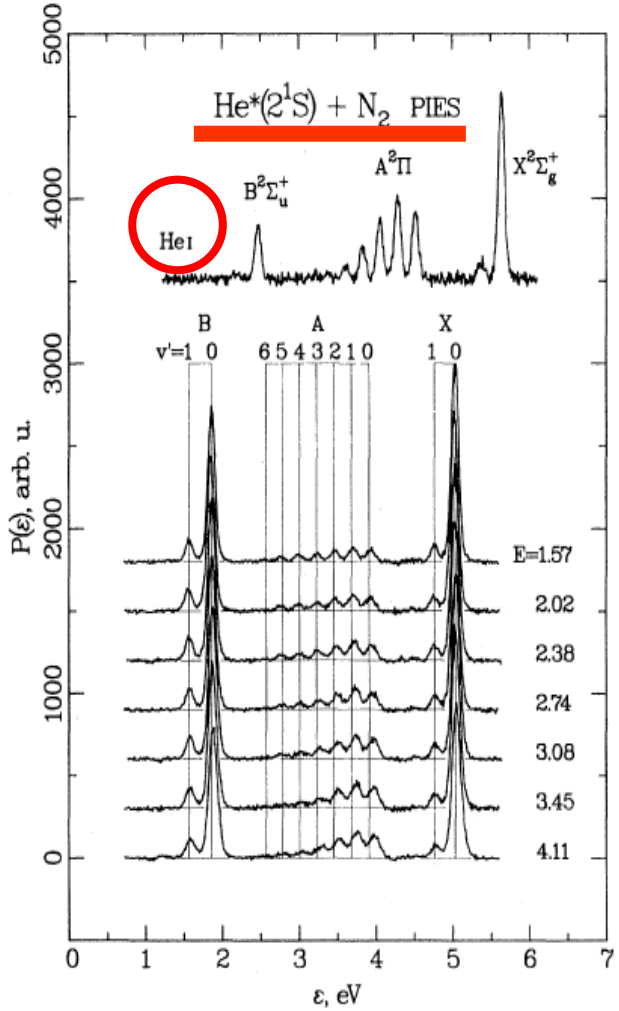

FIG. 21. Energy dependence of electron spectra from state-selected $He^*(2\,^1S)+N_2$, from Dunlavy *et al.* (1990, 1992). The uppermost spectrum is a photoelectron spectrum for reference, with N_2^+ electronic state assignments indicated. Noteworthy PIES features include the population change in *A* and *B* states relative to *X* compared to photoelectron spectroscopy and vibronic peak intensity and position changes with *E* (kcal/mol) of the *A* state.

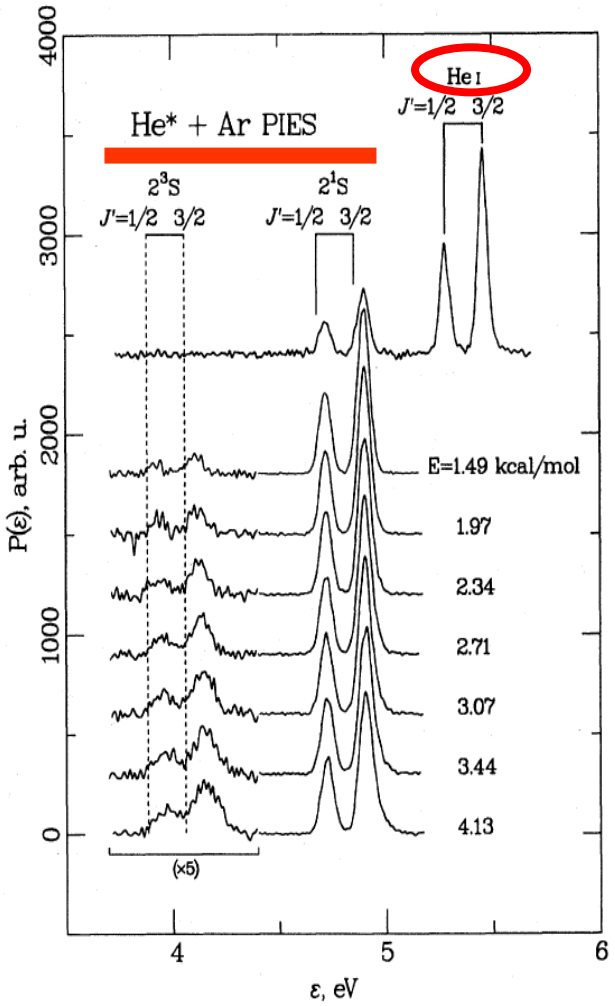

FIG. 19. Energy dependence of electron spectra from He^*+Ar PI (Bevsek *et al.*, 1992). The uppermost spectrum is a simultaneous PI electron/photoelectron measurement used for calibration of the energy scale; the J' values refer to the final Ar^+ fine-structure state. The remaining PI electron spectra are normalized to the same area under the $J'=\frac{3}{2}$ peak; base lines are shifted for clarity of viewing. The variations in intensity and line position with energy for ^3S are noteworthy; the fine structure in these data is noise, due to a low counting rate.

PIES – DATA molecular reactant

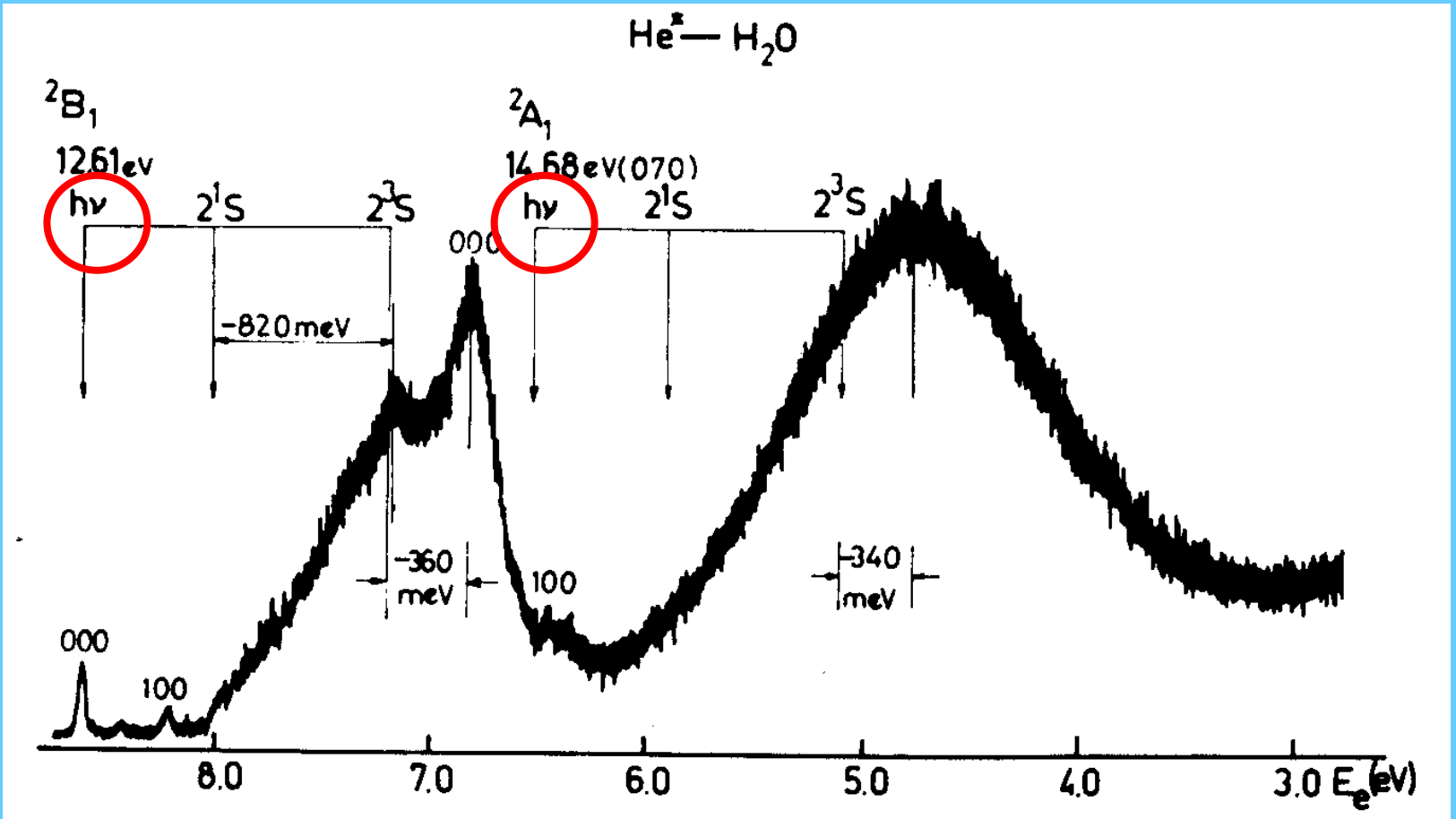

FIG. 39. EEDC for simultaneous ionization of H_2O by He*(2^1S) and He*(2^3S) metastable atoms and He I resonance photons.[421] The 'nominal' peak positions are indicated by the vertical arrows.

$He^*(^3S) + H_2O \rightarrow$	$He + H_2O^+ + e^-$	77.9%
	$He + OH^+ + H + e^-$	17.9%
	$He + OH + H^+ + e^-$	3.2%
	$HeH^+ + OH + e^-$	0.8%
	$HeO^+ + H_2 + e^-$	0.2%

$Ne^*(^3P) + H_2O \rightarrow Ne + H_2O^+ + e^-$

PIES experimental technique

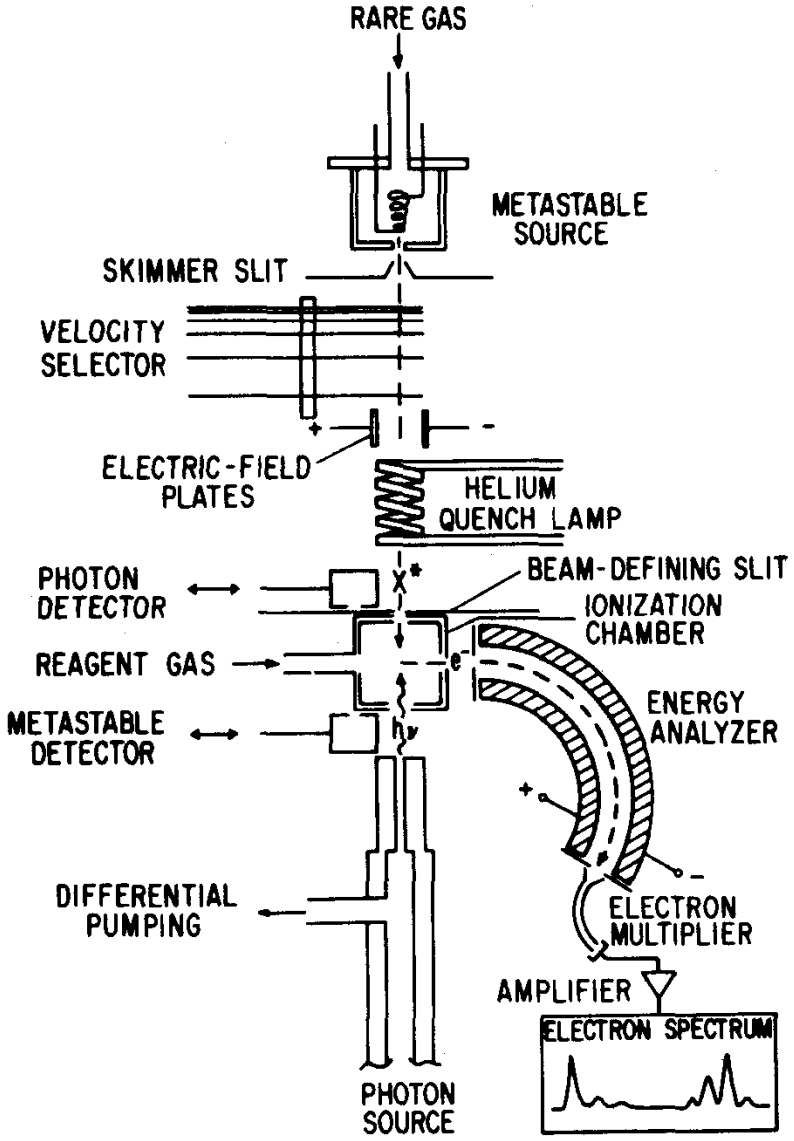

FIG. 41. Schematic diagram of a typical Penning-electron/photoelectron spectrometer system.

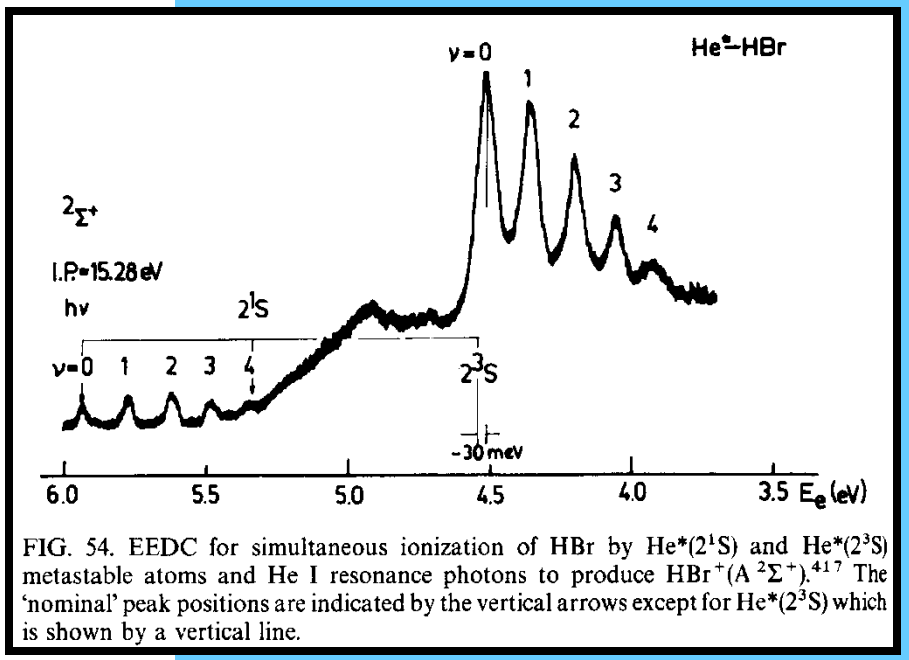

FIG. 54. EEDC for simultaneous ionization of HBr by He*(2^1S) and He*(2^3S) metastable atoms and He I resonance photons to produce $HBr^+(A\ ^2\Sigma^+)$.[417] The 'nominal' peak positions are indicated by the vertical arrows except for He*(2^3S) which is shown by a vertical line.

Experiment

$$Ng^* + BC \rightarrow X + Y^+ + e^-$$

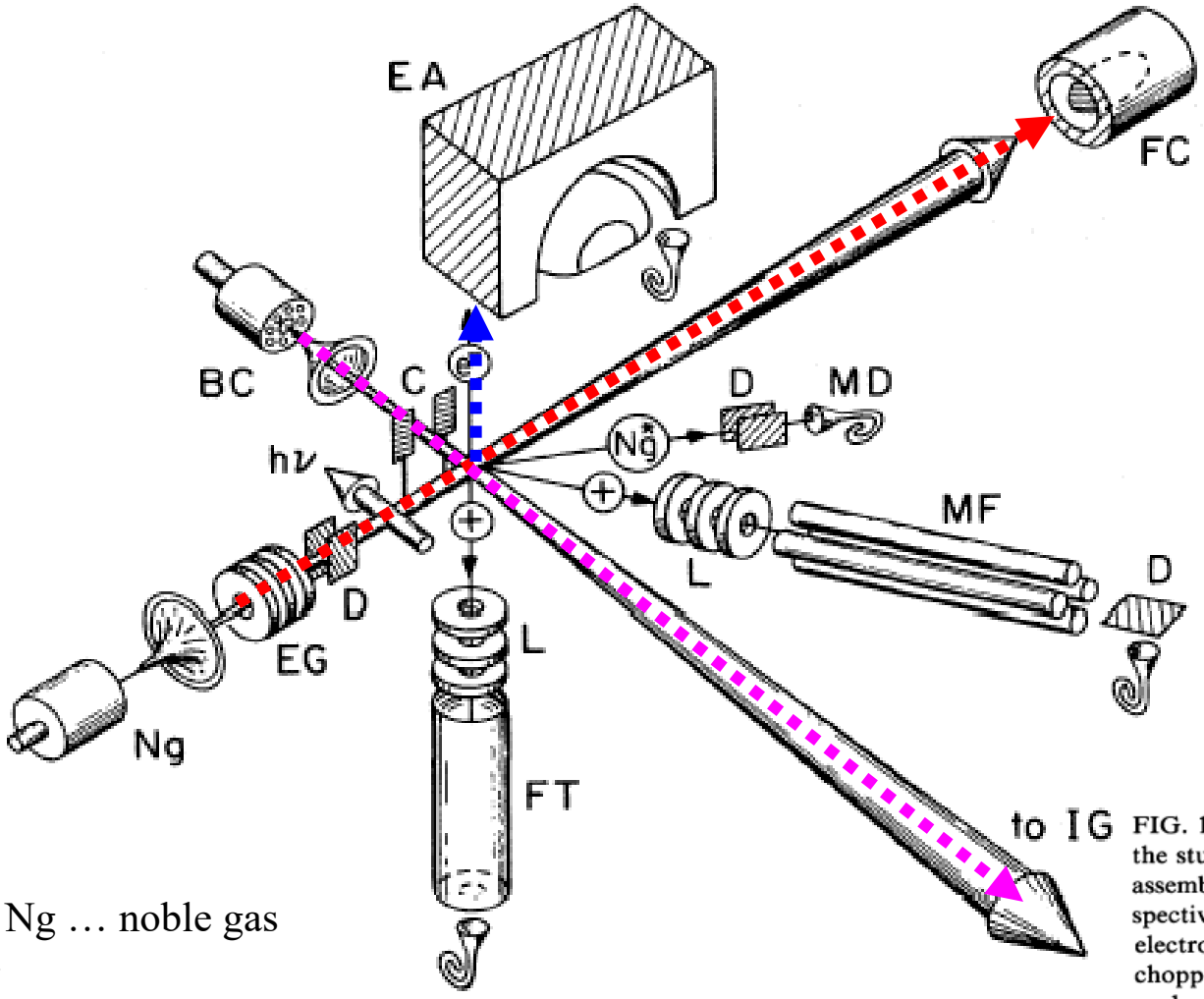

Ng … noble gas

FIG. 1. Schematic illustration of a crossed-beam apparatus for the study of Penning ionization. Ng and BC—nozzle-skimmer assemblies for the excited atom and partner molecule beams, respectively; EG—electron gun used to excite Ng to Ng*; D—electrostatic deflector; $h\nu$—photons for state selection; C—chopper for modulation of BC beam; EA—electrostatic energy analyzer for Penning electrons; FC—Faraday cup metastable beam monitor; MD—metastable detector (electron multipler); L—electrostatic lens/retarding field assembly; MF—quadrupole mass filter; IG or MS—molecular-beam monitor, either ion gauge or mass spectrometer; FT—ion flight tube for coincidence measurements. The curly objects are channel electron multipliers. Not indicated are various collimators and plates surrounding the intersection region for total ion collection experiments.

Dynamics of the process

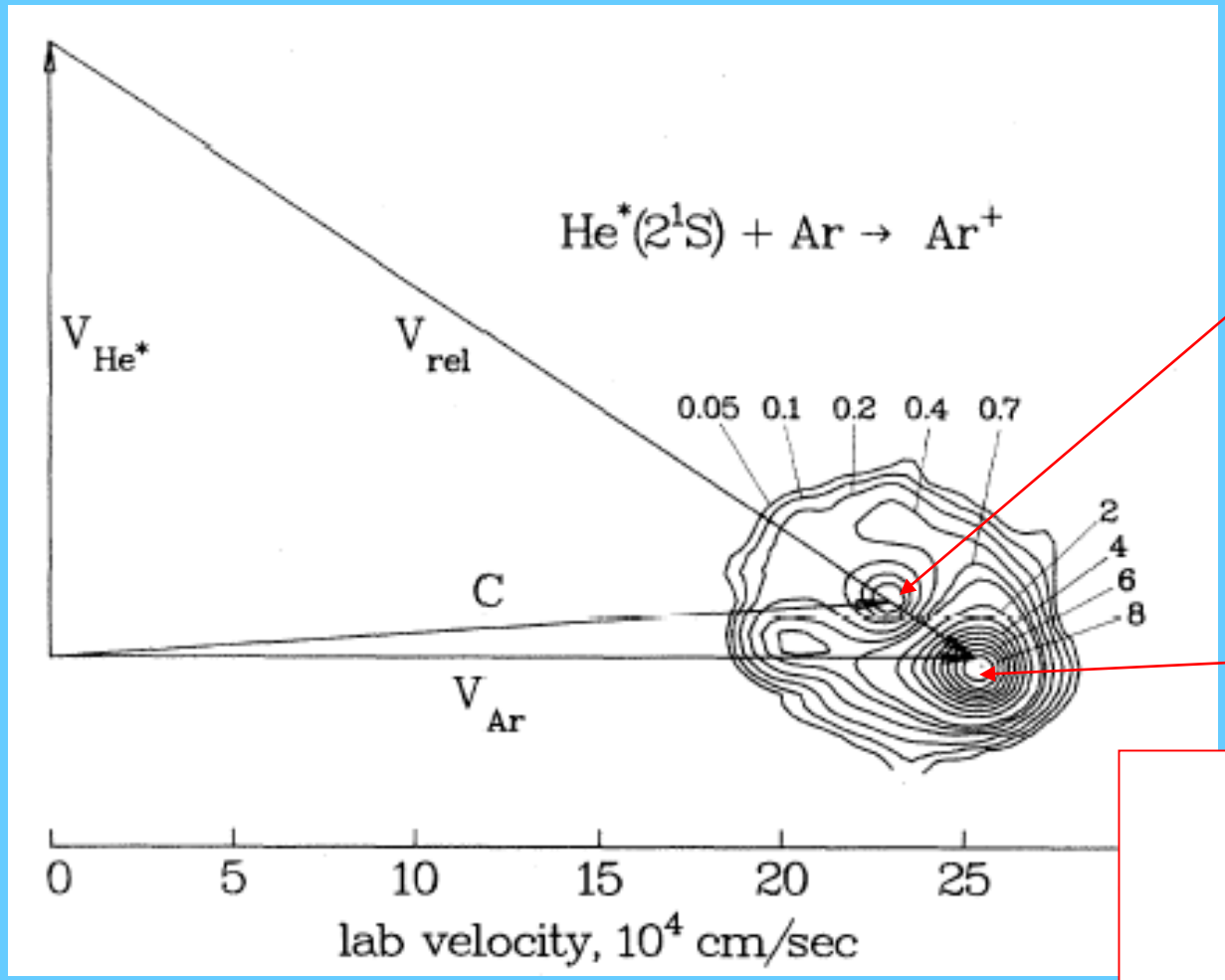

FIG. 20. Velocity-space c.m. Ar^+ intensity contour map for $He^*(2\,^1S)+Ar$ at $E=4.2$ kcal/mol (Longley *et al.*, 1992). The map is arbitrarily normalized to 10 at the peak. Strong forward scattering is indicated, with $E' \approx E$ and moderate coupling between E' and θ.

Indirect process

Direct process

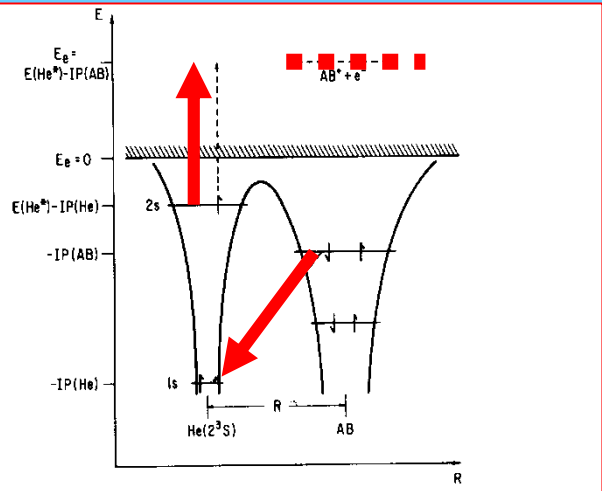

FIG. 3. Schematic representation of electron orbitals demonstrating the two-electron exchange mechanism for the Penning process $He(2^3S)+AB \rightarrow He(1^1S)+AB^+ + e^-$.

Potential energy curves, interpretation

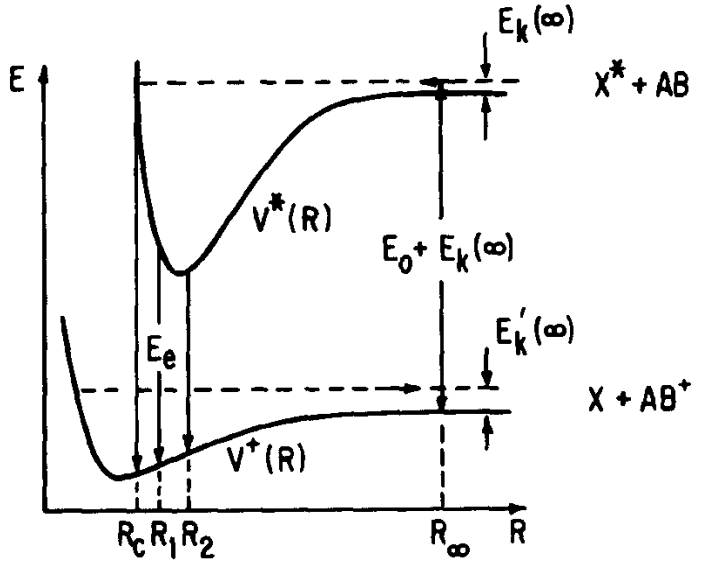

FIG. 46. Potential-energy curve model for PI and AI processes.

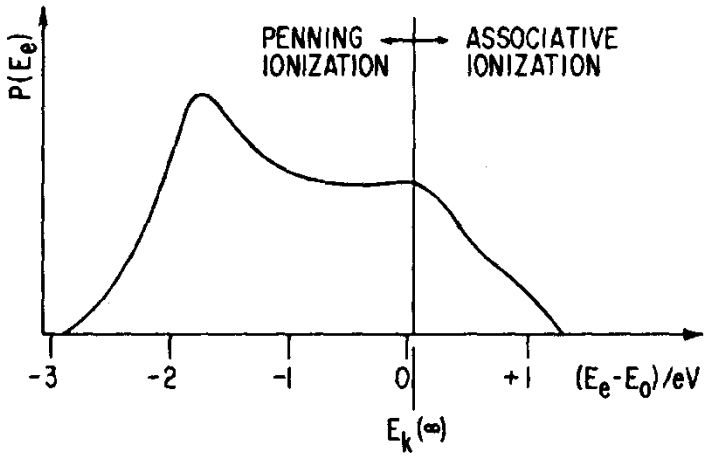

FIG. 47. A hypothetical EEDC representing the probability of producing an electron, $P(E_e)$, of energy $(E_e - E_0)$ in the ionizing system described in Fig. 46. Shown are the portions of the EEDC related to PI and AI.

PI electron – ion coincidence spectroscopy PIEICO

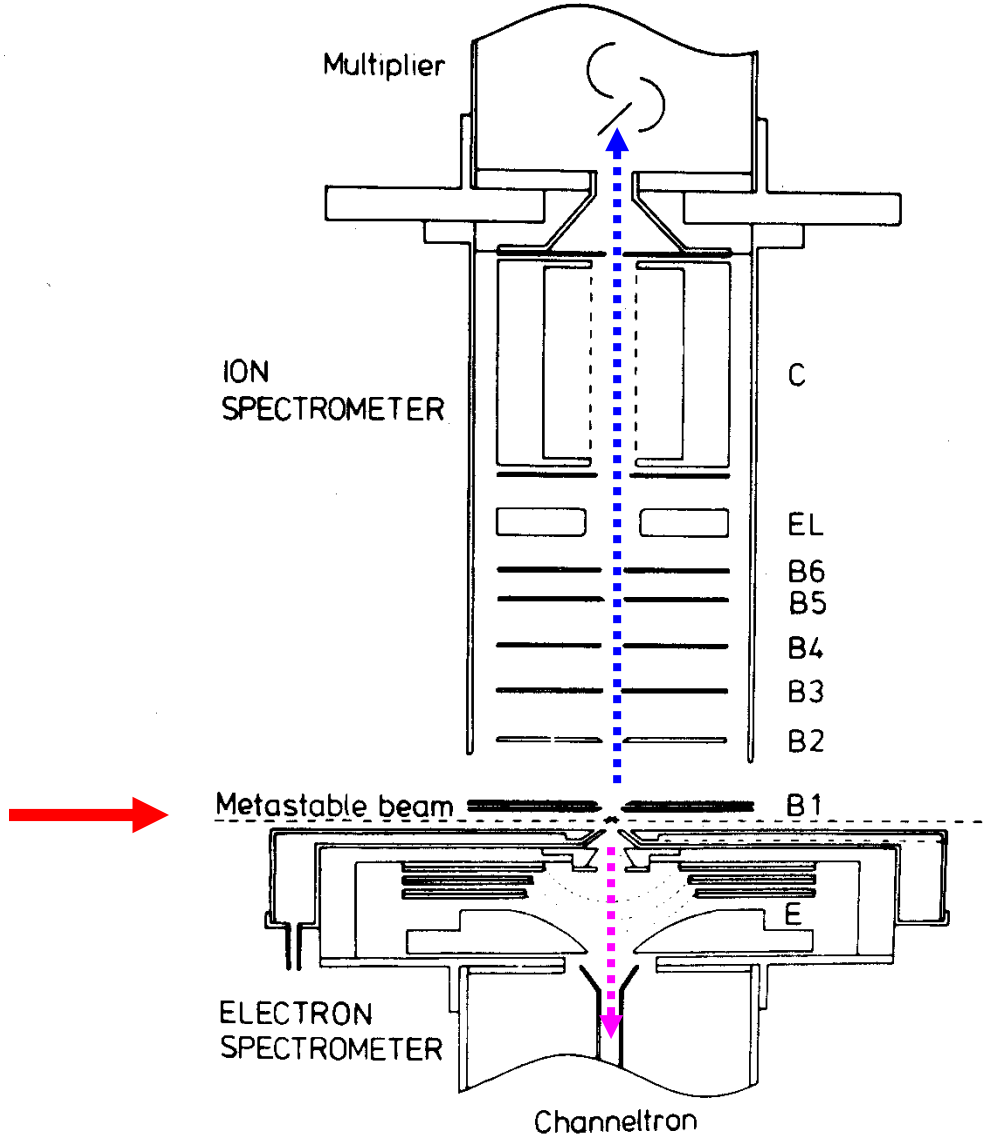

FIG. 57. Schematic diagram of a retarding field electron energy analyzer and time-of-flight ion mass spectrometer for conducting PIEICOS studies.[471]

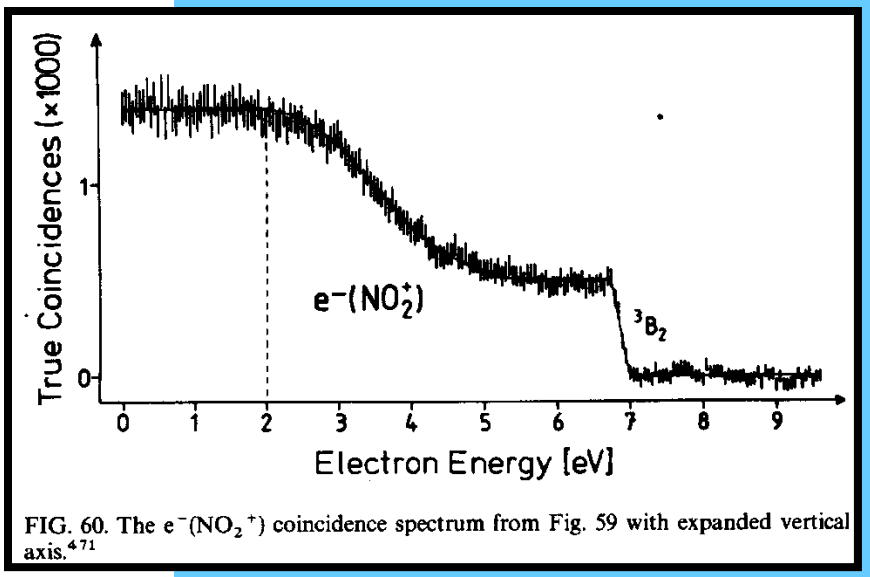

FIG. 60. The $e^-(NO_2^+)$ coincidence spectrum from Fig. 59 with expanded vertical axis.[471]

Data PIEICO

hν

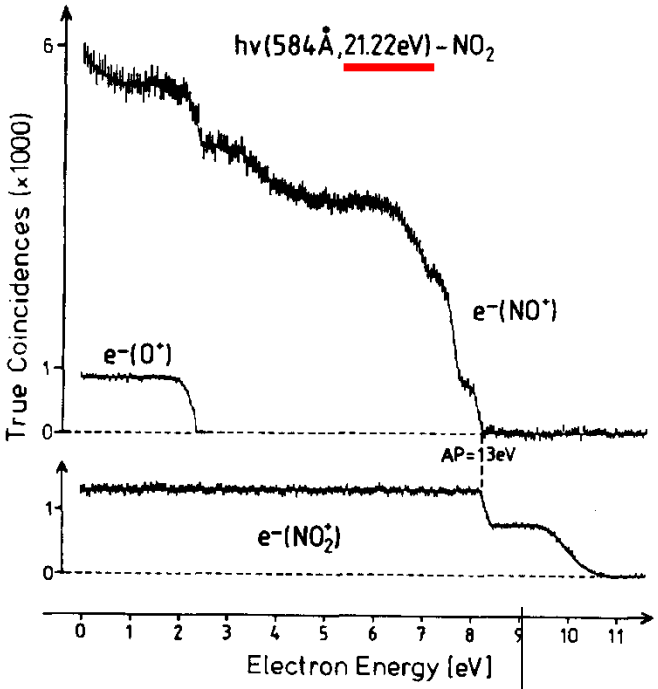

FIG. 58. Electron–ion coincidence spectra produced by He I PhI of NO_2 employing the apparatus shown in Fig. 57.[471]

He*

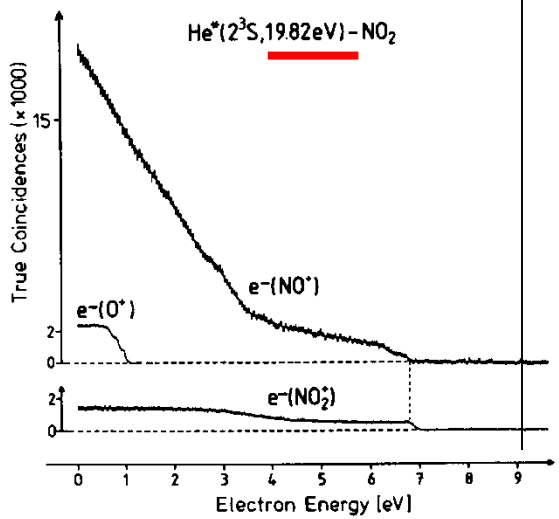

FIG. 59. Electron–ion coincidence spectra produced by $He^*(2^3S)$ PI of NO_2 employing the apparatus shown in Fig. 57.[471]

Data PIEICO

hν

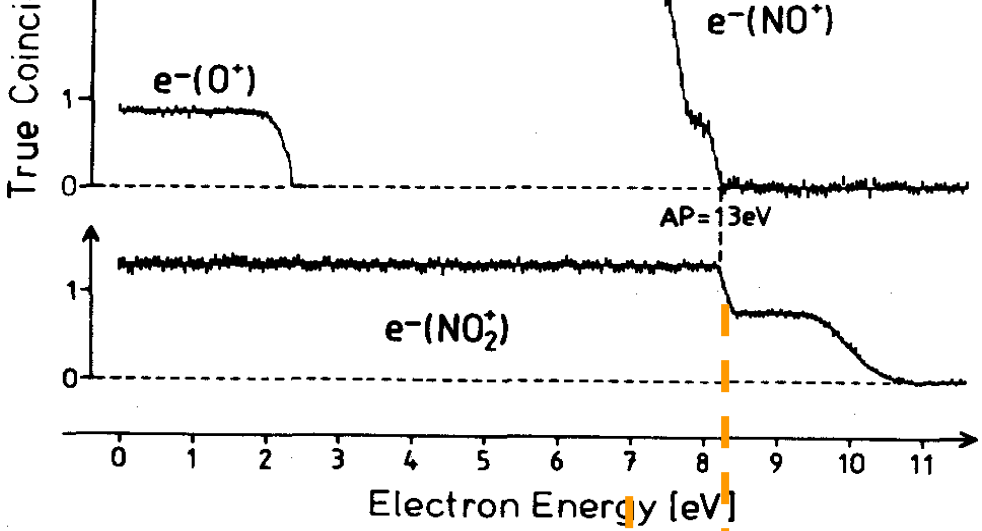

FIG. 58. Electron–ion coincidence spectra produced by He I PhI of NO_2 employing the apparatus shown in Fig. 57.[471]

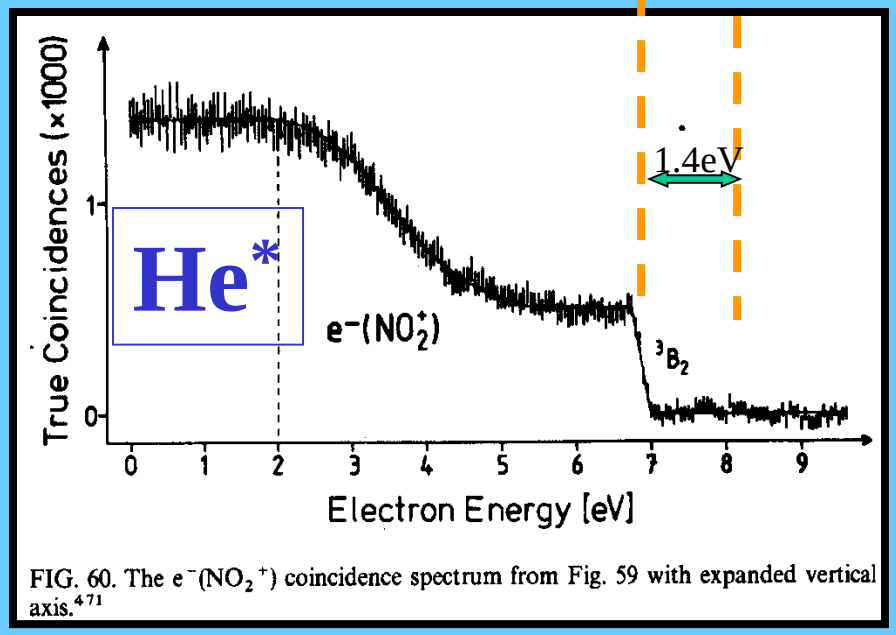

FIG. 60. The $e^-(NO_2^+)$ coincidence spectrum from Fig. 59 with expanded vertical axis.[471]

Pohádka r. 1999

JOURNAL OF CHEMICAL PHYSICS VOLUME 111, NUMBER 16 22 OCTOBER 1999

The chemi-ionization of $He^*(2\,^{1,3}S)+Ar,Kr,Xe$ for collision energies from 0.003 to 6 eV

R. Feltgen, H. Ferkel,[a] R. K. B. Helbing,[b] A. Lindinger, D. Pikorz, and H. Vehmeyer
Max-Planck-Institut für Strömungsforschung, Bunsenstr.10, D-37073 Göttingen, Germany

Measurements of the collision energy dependence of the chemi-ionization cross sections of the model systems $He^*(2\,^{1,3}S)+R$, R=Ar,Kr,Xe, are presented for the relevant energy range 0.003–6 eV. Except for $He^*(2\,^{1}S)+Xe$, all systems show a pronounced minimum of ionization at thermal energies. In the hyperthermal range, however, the two spin systems are in sharp contrast to each other: the triplet systems exhibit a broad saturating maximum of ionization, whereas the singlet systems reveal a shallow shaped second minimum (pronounced for Xe) which can be rationalized within the one-electron model potential calculations of Siska [J. Chem. Phys. **71**, 3942 (1979)]. Using an effective single-channel Schrödinger equation, one finds, for all systems, complex potentials depending on distance only which properly model the measured features. A more profound picture appears when differential elastic cross sections from experiments of other groups are included. In the triplet case, differential elastic and chemi-ionization data can be adequately described with one complex potential, i.e., the local approximation holds. This is not found for the singlet systems. The hyperthermal minima instead give evidence that the optical singlet potentials are nonlocal. Various aspects of this striking spin dependence of the characteristics of $He^*(2\,^{1,3}S)+R$ are discussed. In particular, the breakdown of the local approximation in the singlet case can be rigorously derived. [S0021-9606(99)00440-7]

Pohadka - experiment

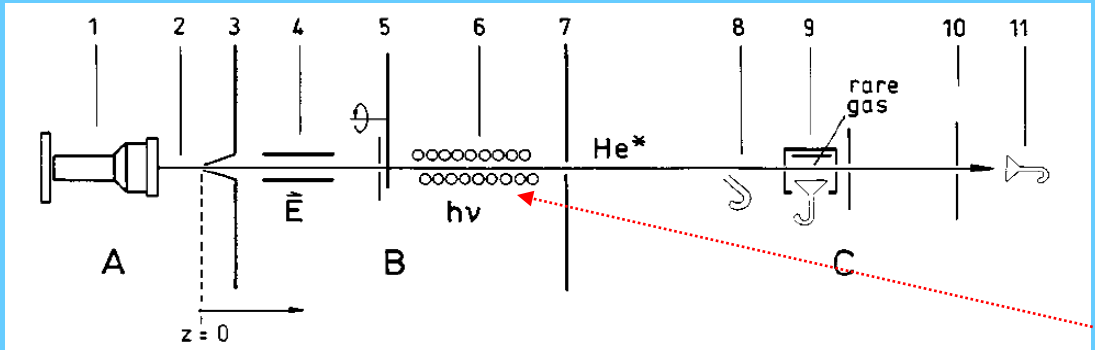

FIG. 1. Schematic view of the experimental arrangement consisting of three differentially pumped stages *A*, *B*, and *C*, where the primary beam He*($2\,^{1,3}S$) is produced, prepared, and used for the measurements, respectively. (1) nozzle source heated by a high-pressure He arc, nozzle aperture ~ 1 mm Ø, $-60 < z < -10$ mm; (2) low-pressure He arc; (3) skimmer 0.4 mm Ø, $z = 0$ mm; (4) condenser 2 kV/cm; (5) TOF chopper, $z = 430$ mm; (6) quench lamp; (7) collimator 6 mm Ø, $z = 935$ mm; (8) first beam monitor channeltron (off axis), $z = 1597$ mm; (9) collision cell with ion channeltron and repeller electrode, $\bar{z} = 1640$ mm; (10) collimator 0.3 mm Ø, $z = 2130$ mm; (11) second beam monitor channeltron, $z = 2153$ mm.

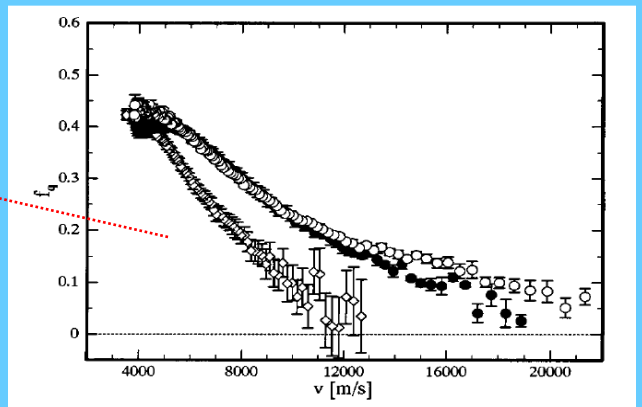

FIG. 2. Quenching efficiency f_q [Eq. (3)] for the singlet component in the He* beam as a function of the He* velocity v for three different quench lamps (◇, ●, ○) explained in the text.

Results, ….

1999

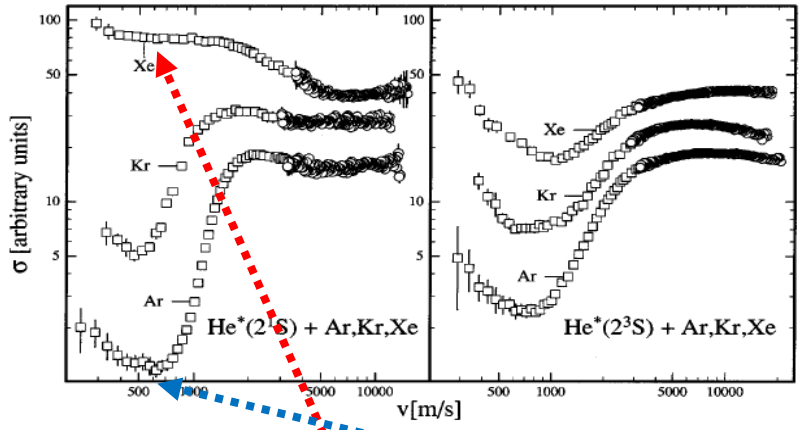

FIG. 3. Measured CI cross sections σ for $He^*(2\,^{1,3}S)+Ar,Kr,Xe$ as a function of the He^* velocity v. (□) thermal, (○) hyperthermal.

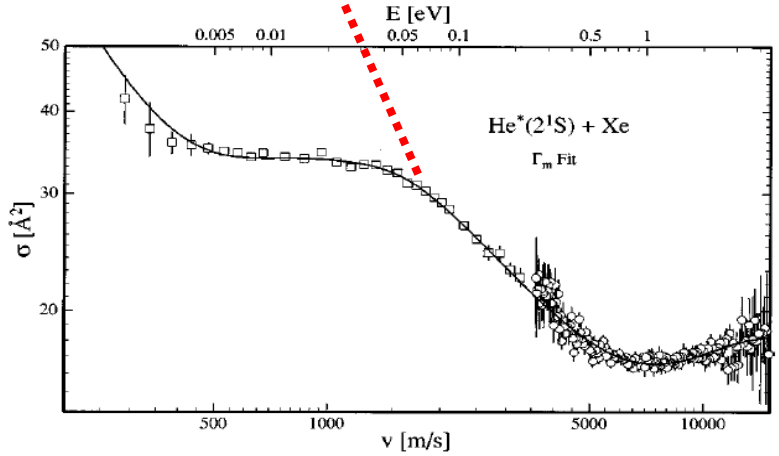

FIG. 7. $(V_{MGJS}-i\Gamma_m/2)$ fit (———) of CI data for $He^*(2\,^1S)+Xe$ (□,○).

1976

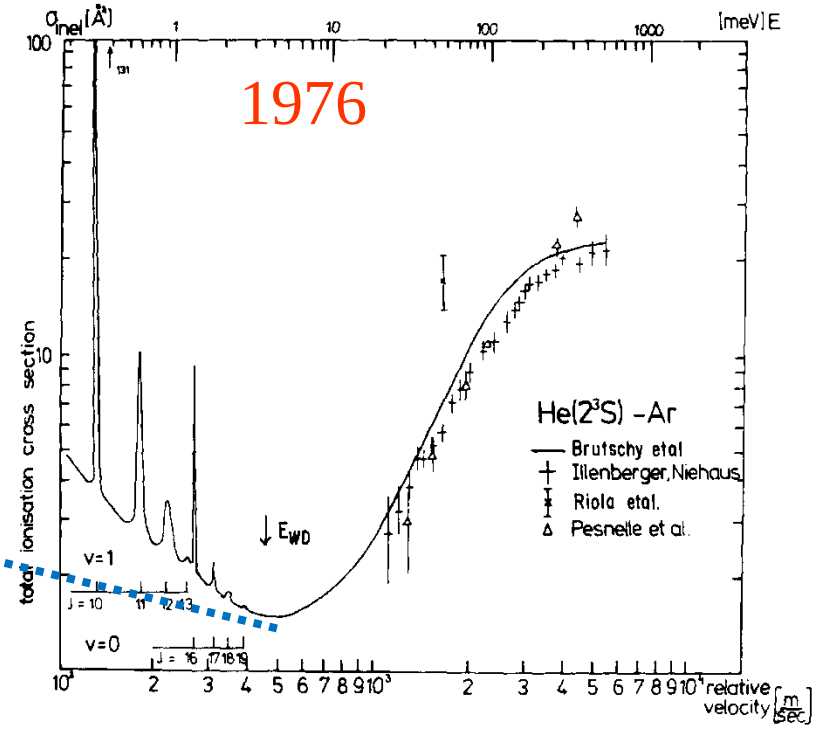

FIG. 30. Calculated total ionization cross section by Brutschy *et al.*[118] (solid curve) as a function of relative velocity for the system $He^*(2^3S)$–Ar compared with the experimental results of Illenberger and Niehaus,[160] Riola *et al.*,[374] and Pesnelle *et al.*[355] (adapted from ref. 118). The positions of the orbiting or shape resonances for (v,J) quantum numbers are also shown.

Results, …. Calculated potentials

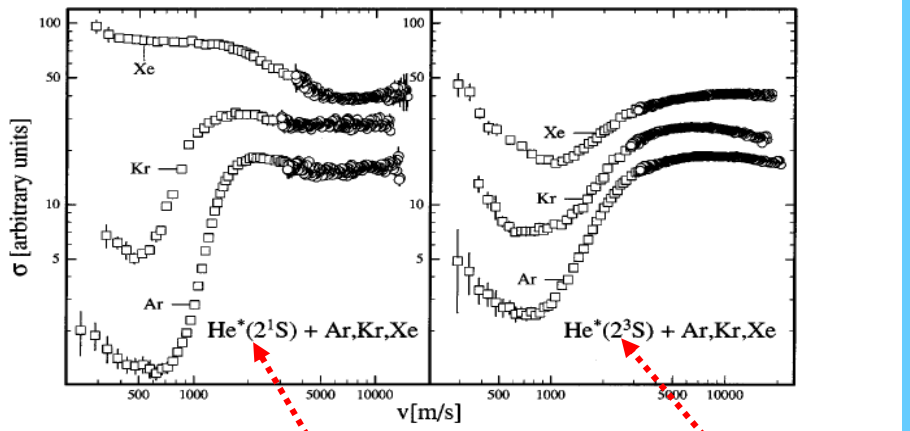

FIG. 3. Measured CI cross sections σ for He*(2 $^{1,3}S$) + Ar,Kr,Xe as a function of the He* velocity v. (□) thermal, (○) hyperthermal.

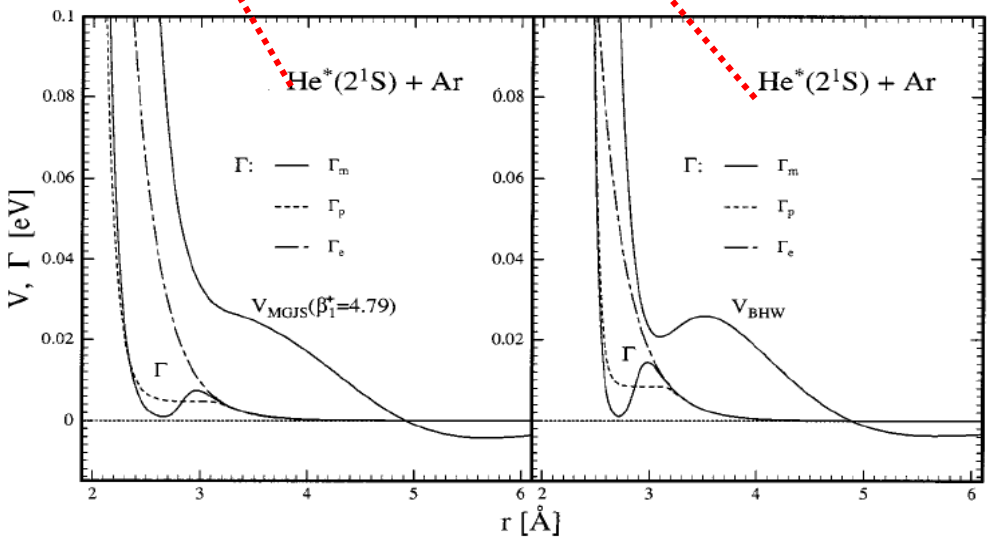

FIG. 8. Complex CI fit potentials $V(r) - i\Gamma(r)/2$ for He*(2 ^1S) + Ar using the model functions of Refs. 10 (MGJS) and 12 (BHW) for the real part $V(r)$. $\Gamma_{m,p,e}$ are explained in the text.

$He^*(2^3S)$ + Ar, Kr, Xe **cross sections …..absolute values**

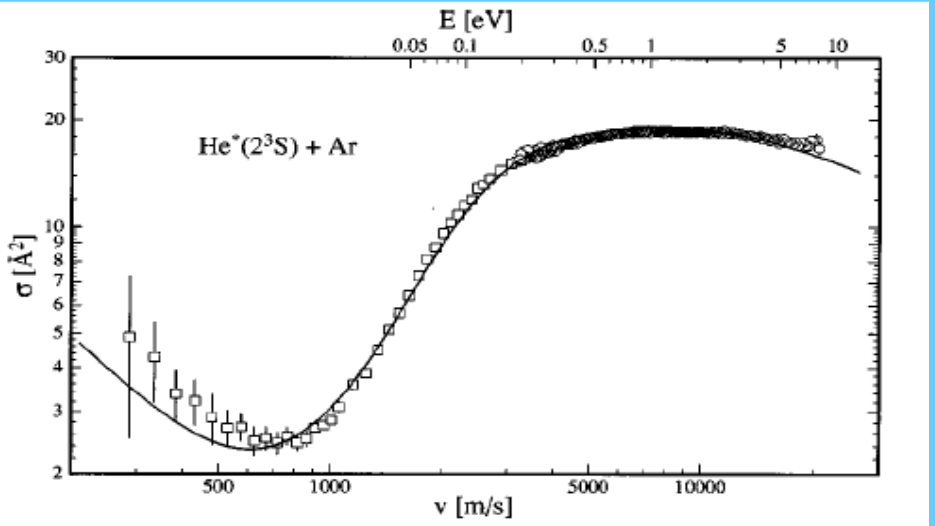

FIG. 17. $[V_{MGJS}(\beta_1^+ = 4.79) - i\Gamma_p/2]$ fit (———) of CI data for $He^*(2\,^3S) + Ar$ (□,○).

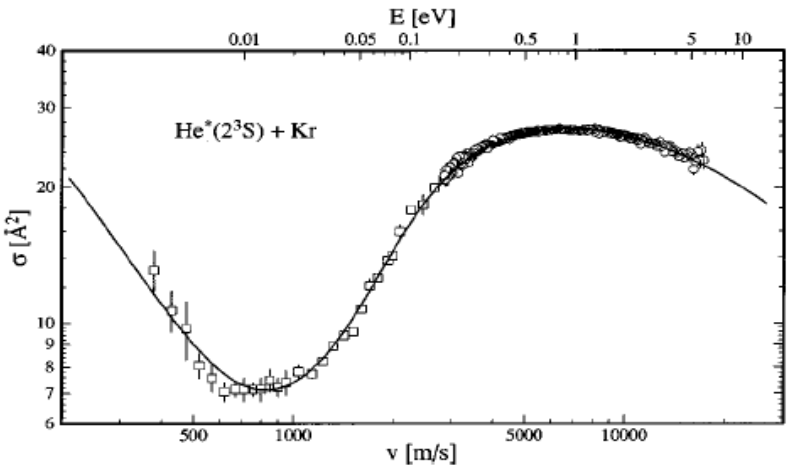

FIG. 18. $(V_{MGJS} - i\Gamma_p/2)$ fit (———) of CI data for $He^*(2\,^3S) + Kr$ (□,○).

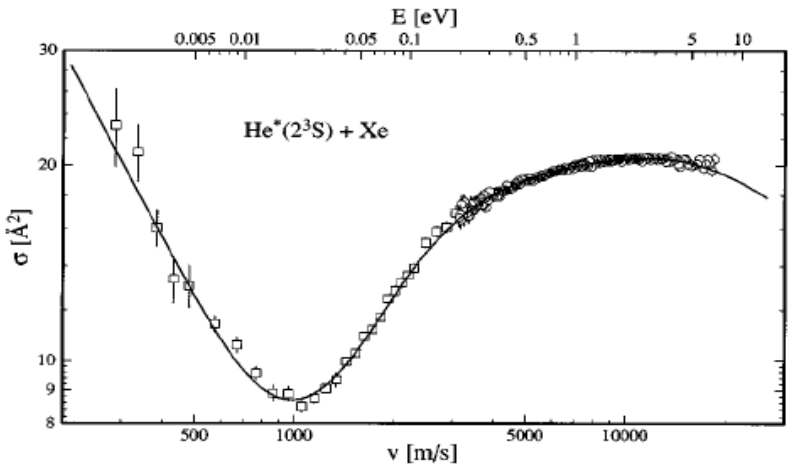

FIG. 19. $(V_{MGJS} - i\Gamma_p/2)$ fit (———) of CI data for $He^*(2\,^3S) + Xe$ (□,○).

Singled and triplet

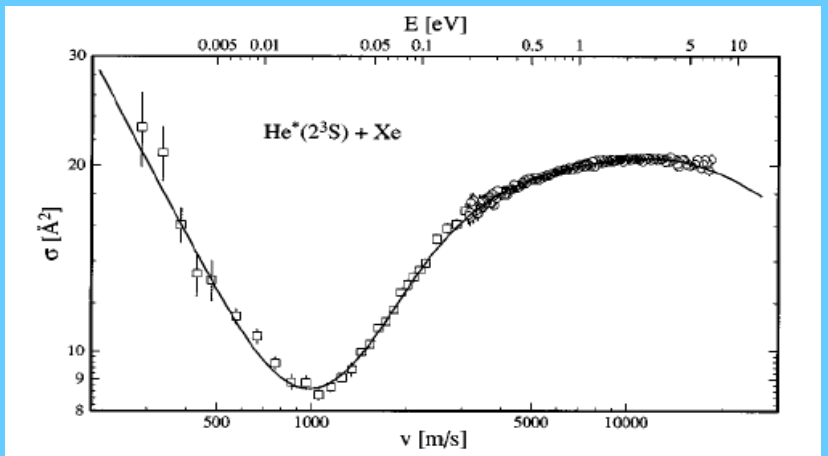

FIG. 19. ($V_{MGJS} - i\Gamma_p/2$) fit (———) of CI data for He*($2\,^3S$) + Xe (□,○).

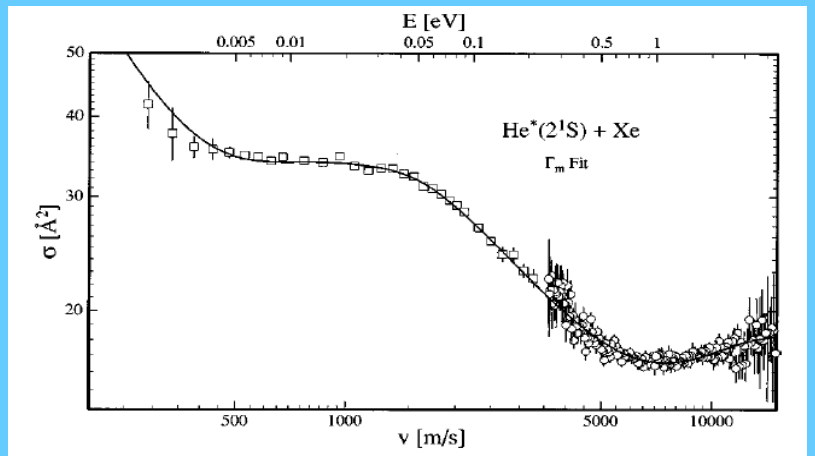

FIG. 7. ($V_{MGJS} - i\Gamma_m/2$) fit (———) of CI data for He*($2\,^1S$) + Xe (□,○).

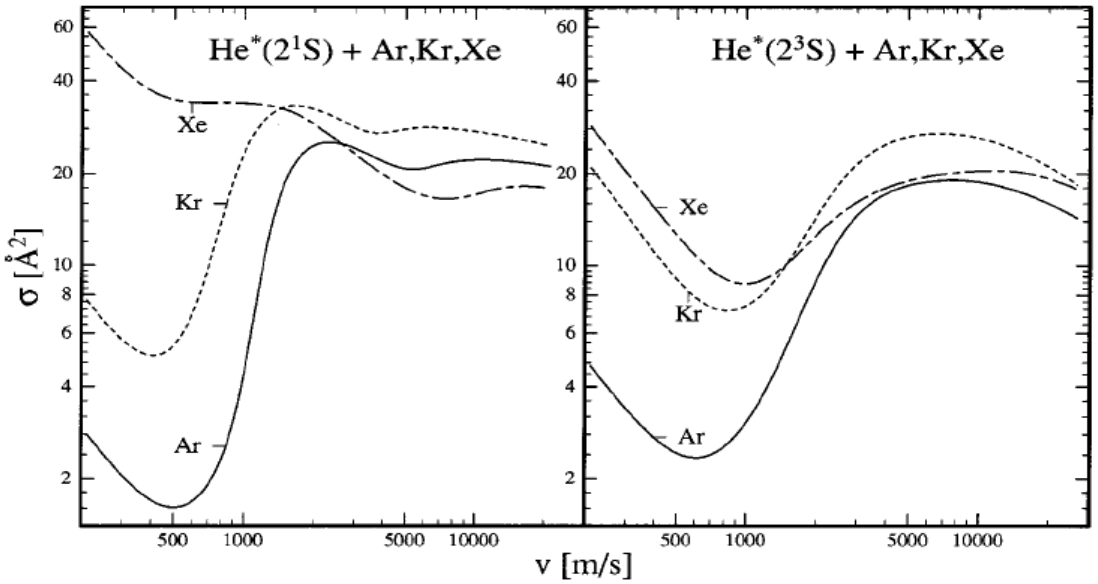

FIG. 22. Comparison of the theoretical CI cross sections σ vs v, calculated with the CI best fit potentials of He*($2\,^{1,3}S$) + Ar,Kr,Xe and averaged for the target motion in the cell.

Perugia molecular beam apparatus for Penning ionization studies

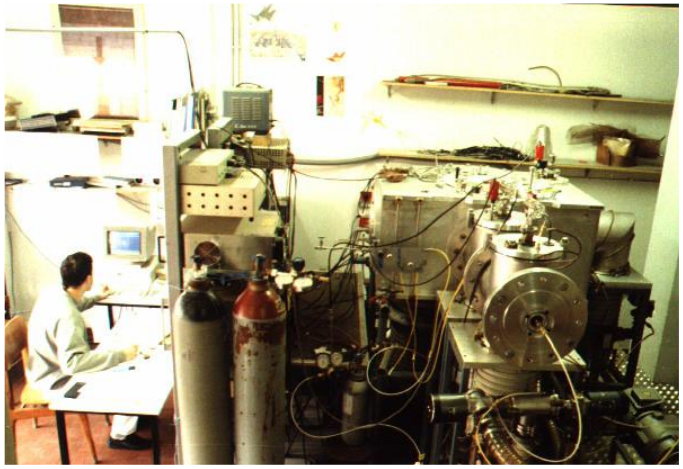

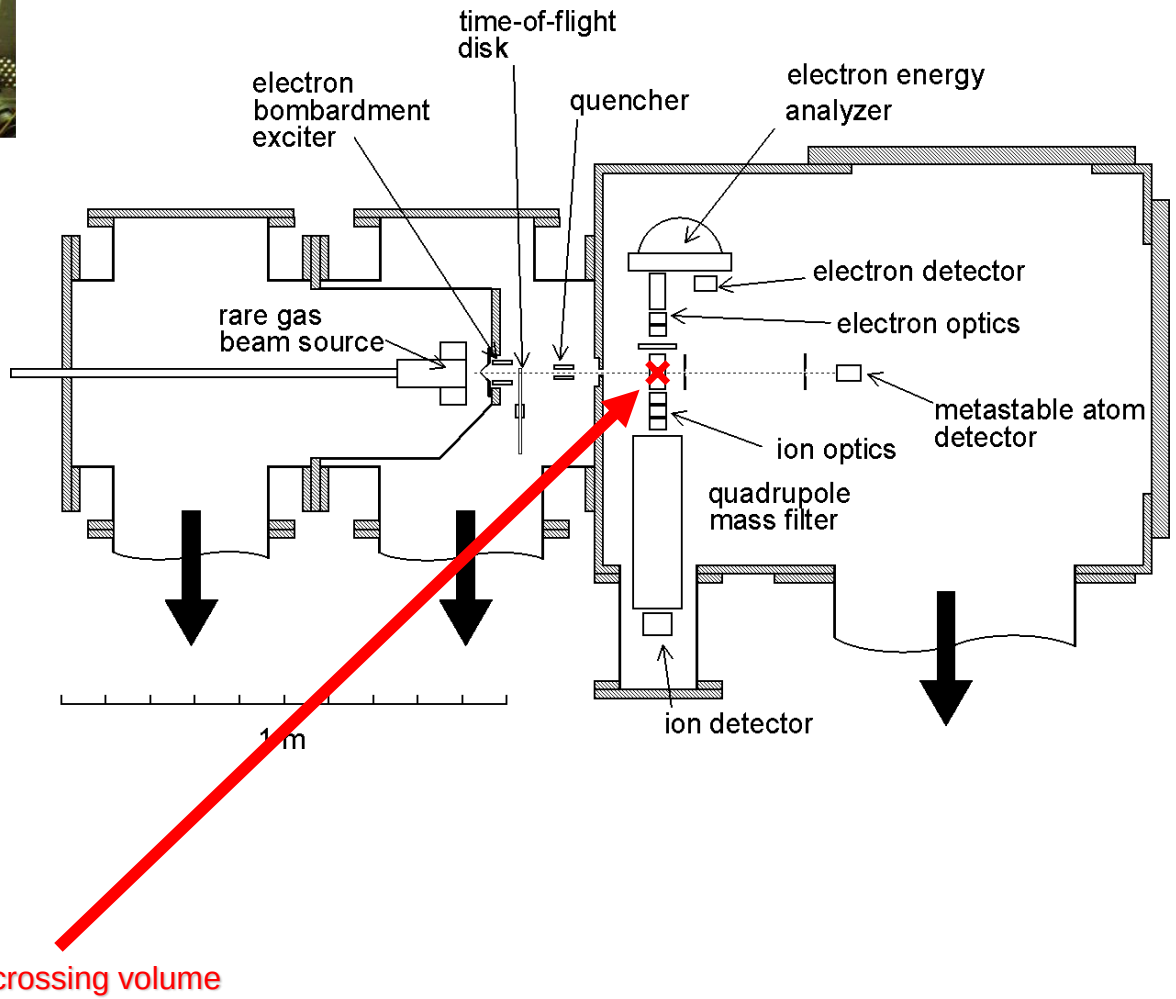

Biondini experiment

THE JOURNAL OF CHEMICAL PHYSICS **122**, 164307 (2005)

2005

Penning ionization of N_2O molecules by $He^*(2^{3,1}S)$ and $Ne^*(^3P_{2,0})$ metastable atoms: A crossed beam study

Francesco Biondini
Dipartimento di Ingegneria Civile ed Ambientale, Università di Perugia, 06125 Perugia, Italy

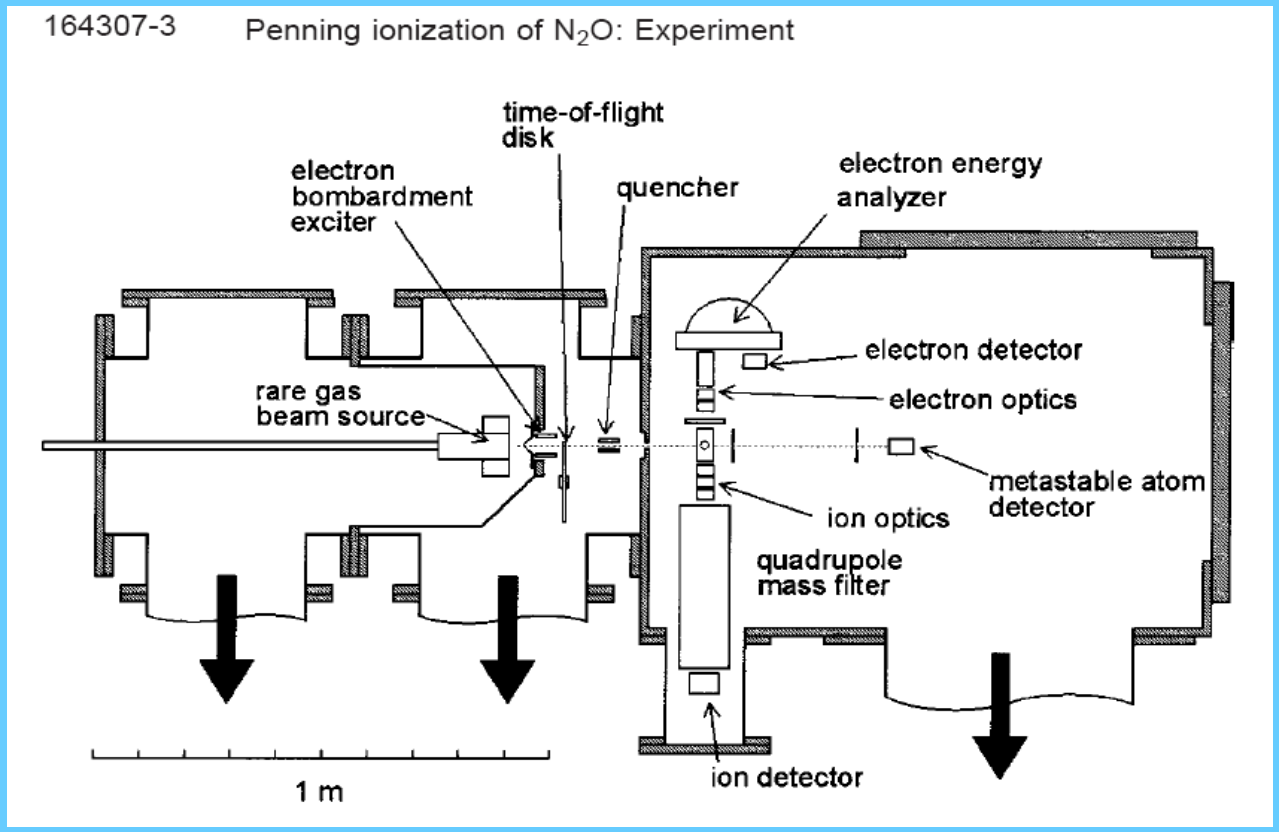

The basic configuration of the experiment consists of two crossed beams, one of metastable atoms He* or Ne* and the other of N_2O molecules. **The N_2O molecules come from a glass microcapillary array at room temperature**, while the **primary beam was produced by an effusive or supersonic source coupled with different excitation devices**, such as microwave discharge or electron impact

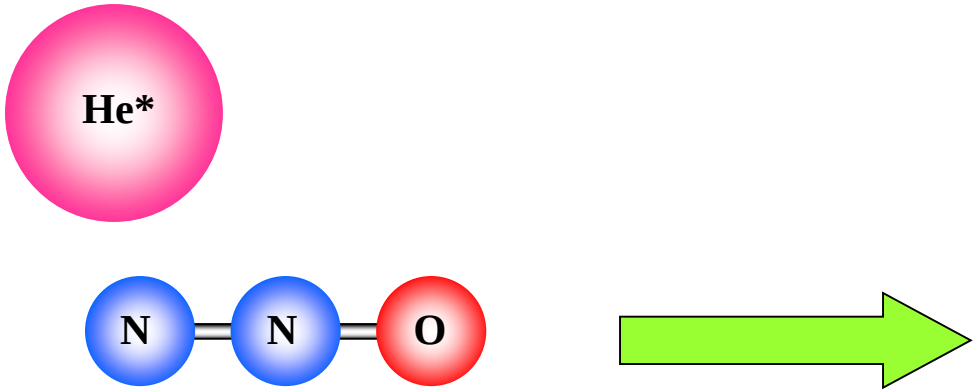

N_2O^+ ion
in the ground
$^2\Pi$ state

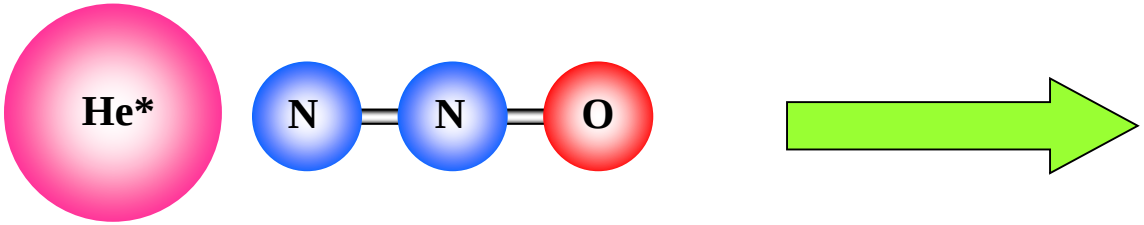

N_2O^+ ion
in the excited
$^2\Sigma$ state

$He^*(2^1S) + N_2O$

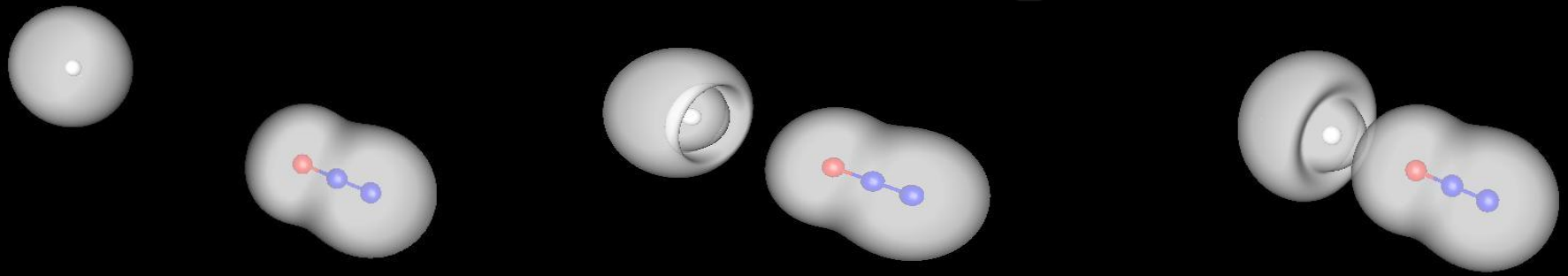

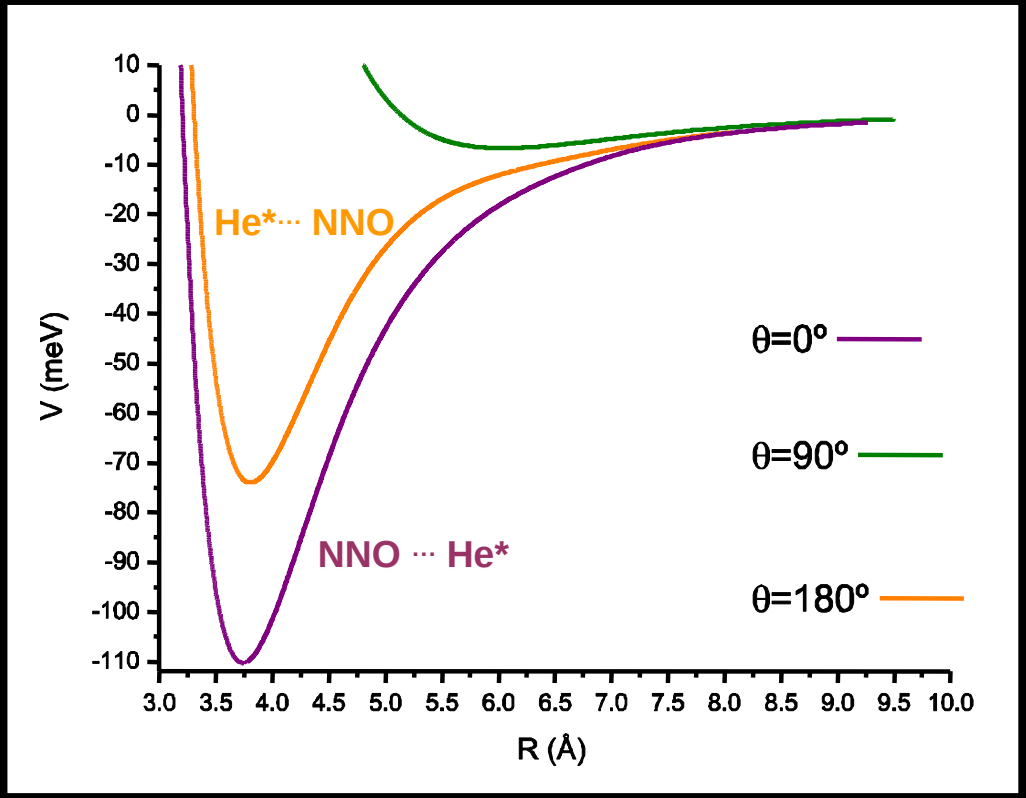
10
0
-10
-20
-30
-40
-50
-60
-70
-80
-90
-100
-110
V (meV)
3.0
3.5
4.0
4.5
5.0
5.5
6.0
6.5
7.0
7.5
8.0
8.5
9.0
9.5
10.0
R (Å)
He*··· NNO
NNO ··· He*
θ=0°
θ=90°
θ=180°

$He^*(2^3S, 2^1S)$-N_2O

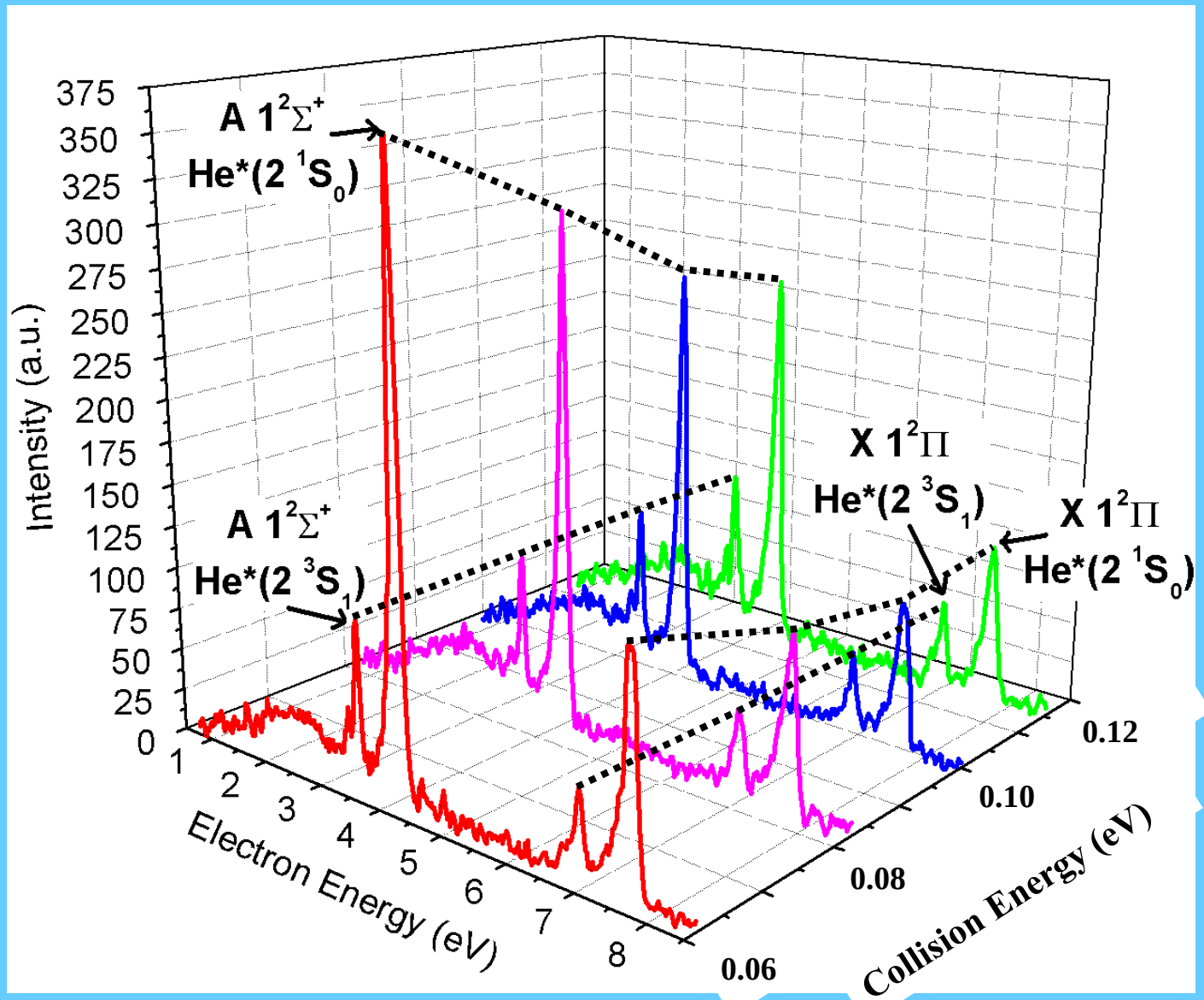

Biondini results

PIES spectra for the $He^*(^{3,1}S_{1,0})$

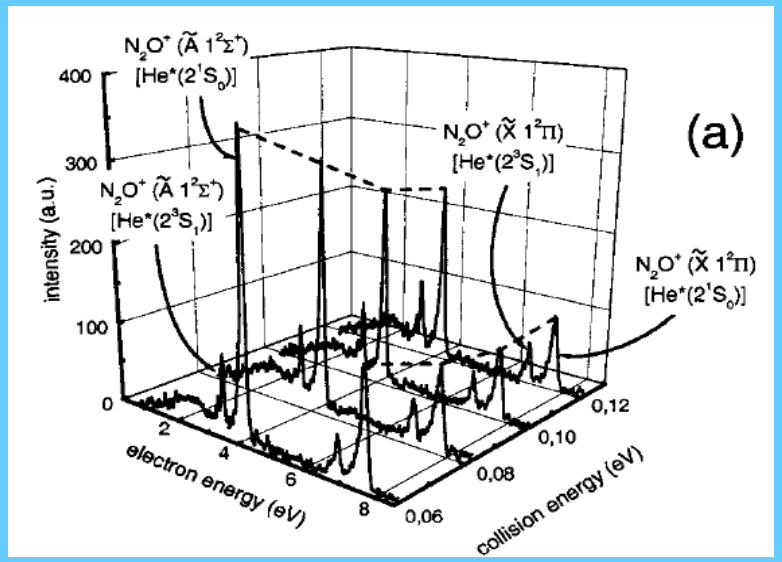

Photoionization and PIES spectra

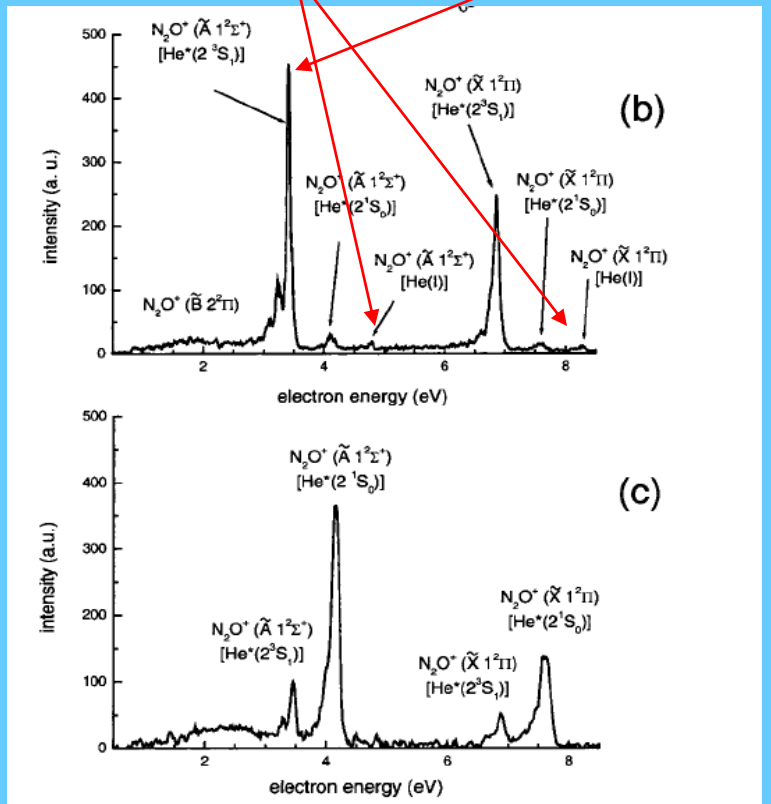

FIG. 2. (a) Spectra of electrons emitted in the ionization of N_2O by metastable helium atoms, at different collision energies, by using an electron bombardment source. (b) Spectra of emitted electrons, when also photoionization occurs, as obtained by using microwave discharge source from which both metastable atoms and photons are coming out. (c) Spectra of electrons for $He^*(^{3,1}S_{1,0})-N_2O$ ionization at 0.06 eV collision energy, as also reported in (a). At the relevant peaks, the state of product ions and the ionizing particle are indicated. The lines in all spectra join experimental points, which have been omitted for clarity. The points have been recorded every 0.01 eV.

PIES of Ne*

Mass spectra for the $Ne^*(^3P_{2,0})+N_2O$ system

Mass spectra recorded at an average collision energy of 45 meV have shown the following relative abundances:

$$Ne^*(^3P_{2,0}) + N_2O \rightarrow Ne + N_2O^+ + e^- \quad (77.9\%)$$

$$\rightarrow Ne + N + NO^+ + e^- \quad (13.3\%)$$

$$\rightarrow Ne + N_2 + O^+ + e^- \quad (8.5\%)$$

$$\rightarrow NeN_2O^+ + e^- \quad (0.3\%).$$

The electron energy spectra for $Ne^*(^3P_{2,0})+N_2O$, measured with a resolution of ~40 meV (FWHM) and reported in Fig. 3, show the peaks for $N_2O^+(\tilde{X}\,^2\Pi)$ production in the $v=0,1,2$ vibrational states. The $\tilde{A}\,^2\Sigma^+$ excited electronic state of N_2O^+ ion, although energetically accessible, has not been observed in our apparatus because the related electrons have a kinetic energy content below 1.0 eV. Finally, in the Ne^*-N_2O system, the $\tilde{B}\,^2\Pi$ excited electronic state of N_2O^+ is energetically inaccessible. In Fig. 3, the $N_2O^+(\tilde{X}\,^2\Pi)$ peaks show the different contributions for the fine structure components, $^3P_2$ and $^3P_0$. The data, recorded at different collision energies, show an increase of the ionic production by

Electron spectra s recorded at different collision energies

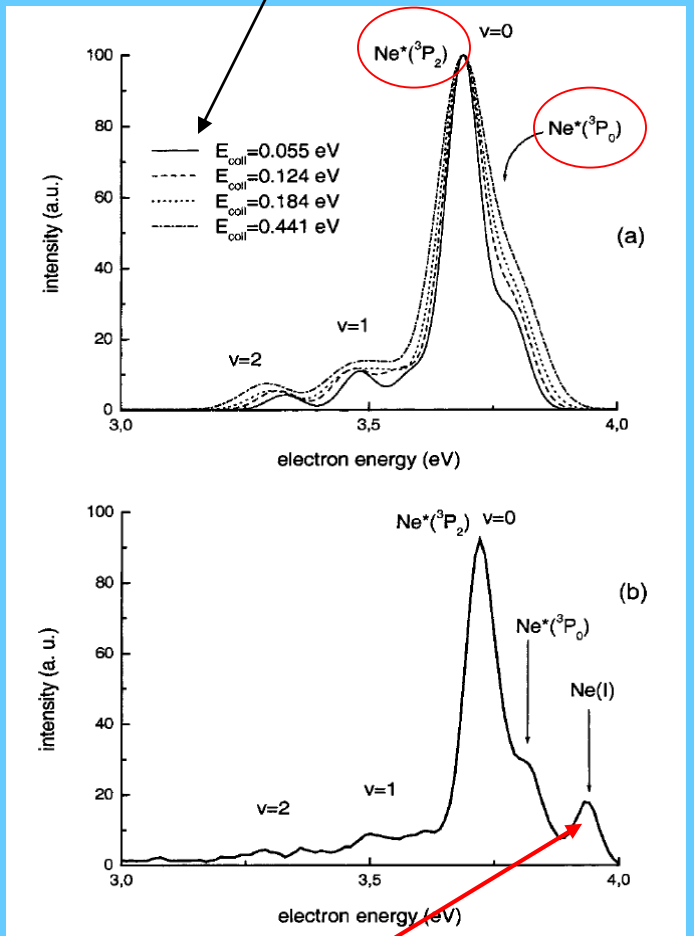

FIG. 3. Electron energy spectra of $Ne^*(^3P_{2,0})-N_2O$ ionization. In this case, only $N_2O^+(\tilde{X}\ 1\ ^2\Pi)$ can be formed. (a) Spectra at different collision energies obtained by using an electron bombardment source. (b) Spectra, when also photoionization occurs, as obtained by using microwave discharge source from which both metastable atoms and photons are coming out. The lines in all spectra joins experimental point, which have been omitted for clarity. The points have been recorded every 0.01 eV.

Rg = He, Ne

$Rg^* + N_2O \rightarrow [Rg\ldots N_2O^+] + e^-$

$[Rg\ldots N_2O^+] \rightarrow N_2O^+$

$\rightarrow NO^+ + N$

$\rightarrow O^+ + N_2$

$\rightarrow RgN_2O^+$

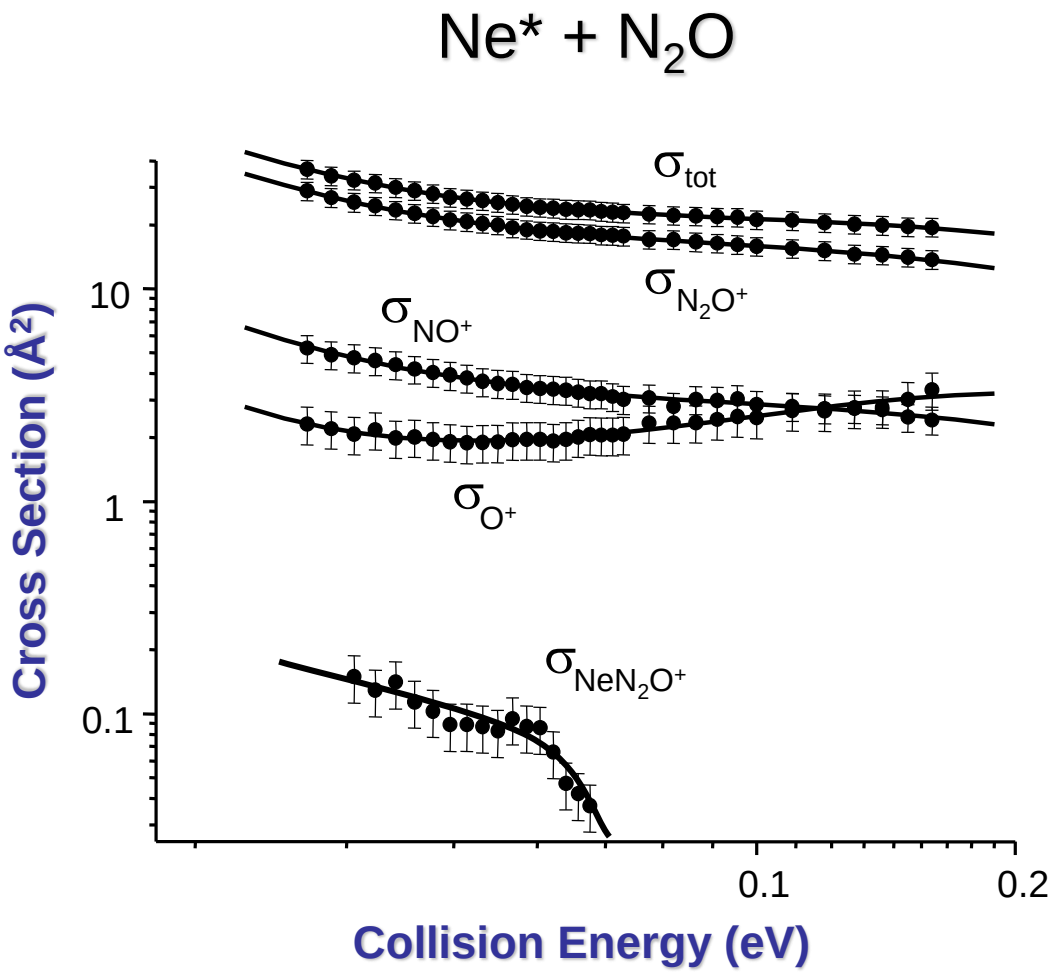

PIES of Ne*

Mass spectra for the $Ne^*(^3P_{2,0})+N_2O$ system

Mass spectra recorded at an average collision energy of 45 meV have shown the following relative abundances:

$$Ne^*(^3P_{2,0}) + N_2O \rightarrow Ne + N_2O^+ + e^- \quad (77.9\%)$$

$$\rightarrow Ne + N + NO^+ + e^- \quad (13.3\%)$$

$$\rightarrow Ne + N_2 + O^+ + e^- \quad (8.5\%)$$

$$\rightarrow NeN_2O^+ + e^- \quad (0.3\%)$$

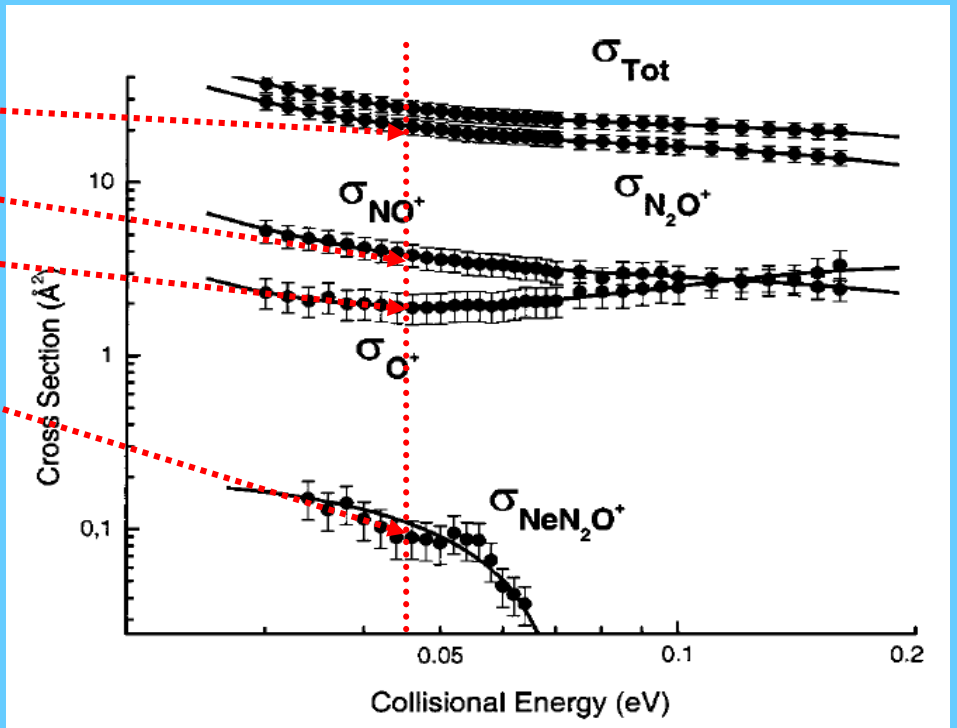

FIG. 4. Absolute total and partial ionization cross sections, as a function of collision energy, for $Ne^*(^3P_{2,0})-N_2O$ leading to the formation of N_2O^+, NO^+, O^+, and NeN_2O^+. Curves connecting experimental points are visual aids to show the energy dependence for the cross sections.

PIES of He * and Ne*

Mass spectra recorded at an average collision energy of 45 meV have shown the following relative abundances:

$$Ne^*(^3P_{2,0}) + N_2O \rightarrow Ne + N_2O^+ + e^- \quad (77.9\%)$$

$$\rightarrow Ne + N + NO^+ + e^- \quad (13.3\%)$$

$$\rightarrow Ne + N_2 + O^+ + e^- \quad (8.5\%)$$

$$\rightarrow NeN_2O^+ + e^- \quad (0.3\%).$$

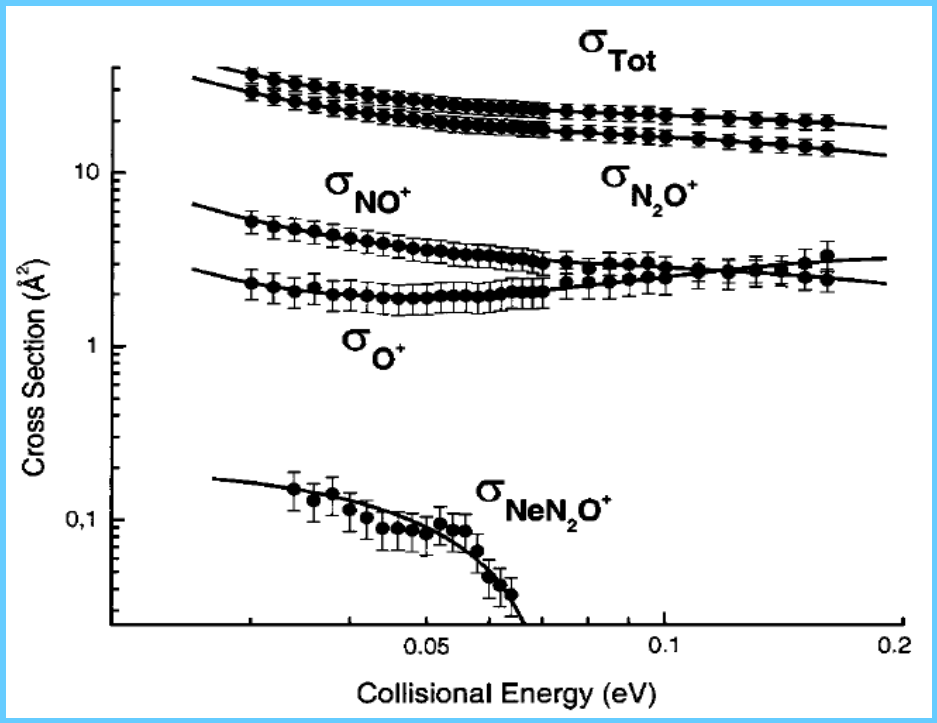

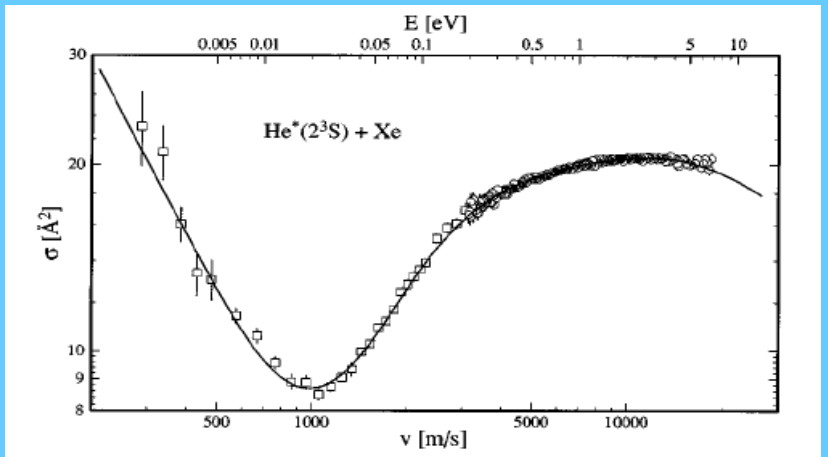

FIG. 19. ($V_{MGJS} - i\Gamma_p/2$) fit (———) of CI data for He*($2\,^3S$) + Xe (□,○).

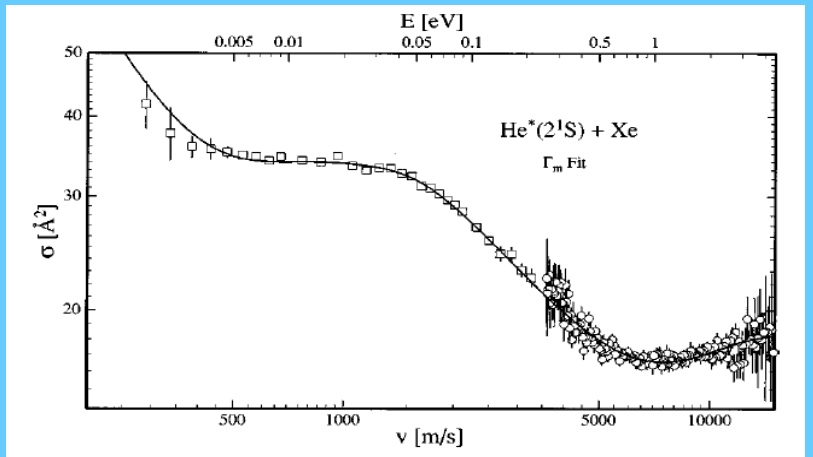

FIG. 7. ($V_{MGJS} - i\Gamma_m/2$) fit (———) of CI data for He*($2\,^1S$) + Xe (□,○).

Velocity dependence of total ionization cross section $H^*(2^3S)$- Ar

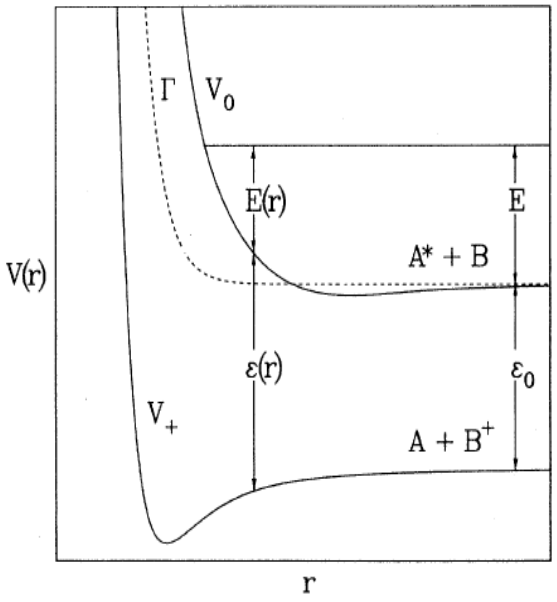

FIG. 2. Two-potential-curve model for Penning ionization. E is the center-of-mass kinetic energy of collision; ε_0 is the separation of the reagent and product potential asymptotes, $\varepsilon_0 = E_*(A^*) - IE(B)$; $E(r)$ is the (classical) local heavy-particle kinetic energy, including centrifugal energy; and $\varepsilon(r)$ is the kinetic energy of the Penning electron when Penning ionization takes place at separation r.

Branching ratio

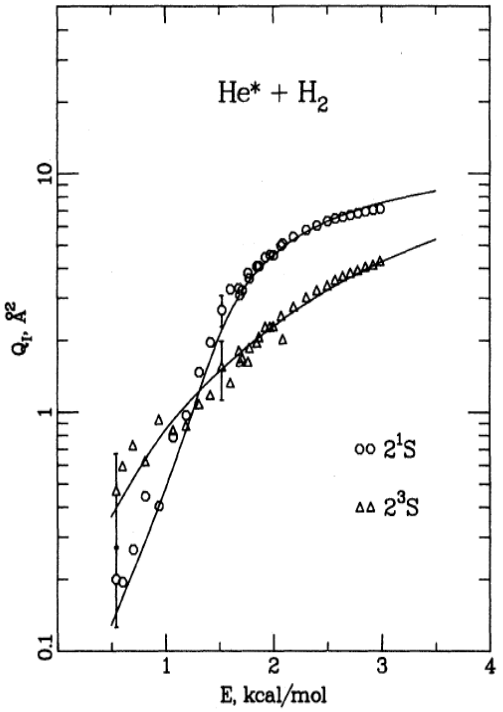

FIG. 12. Total ionization cross sections for $He^* + H_2$, experimental data (points) from Martin *et al.* (1984, 1989), and calculated curves from Martin and Siska (1985, 1988). The experimental measurements are relative, the absolute units being derived from the theoretical curves, which, when integrated over a Maxwellian energy distribution, match the measured total quenching rates at 300 K (Schmeltekopf and Fehsenfeld, 1970).

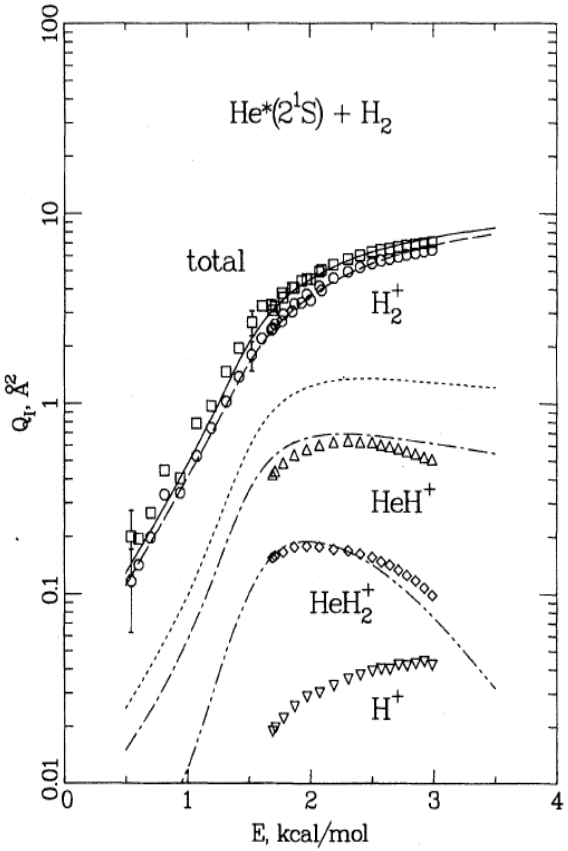

FIG. 13. Energy dependence of product branching for $He^*(2\,^1S) + H_2$ PI, experimental data from Martin *et al.* (1984, 1989), and calculated branching patterns from the modified phase-space model of Martin *et al.* (1989). The short-dashed curve represents the maximum cross section for HeH^+ allowed by the Langevin capture criterion, while the other curves correspond with the experimental data they lie closest to.